

Process Optimization of Ultrasonic Tacking of Unidirectional Tapes

Implementation of Fundamental Ultrasonic Welding Knowledge in the Automated Tape Laying Process for Unidirectional Carbon Fibre Thermoplastic PEEK and PEKK Tapes

N. Katuin

MSc. Thesis

Faculty of Aerospace Engineering
Delft University of Technology



Process Optimization of Ultrasonic Tacking of Unidirectional Tapes

Implementation of Fundamental Ultrasonic Welding Knowledge in the Automated Tape Laying Process for Unidirectional Carbon Fibre Thermoplastic PEEK and PEKK Tapes

by

N. Katuin

to obtain the degree of Master of Science

at the Delft University of Technology

to be defended publicly on Wednesday September 23, 2020 at 03:00 PM.

Student number:	4738373	
Project duration:	September 9, 2019	- September 13, 2020
Thesis committee:	Prof. dr. ir. Clemens A. Dransfeld	- TU Delft, chair, supervisor
	Asst. Prof. dr. ir. Miguel A. Bessa	- TU Delft, examiner
	Asst. Prof. dr. ir. Daniël M. J. Peeters	- TU Delft, examiner
	Ing. Jan G. Groothedde	- Boikon B.V., daily supervisor
	Ir. Meindert J. ter Veer	- Boikon B.V., daily supervisor

Document type: Public

An electronic version of this thesis is available at <http://repository.tudelft.nl/>.

*Scientist discover the world that exists,
engineers create the world that never was.*

T. von Karman

Preface

After receiving my bachelor's degree in Aeronautical Engineering at the Inholland University of Applied Sciences Delft I decided to continue my educational career at the Delft University of Technology. With this thesis, related to continuous ultrasonic tacking of thermoplastic unidirectional carbon fibre tapes, I am concluding my university period by receiving a master's degree in Aerospace Engineering.

First of all, I would like to express my gratitude to all the employees of Boikon B.V., Leek. Doing research for Boikon B.V. felt like a sincere collaboration between myself and the company, this because of the support and interest from various departments within the company. In special I would like to thank my daily supervisors, Jan and Meindert. Even in times of COVID-19, Jan made it possible to perfectly guide this project by having essential meetings on regular basis and keeping the goal of this project crystal clear by constantly considering the expectations of Boikon and the university. Discussions with Meindert on regular basis, in combination with his technical ultrasonic tacking expertise enormously contributed to the achieved results presented in this thesis.

Secondly, I would like to thank Clemens for the superior guidance and continuous support throughout the project. I am very pleased that you accepted my request for supervision. Clemens his broad expertise in the field of (thermoplastic) composites, in combination with his interest to the topic resulted in fruitful biweekly meetings which always encouraged me to continue working on the project. Furthermore, I would like to thank Miguel Bessa and Daniël Peeters for being part of my thesis committee.

Last but not least, I would like to thank my friends in Delft and Groningen, family and housemates for their continuous encouragement and support. Thanks for everything!

*N. Katuin
Leek (NL), September 2020*

Summary

Variations in the ability to tack various Unidirectional (UD) tapes consisting of Polyetheretherketone (PEEK) and Polyetherketoneketone (PEKK) Thermoplastic (TP) polymers reinforced with Carbon Fibre (CF) are observed at Boikon B.V. while utilising their developed Ultrasonic Tacking (UST) technique. Therefore, a research project with main objective; "Improving the understanding of the UST process to increase the tape laying speed and preserving the tacking quality of PEKK and PEEK UD tapes by providing Boikon with fundamental knowledge related to the most influential parameters, obtained from extensive literature research and validated with experimental work" was initiated.

The converter, booster and sonotrode are the three main components of the ultrasonic stack required to introduce the ultrasonic vibrations in the UD tape. The vibrational amplitude generated by the converter is amplified by the booster and the sonotrode while pressure is exerted by the ultrasonic stack to ensure efficient energy transmission. A bond between two UD tapes is established when fusion of polymer chains across the interface takes place. In order for polymer fusion to take place the TP polymer must be sufficiently heated. The ease of heating of TP polymers during UST depends on two heating mechanism and various polymer material properties. The E' and E'' of semi-crystalline polymers used for high structural applications are unfavoured for UST, and partially explain why processing of PEEK and PEKK is challenging. The vibrational amplitude, continuous tacking pressure and the tape laying velocity are considered the most important influential parameters for the process. The amplitude at the sonotrode tip is in direct relation with the amount of dissipated energy, a higher amplitude results in the generation of additional heat. Besides the magnitude of energy dissipation per time unit, the amount of generated heat also depends on the duration of the process, in other words the tape laying velocity.

Based on the existing method of Voronoi Tessellation, an algorithm was developed to characterize the microstructure of an UD tape using multiple micrographs. The fibre locations are extracted from the micrographs using image analysis software. This in combination with the defined tape boundary characterizes the distribution of fibres and resin through the tape thickness. A local Fibre-Resin Ratio (FRR) ratio was introduced to quantify, and compare various tapes. Each of the through thickness distributions of the three different tapes analysed show unique behaviour. This type of distribution emphasizes that much variation is present between various micrographs analysed of the same UD tape, especially in the vicinity of the outer surfaces. For UST the outer surfaces are of high importance because the TP resin here should establish the bond between both UD tapes. Therefore, a different type of analysis was developed. This analysis is called the localized analysis and provides the average FRR of regions only in contact with the tape boundary. The localized analysis more accurately quantifies and distinguishes the outer surfaces of the three tapes analysed, especially for tapes showing much surface waviness.

Based on micrographs obtained from tacked samples prepared using the Falko Automated Tape Laying (ATL) an analysis is performed to relate the microstructure to the consistency of tacking. Remarkably, the variation of FRR at the outer surfaces is also present in the measured Bond Line Length (BLL) of tacked samples. The bond lengths measured at various locations over multiple micrographs per UD tape emphasize that the degree of consistency in FRR distribution is in relation to the consistency of established bonds.

The influence of the amplitude, pressure and velocity on the bond strength is extensively studied using Response Surface Methodology (RSM) as type of Design of Experiment(s) (DOE). Different combinations of parameter settings are utilised to prepare the samples. The bond strength is measured using a Mandrel Peel (MP) setup designed, built and validated at Boikon. The RSM provides an Analysis of Variance (ANOVA), and based on that it is possible to determine which of the significant second order model terms contributes most to the bond strength. By critically reviewing these results, in combination with the response surfaces, it became clear that the vibrational amplitude showed the highest potential for process optimization in terms of an increased tape laying velocity.

The variation in measured bond strength, using the developed MP setup, was analysed based on the peel force curves of various samples. A trend was observed showing that the degree of variation in BLL and FRR is in agreement with the variation in the measured bond strength of tacked samples.

Validation of the results from the parameter study was performed by implementing a high gain booster in the Falko ATL. This resulted in an increase of vibrational amplitude. Various samples were prepared using a step-wise increase of amplitude, while keeping the other parameters similar. With the use of the MP setup it was shown that the bond strength increased with an increase of amplitude. For process optimization it was of interest what the effect of an velocity increase is on the measured bond strength. While increasing the velocity, the bond strength dropped slightly but an increase of vibrational amplitude showed its potential for process optimization.

Based on the results of the microstructure characterization experiment it is concluded that each UD tape can be described with an unique FRR distribution. The fibre rich outer surfaces with much variation of the PEEK tape from Teijin, in combination with the unfavourable semi-crystalline TP polymer properties explain why processing of this specific UD tape is challenging. Less challenging to process is the PEKK tape from Solvay. This tape does posses a resin rich upper surfaces what enhances the bonding capabilities. Nevertheless, the BLL experiment concludes, in terms of bond length consistency, that a rather consistent distribution of fibres and resin is favoured compared to a resin rich UD tape with severe surface waviness. Furthermore it was found that variations in BLL, FRR and peel force are interrelated. Each of the parameters included in the statistical model showed significance with respect to the bond strength, meaning that each of these parameters influences the final bond strength. The amplitude showed the highest potential for process optimization. With tuning of the continuous tacking pressure identical bond strengths can be obtained with the implemented high gain booster, while utilising a velocity increase of 43%.

The current method used to characterize microstructures of UD tapes was successfully used, but requires optimization for a more precise analysis. Additionally, the optimum value of vibrational amplitude for process optimization should be determined such that a maximum increase of tape laying velocity can be realized while preserving the bond strength.

Contents

Preface	iii
Summary	v
Table of Contents	viii
List of Figures	ix
List of Tables	xiii
List of Acronyms	xv
List of Symbols	xvii
1 Introduction	1
1.1 Project Background	1
1.2 Research Questions and Methodology	2
1.3 Thesis Outline	3
2 Literature Review	5
2.1 An introduction to ultrasonic welding technology	5
2.1.1 Description of ultrasonic welding components	6
2.1.2 Thermoplastic Material Properties for Ultrasonic Welding	9
2.2 The Physics of Ultrasonic Welding	12
2.2.1 Wave propagation and attenuation	12
2.2.2 Heating Mechanisms	15
2.2.3 Heat Transfer	16
2.2.4 Squeeze flow and wetting	16
2.2.5 Bonding Mechanisms	16
2.2.6 Parameter Influences to Ultrasonic Welding	17
2.3 The Quantification of Welding Quality	20
2.3.1 T-peel Test	20
2.3.2 Fixed-arm Peel Test	20
2.3.3 Floating Roller Peel Test	21
2.3.4 Mandrel Peel Test	22
2.4 Statistical Methods for Design of Experiments	23
2.4.1 Design of Experiment Motivation	23
2.4.2 Response Surface Methodology	24
3 Microstructural Characterization of Unidirectional Tapes	31
3.1 Methodology of Experiment	31
3.2 Sample Preparation and Micrograph Analysis	32
3.3 Design of Analytical Material Analysis Model	33
3.3.1 Fibre Coordinates Extraction	33
3.3.2 Fibre Coordinate Data Post-Processing	36
3.4 Results and Discussion	41
3.5 Concluding Remarks	44
4 Quality Quantification of Tacked Unidirectional Tapes	45
4.1 Methodology of Experiment	45
4.2 Motivation of Mandrel Peel Test	45
4.3 Design of Experimental MP Setup	47
4.4 Construction of Experimental MP Setup	48
4.5 Validation of Experimental MP Setup	49

4.6	Concluding Remarks	52
5	Experiments and Analysis of Tacked Unidirectional Samples	53
5.1	Bond Line Comparison of Tacked UD Tape Samples.	53
5.1.1	Methodology of Experiment	53
5.1.2	Preparation and Microscopy of Samples	53
5.1.3	Bond Length Measurements	54
5.1.4	Results and Discussion	54
5.1.5	Concluding Remarks	56
5.2	Influential Tacking Parameter Study	56
5.2.1	Methodology of Experiment	56
5.2.2	Parameter space of Influential Parameters	56
5.2.3	Validation of Statistical Model Assumptions	57
5.2.4	The Application of Data Transformation	58
5.2.5	Results and Discussion	59
5.2.6	Concluding Remarks	61
5.3	Effect of UD Tape Microstructure on Bond Strength Variation	62
5.3.1	Methodology of Experiment	62
5.3.2	Results and Discussion	63
5.3.3	Concluding Remarks	64
6	Optimization of Ultrasonic Tacking Technology	65
6.1	Influence of Increased Vibrational Amplitude on Bond Strength	65
6.1.1	Methodology of Experiment	65
6.1.2	Modification of Ultrasonic Tacking Stack	65
6.1.3	Results and Discussion	67
6.1.4	Concluding Remarks	68
6.2	Validation of Booster Implementation	68
6.2.1	Methodology of Experiment	68
6.2.2	Results and Discussion	68
6.2.3	Concluding Remarks	69
7	Conclusions and Recommendations	71
7.1	Conclusions.	71
7.2	Recommendations	73
	Bibliography	75
A	Microstructure Characterization Python Script	85
B	Bond Line Length Comparison Micrographs	99
C	DOE Peel Force Results	103
D	Analysis of Variance DOE Results	105
E	Optimization of Ultrasonic Technology Experiment Results	107

List of Figures

1.1	Photograph of the Falko ATL	1
1.2	Photograph of the slitting equipment	1
1.3	Process flow from UD tape production to consolidated final part	2
2.1	Classification of thermoplastic polymer joining techniques	5
2.2	Schematic visualisation of main USW components	6
2.3	Development of vibrational amplitude and stress in the USW components.	7
2.4	Influence of sonotrode shape to vibrational amplitude and stress	8
2.5	Visualisation of storage and loss modulus	9
2.6	Amorphous and semi-crystalline polymer dynamic mechanical properties	10
2.7	Three different cyclic loading viscoelasticity models	11
2.8	Molecular structure repeat units of PEEK, PEKK and PP	12
2.9	Captured sound and energy conversion fringe patterns in a rod	13
2.10	Influence of shear modulus and $\tan \delta$ on temperature change	14
2.11	Bonding steps for inter-diffusion of polymer chains across welding interface	17
2.12	Polymer chain alignment across welding interface	18
2.13	Influence of welding force to weld strength for various polymers	18
2.14	Behaviour of energy director throughout the welding process	19
2.15	Schematic illustration of the T-peel test	21
2.16	Schematic illustration of the fixed-arm peel test	21
2.17	Various possible T-peel test situations	21
2.18	Schematic illustration of the floating roller peel test	22
2.19	Schematic illustration of the mandrel peel test	22
2.20	Influence of alignment force for conformity of the mandrel peel test	23
2.21	Three predictor, three level Circumscribed and Face centred central composite designs	25
2.22	Transformation of predictor levels from engineering units to coded units	25
2.23	Non-normality response distribution plot	26
2.24	Example plot of residuals versus observation order	26
2.25	Residual versus fitted value plot - homoscedasticity	27
2.26	Residual versus fitted value plot - heteroscedasticity	27
2.27	F-value distribution plot including critical F-value	29
2.28	Example response surface plot	30
2.29	Example contour plot	30
3.1	Voronoi pattern visualized using four subsequent steps	32
3.2	Photograph of UD samples in sample holder before embedding	33
3.3	Photograph of embedded and prepared UD tape samples for microscopy	33
3.4	Overview of micrographs of the PEEK and PEKK tapes	34
3.5	Micrographs presenting material defects of the PEEK and PEKK tapes	35
3.6	UD tape fibre coordinate extraction using ImageJ	35
3.7	Material analysis with Voronoi pattern functional blocks	36
3.8	Visualization of transformation from infinite to finite Voronoi vertices of a basic diagram	37
3.9	CF-PEEK Solvay tape boundary definition by constructing a polygon in ImageJ	38
3.10	Voronoi diagram with FRR colour plot of Teijin CF-PEEK tape section	40
3.11	Corresponding through tape thickness FRR distribution of Teijin CF-PEEK tape section	40
3.12	Upper and lower boundary Voronoi cell detection of Solvay CF-PEKK tape	40
3.13	Voronoi diagram sections CF-PEEK Teijin UD tape	41
3.14	Voronoi diagram sections CF-PEKK Solvay UD tape	41
3.15	Voronoi diagram sections CF-PEKK Toray UD tape	41

3.16 Mean FRR through thickness CF-PEEK - Teijin tape	42
3.17 Mean FRR through thickness CF-PEKK - Solvay tape	42
3.18 Mean FRR through thickness CF-PEKK - Toray tape	42
3.19 Mean FRR bar plot of Voronoi cells intersecting with UD tape top and bottom surfaces	43
4.1 3D HiCAD design of the mandrel peel test setup	47
4.2 3D HiCAD design linear vertical displacement unit	48
4.3 Mandrel peel test experimental setup	49
4.4 Close up photo of interaction between force gauge and mandrel peel test setup	49
4.5 Photograph of UD tape fixture	49
4.6 Photograph of pulley system for alignment weights	49
4.7 Initial friction tests for mandrel peel test setup validation using CF-PEEK samples	50
4.8 Peel rate comparison for mandrel peel test setup validation - low peel rate	51
4.9 Peel rate comparison for mandrel peel test setup validation - intermediate peel rate	51
4.10 Peel rate comparison for mandrel peel test setup validation - high peel rate	51
4.11 Photograph showing the presence of fibre bridging at the front during the MP test	52
4.12 Photo showing the presence of fibre pull-out at the back during the MP test	52
4.13 Peel force behaviour: peel rate versus coefficient A	52
4.14 Peel force behaviour: peel rate versus coefficient B	52
5.1 Schematic visualization of preparation of UD test strokes	54
5.2 Example of bond length determination method	54
5.3 Bar chart representing bond line comparison of tacked CF-PEEK and CF-PEKK tapes	55
5.4 Bar chart representing bond line comparison of tacked Solvay CF-PEKK tapes	55
5.5 Schematic illustration DOE parameter space	57
5.6 CF-PEEK Teijin DOE validation of the statistical analysis assumptions	58
5.7 CF-PEKK Solvay DOE validation of the statistical analysis assumptions	58
5.8 CF-PEKK Toray DOE validation of the statistical analysis assumptions	58
5.9 Validation of the statistical analysis assumptions of transformed CF-PEKK Toray DOE data	59
5.10 CF-PEEK Teijin response surfaces showing relations between predictors and response	60
5.11 CF-PEKK Solvay response surfaces showing relations between predictors and response	61
5.12 CF-PEKK Toray response surfaces showing relations between predictors and response	61
5.13 Peel force graphs of PEEK and PEKK low tacking parameter settings samples	63
5.14 Peel force graphs of PEEK and PEKK high tacking parameter settings samples	63
5.15 Visualization of relations between FRR, R_{BLL} and R_{PF}	64
6.1 Ultrasonic stack configurations used for booster implementation	66
6.2 Bond strength differences of samples from different ultrasonic stack configurations	66
6.3 Required power differences of samples from different ultrasonic stack configurations	66
6.4 Overview of fitted line plot of vibrational amplitude versus bond strength	67
7.1 Schematic ideal UD tape FRR distribution for UST	72
B.1 Bond line comparison micrographs of tacked CF-PEEK Teijin sample 1	99
B.2 Bond line comparison micrographs of tacked CF-PEEK Teijin sample 2	99
B.3 Bond line comparison micrographs of tacked CF-PEEK Teijin sample 3	99
B.4 Bond line comparison micrographs of tacked CF-PEKK Solvay tape 1	100
B.5 Bond line comparison micrographs of tacked CF-PEKK Solvay sample 2	100
B.6 Bond line comparison micrographs of tacked CF-PEKK Solvay sample 3	100
B.7 Bond line comparison micrographs of tacked CF-PEKK Toray sample 1	101
B.8 Bond line comparison micrographs of tacked CF-PEKK Toray sample 2	101
B.9 Bond line comparison micrographs of tacked CF-PEKK Toray sample 3	101
B.10 Bond line comparison micrographs of tacked CF-PEKK Solvay fibre rich sample 1	102
B.11 Bond line comparison micrographs of tacked CF-PEKK Solvay fibre rich sample 2	102
B.12 Bond line comparison micrographs of tacked CF-PEKK Solvay resin rich sample 1	102
B.13 Bond line comparison micrographs of tacked CF-PEKK Solvay resin rich sample 2	102

E.1	CF-PEEK Teijin: influence of vibrational amplitude on the bond strength	107
E.2	CF-PEKK Solvay: influence of vibrational amplitude on the bond strength	107
E.3	CF-PEKK Toray: influence of vibrational amplitude on the bond strength	108
E.4	CF-PEEK Teijin: influence of vibrational amplitude on the required power	108
E.5	CF-PEKK Solvay: influence of vibrational amplitude on the required power	108
E.6	CF-PEKK Toray: influence of vibrational amplitude on the required power	109

List of Tables

2.1	Storage and loss modulus summary of PEEK, PEKK and PP in the low frequency range	12
2.2	Viscosity of ABS, PS, PP and PE polymers	19
2.3	Face centred central composite design example	26
2.4	Minitab standard format Analysis of Variance result table	28
3.1	CF-PEKK and CF-PEEK UD tape microscopy sample thickness measurements	32
3.2	ImageJ parameters used for the local maxima detection	34
3.3	Results explaining the difference in local maxima observed in the micrographs sections	36
3.4	Theoretical and average measured fibre diameters of Tenax-E and HexTow AS4D fibres	39
3.5	Accuracy analysis results of outer tape surfaces FRR between distribution analysis and localised analysis	43
4.1	Trade-off table peel strength assessment method	46
5.1	Amplitude [%], Pressure [%] and Velocity [mm s^{-1}] used for bond line experiment samples	54
5.2	Tape dependent parameter space for DOE	57
5.3	Contribution of model terms to the response - CF-PEEK Teijin	59
5.4	Contribution of model terms to the response - CF-PEKK Solvay	59
5.5	Contribution of model terms to the response - CF-PEKK Toray	59
5.6	Model summaries of PEEK and both PEKK tapes DOE	60
5.7	Variation ratios R_{BLL} and R_{PF} of the CF-PEEK tape and both CF-PEKK tapes	63
6.1	Peel strength increase with increase of amplitude: DOE vs booster implementation	67
6.2	Differences in measured peel force with velocity increase	69
C.1	DOE peel force results CF-PEKK Teijin	103
C.2	DOE peel force results CF-PEKK Solvay	104
C.3	DOE peel force results CF-PEKK Toray	104
D.1	ANOVA results of CF-PEEK Teijin DOE	105
D.2	ANOVA results of CF-PEKK Solvay DOE	106
D.3	ANOVA results of CF-PEKK Toray DOE	106

List of Acronyms

Adj. MS	Adjusted Mean of Squares
Adj. SS	Adjusted Sum of Squares
Adj. SS_M	Adjusted Model Sum of Squares
ANOVA	Analysis of Variance
ATL	Automated Tape Laying
BLL	Bond Line Length
CCD	Central Composite Design
CF	Carbon Fibre
DF	Degree(s) of Freedom
DMA	Dynamic Mechanical Analysis
DOE	Design of Experiment(s)
DSC	Differential Scanning Calorimetry
ED	Energy Director
FEM	Finite Element Modelling
FRP	Fibre Reinforced Polymer
FRR	Fibre-Resin Ratio
GF	Glass Fibre
MP	Mandrel Peel
PE	Polyethylene
PEEK	Polyetheretherketone
PEKK	Polyetherketoneketone
PP	Polypropylene
PS	Polystyrene
RSM	Response Surface Methodology
SEM	Scanning Electron Microscope
SS	Sum of Squares
SS_M	Model Sum of Squares
SS_R	Residual Sum of Squares
SS_T	Total Sum of Squares
TP	Thermoplastic
TS	Thermoset
UD	Unidirectional
UST	Ultrasonic Tacking
USW	Ultrasonic Welding

List of Symbols

E''	Loss Modulus	N mm^{-2}
E'	Storage Modulus	N mm^{-2}
E^*	Complex Modulus	N mm^{-2}
E	Young's Modulus	N mm^{-2}
T_c	Crystallization temperature	$^{\circ}\text{C}$
T_g	Glass transition temperature	$^{\circ}\text{C}$
T_m	Melting temperature	$^{\circ}\text{C}$
\dot{Q}	Average energy dissipation per unit time and volume	$\text{J m}^{-3} \text{s}^{-1}$
λ	Wavelength	m
ρ	Density	kg m^{-3}
f	Frequency	Hz
k	Thermal conductivity	$\text{W m}^{-1} \text{K}^{-1}$

Introduction

This chapter provides an introduction to this project. Section 1.1 elaborates on the project background and states the necessity of this project. Section 1.2 defines the research questions and briefly describes the research methodology. Section 1.3 outlines the structure of this thesis.

1.1. Project Background

Nowadays the most common type of resin material for fibre reinforced composites are Thermoset (TS) resins [1]. However, fibre reinforced Thermoplastic (TP) composites are starting to become revolutionary materials in the aerospace and automotive industry [2, 3]. In contrast to TS resins, TP resins are capable of becoming liquid upon heating and solid when cooled down. This explains why TP composites are promising in terms of recyclability [1] and have more elegant joining method possibilities [4, 5], what increases the potential of obtaining high production rates [2].

The favourable aspects of TP polymers used in composite parts does result in the need of new, state of the art manufacturing techniques. Boikon BV (Leek, NL) developed the Falko ATL machine in 2018 (figure 1.1). The Falko Automated Tape Laying (ATL) is able to position, locally heat and fix the slitted tapes, what results in a unique combination of processes for TP composite manufacturing. The slitted tapes are the result of the slitting process also developed by Boikon (figure 1.2). Fixation of the Unidirectional (UD) tapes is realized with local heating of the TP resin by utilising an ultrasonic tacking technology. The ultrasonic technology is described in detail in chapter 2. The use of tapes in the ATL process in combination with smart placement and cutting algorithms does result in minimal waste and provides the option of using local reinforcements [6]. The result of the tape laying process is a near nett shape laminate containing locally tacked layers. Consecutive steps are consolidation and forming to the required geometry.



Figure 1.1: Photograph of the Falko ATL at the Boikon facility. Figure 1.2: Photograph of the slitting equipment at the facility of a customer. Obtained from [6]

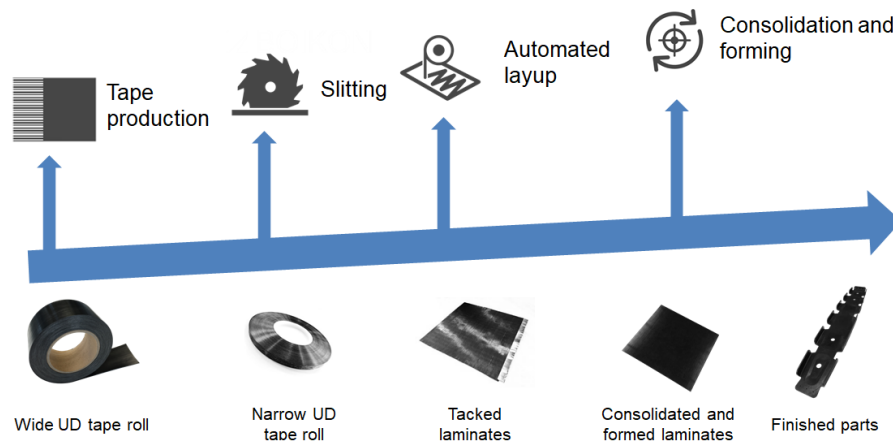


Figure 1.3: Process flow from UD tape production to consolidated final part. Obtained from [6]

Boikon is mainly involved in the slitting and tape laying step of the total TP process flow presented in figure 1.3. Nevertheless, several aspects of the tape production process are still of interest for the company, such as tape quality and differences in tape characteristics. The tacked laminates are further processed by external companies. The final quality of the finished part is the result of the achieved quality of each individual step which implies that Boikon is, to a certain extent, also responsible for the quality of the finished part. Variations in tacking quality are observed at Boikon while using tape materials with different TP polymers and when using apparently identical tapes from different suppliers. The latter is the motivation of the goal of this project, defined as

”Improving the understanding of the Ultrasonic Tacking (UST) process to increase the tape laying speed and preserving the tacking quality of Polyetherketoneketone (PEKK) and Polyetheretherketone (PEEK) UD tapes by providing Boikon with fundamental knowledge related to the most influential parameters, obtained from extensive literature research and validated with experimental work.”

This research project has been initiated on the behalf of Boikon B.V. in order to obtain knowledge regarding the fundamental principles of ultrasonic welding. Understanding of this process with corresponding influential parameters is implemented in the Falko ATL machine to increase tape laying speeds of PEKK and PEEK UD tapes, while preserving the tacking quality. This research project focusses on PEKK and PEEK polymers because their properties are promising for Fibre Reinforced Polymer (FRP) composite parts in the aerospace industry. Increasing the production capabilities of this novel production technique can strongly promote the position of Boikon B.V. in the field of TP composite production.

1.2. Research Questions and Methodology

The main research objective stated above is translated into the following main research question:

’Which UST parameters should be altered, and in which manner, to increase the tape laying speed, while preserving the tacking quality of CF UD tapes containing PEKK and PEEK polymers?’

To answer the main research question using a well defined approach, several more specific sub-questions are derived:

1. Which process parameters are important for the UST process, and what is the influence of those parameters?
 - (a) What is the basic fundamental principle of the UST process used in the ATL manufacturing technique?
 - (b) Based on what is the quality determined of ultrasonic welded thermoplastic materials and can this be used to quantify the tacking quality of the UST technology?

- (c) Which process parameters are involved and in which way do they influence the UST process?
2. Which material properties and characteristics can be related to the tacking quality and how do they influence the tacking quality of the ATL process?
- (a) What type of thermoplastic materials have been tested with the ATL process by Boikon and what are the differences, in terms of properties and characteristics?
 - (b) Which material heating mechanisms are present during conventional Ultrasonic Welding (USW) processes of thermoplastic composites and to which extent are they applicable to the Falko continuous UST technology?

The first research question is answered with a combination of an extensive literature review and experimental work related to the influential parameters. A method to quantify the tacking quality is proposed based on the literature review presented in this report, prior to use this method is thoroughly validated. The fundamental knowledge of USW and relations between parameters are validated for the UST process with a comprehensive Design of Experiment(s) (DOE), studying the influence of parameters to the tacking quality.

Research question two can be answered after more understanding of the different UD tapes, in relation to the tacking quality is obtained. For an improved understanding of the TP in terms of material properties and characteristics, micrographs are obtained and analysed. The type of heating mechanisms presented in the literature review of this report are qualitatively related to the ease of tacking of a specific material in combination with their physical characteristics.

1.3. Thesis Outline

An extensive literature review is presented in chapter 2. This chapter first provides an introduction to ultrasonic technology, consisting of a brief explanation of the ultrasonic components and relevant TP material properties. Besides a more detailed explanation of the physics behind UST, several tacking quality quantification methods are reported. The literature review is concluded with a section describing a statistical method used for the experimental work to study the influence of parameters to the tacking quality. Chapter 3 describes an analysis to characterize the microstructures of the PEEK and PEKK UD tapes, based on cross-section micrographs. The model developed, including the implementation of the Voronoi tessellation algorithm is described. Additionally, results are presented to compare the different tapes analysed. Chapter 4 provides the design of the Mandrel Peel (MP) setup used for tacking quality quantification. Furthermore, design considerations in combination with a thorough validation are presented. Chapter 5 describes experiments related to the bond length of various tacked samples. Besides, the DOE used to determine the relation between influential parameters and the bond strength is described. This chapter is concluded with an experiment analysing the relation between the UD tape microstructure and the variation in bond strength of a tacked sample. Chapter 6 describes the implementation of a different booster for optimization of the UST process in terms of tape laying velocity. This research project is concluded with answers to the research questions in combination with recommendations for further research.

2

Literature Review

A short introduction to the technology of (ultrasonic) welding of Thermoplastic (TP) composites is provided in section 2.1, including a description of the Ultrasonic Welding (USW) components combined with some essential (TP) polymer science. Section 2.2 describes the fundamental principles of USW. Section 2.3 provides methods to quantify the bond strength of tacked Unidirectional (UD) tapes. Section 2.4 explains the basic principles of Design of Experiment(s) (DOE) and motivates why the Response Surface Methodology (RSM) is selected for this research project.

2.1. An introduction to ultrasonic welding technology

Various joining methods for TP polymer materials are listed in figure 2.1. This list of joining methods holds for both fibre-reinforced and unreinforced TP polymer materials. Joining of advanced thermoplastic composites is frequently executed by using fusion methods such as resistance welding, induction welding and ultrasonic welding [5, 7]. Fusion bonding in short is the heating of polymer material at the interface such that the material reaches a viscous state, enabling diffusion of polymer chains across the interface [8]. Resistance welding is based on the Joule's effect where heat is generated using an electric current flowing through a resistive wire mesh placed between the two substrates (parts to weld) [9]. Induction welding relies on an alternating electromagnetic field generating heat by Joule's heating, the dielectric effect and hysteresis losses [10]. Ultrasonic welding can be considered as a friction welding technique due to its high operating frequency and low mechanical vibrational amplitude [9] and produces heat because of surface contact friction and inter-molecular friction [9].

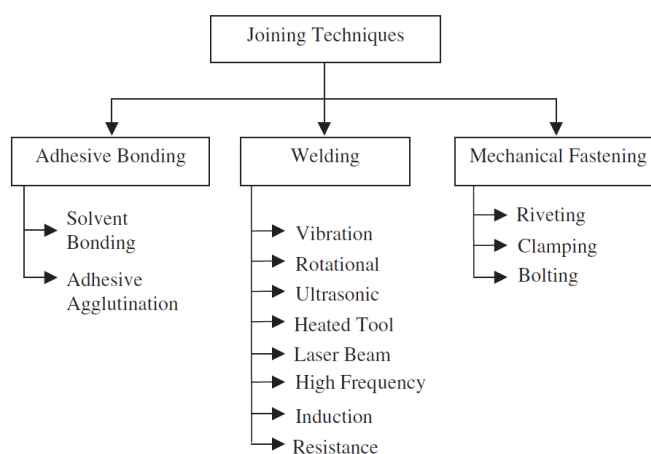


Figure 2.1: Classification of thermoplastic polymer joining techniques. Obtained from [5].

Ultrasonic welding is mentioned as the most promising joining technique for advanced TP composites because this process possesses the largest flexibility in terms of joint design [7, 8]. Figure 2.2 schematically visualizes the basic setup required for USW, note that sonotrode is a more conventional name used for horn [11]. The principle of USW is based on the introduction of mechanical vibrations in the part resulting in heat generation of the TP material [5]. The standard electrical net power is transformed to a higher (ultrasonic) frequency by the power supply [12]. The frequency of sound waves which can be considered as ultrasonic range from 20 kHz to about 1 GHz [13]. However, a majority of studies dedicated to USW utilized frequencies ranging from 15 kHz to 40 kHz, the so called low ultrasonic range [14–16]. The high frequency alternating current from the transformer provided to the converter provides the mechanical vibration of the booster and consequently, the sonotrode [17].

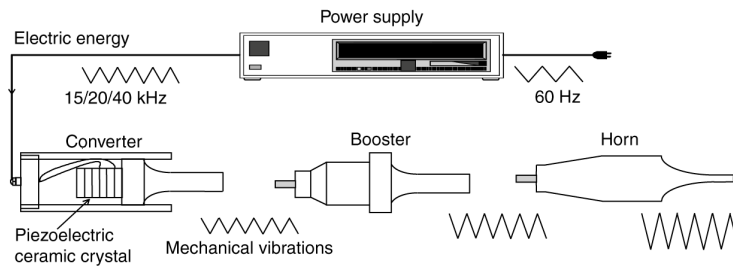


Figure 2.2: Schematic visualisation of main USW components. Obtained from [12].

Compared to the two other fusion bonding techniques mentioned, USW is favoured because no additional foreign material is required [18], bond strengths equal to the parent material strength can be obtained [12], and the process is relatively fast [5, 17, 19]. It should be noted that an Energy Director (ED) is often utilized in the USW process [20, 21]. However, an ED is not considered a foreign material as they generally consist of the same polymer as the Fibre Reinforced Polymer (FRP) composite matrix. Additionally, USW is considered as the process having the largest potential to be automated [22]. Continuous USW is a novel technique in the field of welding consolidated FRP composite parts, the first patent for this process was filed in 2007 [18]. Another advantage for USW is that the welding components and other tooling required for USW can be changed easily and relatively fast what improves the earlier mentioned process flexibility [23].

In contrast to induction welding [5] and resistance welding [24], physical contact between the part and the hot equipment is present for USW. Nevertheless, thermal degradation of the surface material can be prevented because heating of the sonotrode is limited [12], whilst the interface experiences sufficient heat for a fusion bond. If required, the sonotrode can be cooled by using compressed air [17, 25]. As properly addressed by Potente [19], the favourable aspects of USW can only be obtained if the process is tailored in a precise manner, in order to fit the process with the parts to be welded.

2.1.1. Description of ultrasonic welding components

A conventional USW stack consists of three mechanical connected main components, namely the converter, the booster and the sonotrode [23]. Additionally, the function of the actuator is also explained in this paragraph. Figure 2.3 does schematically depict the USW stack, including the development of stress and amplitude throughout each component. Large stresses are observed, due to stress concentrations where the cross-sectional area of a component rapidly changes [26]. The components of the USW stack are designed such that their length is approximately equal to the half-wavelength, one wavelength can be calculated using

$$\lambda = \frac{c}{f} \quad (2.1)$$

where c and f are the speed of sound in a specific material and the frequency of the operating ultrasonic system, respectively [17]. A proper tuned USW stack ensures a maximum vibration amplitude at the tip of the sonotrode for a specific operating frequency, meaning that the booster and sonotrode are designed such that they are in resonance at the operating frequency. Tuning of the components to a frequency other than the operating frequency leads to an inefficient transmission of energy and can eventually lead to damaging the components [27].

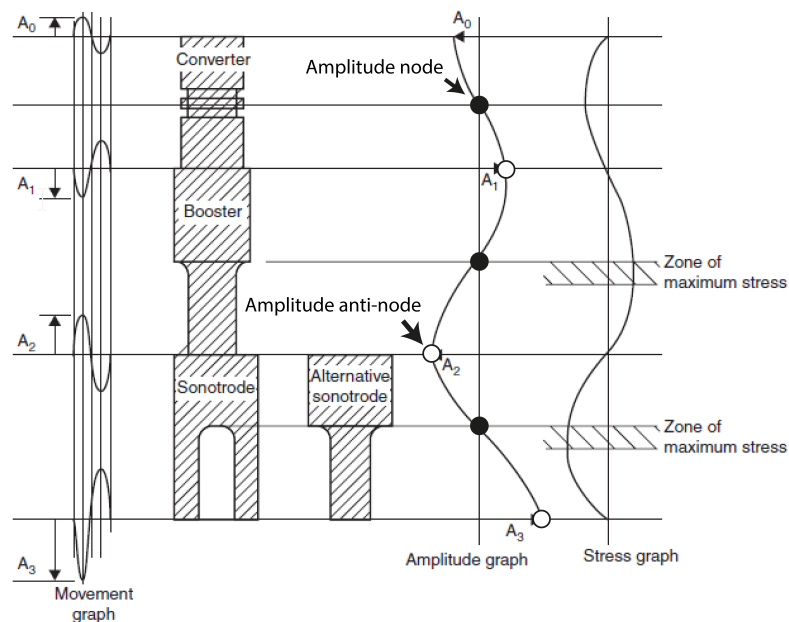


Figure 2.3: Development of vibrational amplitude and stress in the USW components. Obtained from [12].

Converter

The upper part of the ultrasonic stack is called the transducer, or converter [5]. This component transduces the electrical energy to mechanical energy, in general by using the piezoelectric effect. Piezoelectricity is mainly used because of the efficient way of transferring electric energy to mechanical energy [17]. The reversed or indirect piezoelectric effect causes stress in the piezoelectric material, due to the applied electric field, resulting in an expansion or contraction of the piezoelectric material [28]. The piezoelectric effect is initiated by dipole moments which occur due to charge imbalances in molecules. Multiple dipoles pointed in the same direction are called domains. Each individual domain has its own dipole moment of own direction. By applying an electric field, these individual domains align in such a way that the random dipole moments become aligned. This change of orientation causes stress in the material and thus a mechanical excitation for the duration of the applied electric field [29]. According to the matrix equation presented in [30], the equation to calculate the mechanical excitation of a piezoelectric element is

$$\Delta y = d_{33} * V \quad (2.2)$$

where d_{33} ($[\text{mm V}^{-1}]$) and V ($[\text{V}]$) represent the piezoelectric constant of the material and the voltage applied, respectively.

A high frequency oscillatory mechanical motion can be obtained when instead of a constant electric field, an alternating high frequency electric field is applied. In this case the piezoelectric material inside the convertor constantly contracts and expands resulting in the high frequency vibration.

Booster

The component beneath the converter, the booster, is either used to increase or decrease the amplitude provided by the converter [23]. Besides the amplification function, the booster also provides a mounting point to connect the ultrasonic stack to the actuator. A metal ring is commonly used to function as mounting point. At this mounting position, often called the nodal point, the amplitude of vibration is (roughly) zero. The booster can influence the amplitude by having an unequal mass distribution along the booster length. When an amplitude increase is desired, considering the conservation of momentum law, a larger mass should be positioned at the top of the booster [17]. In other words, once the heavier upper part of the booster, m_{high} is in motion, the lower part containing m_{low} , experiences a faster motion having a larger amplitude. The gain of the booster is defined as the ratio of amplitude at the top to the amplitude at the bottom, which is proportional to the mass differences. Amplitude reduction boosters can be required when large gain factors are needed for the sonotrode, preventing not tunable situations to occur [12].

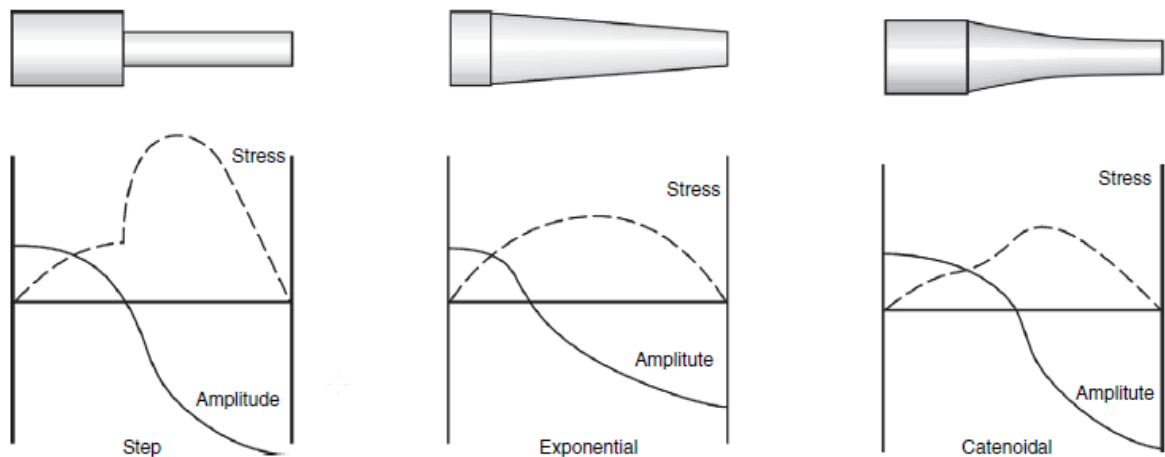


Figure 2.4: Influence of sonotrode shape to vibrational amplitude and stress distributions. Obtained from [23].

Sonotrode

The component transferring the mechanical vibrations from the ultrasonic stack to the part is called the sonotrode, and is commonly machined from aluminium or titanium [31]. The mechanical vibrations can be transferred to the part in a transverse [26] and longitudinal fashion [7, 9, 32, 33], the latter is considered more conventional. A variety of sonotrode shapes are used in the past based on specific needs of the production process [26, 27, 34–37]. Custom sonotrodes are common case because they are designed such that they perfectly fit the material used, the operating frequency utilised and the gain required [27]. For continuous USW processes, the sonotrode commonly has rounded edges at the tip [31]. This is utilized to obtain a more gradual increase of vibrational energy until a steady state amplitude condition is reached.

As depicted in figure 2.4, the shape heavily influences the stress and amplitude distribution along the sonotrode. With a stepped sonotrode, a gain factor of 1:9 can be obtained [23]. However, it is explained that achieving such high gain factors with a stepped sonotrode is challenging because of the presence of large stresses in the sonotrode. This introduces the balance the engineer should consider between obtaining a high vibrational amplitude and maintaining low stresses levels. This is especially challenging for sonotrodes in automated and continuous processes since those are more prone to fatigue issues [38].

The sonotrode should be designed such that the resonance frequency of the sonotrode is at, or close to the operating frequency [12]. This reflects on the length of the sonotrode for standard sonotrode shapes [27, 34–37, 39]. In general, sonotrodes having a basic geometry can be designed using simple exact equations whereas more complex shapes require empirical relations. Numerical modelling projects can be utilized for complex sonotrode shapes which consequently removes the necessity to use empirically derived data [26, 27, 34–37]. As an example, resonance frequencies were found in the first (i.e. fundamental) mode for stepped, conical and cylindrical sonotrode geometries [37]. However, realising a maximum displacement at the sonotrode tip is not necessarily obtained in the fundamental harmonic mode. Kim et al. [26] presented a modal analysis for a specific 20 kHz sonotrode, obtaining a natural frequency of 19.584 Hz in the 10th harmonic mode. This example emphasizes the need of Finite Element Modelling (FEM) analysis for complex sonotrode geometries to tune the resonance frequency of the sonotrode close as possible to the operating frequency of the welding system.

Actuator

Many studies [20, 32, 33, 40] in the field of welding TP polymer materials address the effect of the applied force on the weld strength. For this reason, the actuator is considered as an important component for the USW process. The static welding force is commonly applied using pneumatic cylinders to ensure intimate contact at the weld interface in a controlled and repeatable manner [12, 23]. The aforementioned components of the USW stack are generally attached to the actuator at the zero amplitude node of the booster, as depicted in figure 2.3 [17]. The use of 'dual-pressure control' actuators is

described by Yeh [12] which entails that the pressure applied is high in the initial phase of the process, whereas the applied pressure is lowered as the USW process progresses. This method facilitates that the applied force can vary throughout the process according to the different needs as described in section 2.2.6 [23]. Implementing this approach in a continuous ultrasonic tacking or welding process is challenging, if not impossible and has not been researched in the past by other researchers.

2.1.2. Thermoplastic Material Properties for Ultrasonic Welding

This paragraph briefly elaborates on some basic polymer science, a more detailed explanation of the dynamic moduli is provided next. Furthermore, viscoelasticity of TP polymers is described. This paragraph is concluded with some relevant polymer material properties of Polyetheretherketone (PEEK) and Polyetherketoneketone (PEKK).

Basic Polymer Science

Polymer materials are created using various polymerisation techniques [24, 41], where the degree of polymerisation indicates the number of repeating units in the polymer backbone [42]. Polymers, are generally divided using three groups; thermoplastics, thermosets and elastomers [41]. The categorisation between these polymer classes is based on the interaction between individual polymer chains [24]. In other words, based on intermolecular forces. A thermoset polymer is one large cross-linked three-dimensional network polymer with strong chemical covalent bonds [41]. A thermoset cannot be recycled and becomes infusible once the chemical reaction during the polymerisation process is finished [24]. Elastomeric polymers contain chemical van der Waals bonds which are much weaker compared to the strong covalent bonds [41]. Thermoplastic polymers, consisting only of individual polymer chains do not have chemical bonds and are held together by entanglements of chains, acting as physical bonds [17, 41]. Heating and cooling of TP polymers is a repeatable process due to the lack of these chemical bonds, hence the ability for TP polymers to melt and solidify upon cooling [29, 41].

A different method to classify polymers is based on the level of crystallinity [24]. Crystalline regions, or crystals are regions of orderly packed polymer chains [41]. Polymers containing only ordered regions of polymer chains are called crystalline polymers. However, 100% pure crystalline polymers are impossible to realize. Polymers having no ordered arrangement in their molecular structure are denoted amorphous and polymers with a combination of ordered and random regions are semi-crystalline polymers [24].

TP Polymer Dynamic Moduli and Transition Temperatures

Mechanical properties of polymer materials are commonly characterized using Dynamic Mechanical Analysis (DMA) techniques [43]. The outcome of this analysis is a data set for E' , E'' and $\tan \delta$ over a range of temperatures. The storage modulus, E' describes the elastic response of a polymer which can be related to the stiffness of a polymer [43, 44]. The main difference between Young's modulus and the storage modulus is the fact that Young's modulus is measured statically whereas the storage modulus is measured in a dynamic situation [41]. Additionally, The viscous response of a polymer is described by the loss modulus E'' which is related to the damping behaviour of a polymer. In energy terms, E' can be described by the tendency to store the applied energy and E'' by the tendency to dissipate the applied energy [43]. Considering the potential energy balance, the storage and loss modulus can be described according to figure 2.5 [12]. E' describes the energy which remains in the systems whereas E'' represents the lost energy, which is dissipated to heat. The ratio E'' to E' is defined as $\tan \delta$ [41].

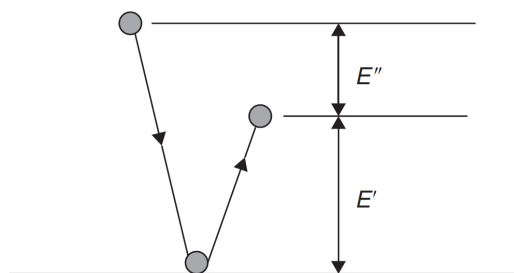


Figure 2.5: Visualisation of storage and loss modulus. Obtained from [12]

The storage and loss modulus in combination with $\tan \delta$ are presented over a range of temperatures in figure 2.6, which are typical DMA graphs for amorphous and semi-crystalline polymers [45]. While increasing the temperature, a small decrease in E' can be observed for both type of polymers, this is related to segmental polymer chain motion meaning a slight decrease in polymer stiffness. A large drop in E' can be observed close to the T_g which is referred to a first order transition due to the motion of complete polymer chains [41]. The glass transition is often referred to the glass to rubber transition phase [41]. It should be noted that the T_g is often a range of temperatures because in many fields of science the T_g is defined slightly different [43]. Nevertheless, in this report the T_g will be referred to the temperature showing a peak in the E'' graph, as presented in figure 2.6. The glass transition temperature characterizes the regions of random polymer chain arrangement and is therefore present in the amorphous and semi-crystalline graph [43]. The drop in E' can be explained by the fact that the vibrational motion of molecules increase while increasing the temperature [24]. In a pure hypothetical case, a crystalline polymer does not have a T_g because increased molecular vibration is restricted due to the confined space of highly ordered molecular chains [43]. In case of a semi-crystalline polymer, a second drop in E' is observed at the T_m of the polymer. This almost complete loss of stiffness is because sufficient energy is available to disrupt the ordered arrangement of the crystal structure [24].

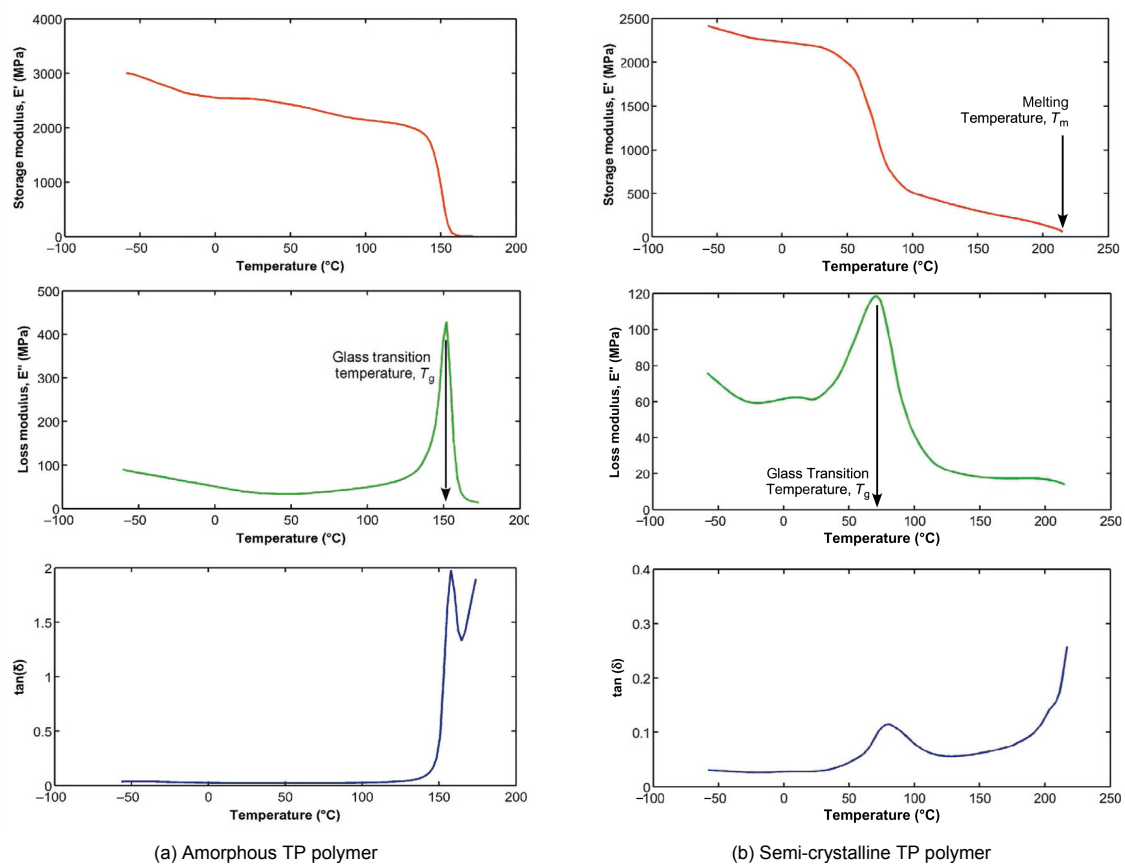


Figure 2.6: Amorphous and semi-crystalline polymer dynamic mechanical properties. Obtained and modified from [31]

The loss modulus graph for both polymers show a large increase at the T_g . The loss modulus displays a large peak at this specific temperature because of the large amount of energy put in the polymer which is not returned due to the glass to rubber transition [41]. As one can imagine, the processing temperature for amorphous polymers is above the T_g whereas T_m is the target temperature for processing semi-crystalline polymers [8].

The storage and loss modulus of a polymer are frequency dependent [41, 46] and are often measured at low frequencies because of limitations of the available equipment [7]. In general, $\tan \delta$ and E'' are small at very low and very high frequencies and contain a peak at intermediate high frequencies [41]. The storage modulus is generally low at low frequencies where the polymer displays rubber behaviour

and high and higher frequencies where the polymer behaves glassy. By increasing the frequency, the value of E' increases drastically in the intermediate viscoelastic frequency regime whilst $\tan \delta$ and E'' both show a maximum in this frequency range [41]. Extrapolation methods are commonly applied [7, 32, 47, 48] to know the behaviour of E' , E'' and $\tan \delta$ over a range of temperatures at a frequency higher than the maximum achievable testing frequency. Such technique is not utilised for the current project, and is therefore not explained in detail.

Besides the T_g and T_m , the crystallization temperature T_c is an important material property when welding semi-crystalline polymers [49]. Crystal regions are formed upon cooling of semi-crystalline polymers from the T_c up to the T_g , crystals cannot be formed below the T_g because of the amount of energy required to form an ordered arrangement of polymer chains [41, 49]. As a side note, the crystallization temperature is highly sensitive to the cooling rate employed in the Differential Scanning Calorimetry (DSC) equipment [50]. The crystallization temperature is defined as the temperature at which the change in specific volume due to crystallization reaches five percent of the overall change [51]. This entails that upon relatively fast cooling, the T_c tends to decrease due to limited possibilities to form crystal structures meaning that the 5% of change is reached in a later stadium.

Viscoelastic Behaviour of Thermoplastic Polymers

In contrast to traditional materials, which are either considered elastic solids or viscous fluids, TP polymers can be considered as viscoelastic materials [41]. This type of material behaves elastically when subjected to low temperatures and high strain rates whereas viscous behaviour can be observed while applying small strain rates at elevated temperatures. As a basic principle, viscoelasticity can be described considering the behaviour of a spring and dashpot combined. Figure 2.7a schematically depicts the behaviour of a spring which is subjected to the sinusoidal load [31]. Integrating the power curve over one cycle does result in zero energy dissipation, meaning that all stored energy upon loading is fully recovered after unloading ($E'' = 0$).

The dashpot model is depicted in figure 2.7b. The velocity in this case, is in-phase with the applied force due to the pure damper effect [31]. From this it can be derived that a dashpot dissipates all provided energy into heat ($E' = 0$) as the power curve shows purely positive work.

Viscoelasticity can be described using a combination of a spring and a dashpot in series, see figure 2.7c. The displacement and velocity graphs have similar shapes compared to those of the spring model but are slight out-of-phase due to the damping aspect of the dashpot [31]. The magnitude of the out-of-phase component depends on the damping part of the viscoelastic polymer material. The power curve shows that more energy is put into the system compared to what is restored ($E', E'' \neq 0$). This can be mathematically substantiated by integrating the area above the horizontal axis and subtracting the integral of the area below the horizontal axis. The remainder of this energy in the material is dissipated into heat [31]. Section 2.2.2 describes in more detail the relevant heating mechanisms for USW.

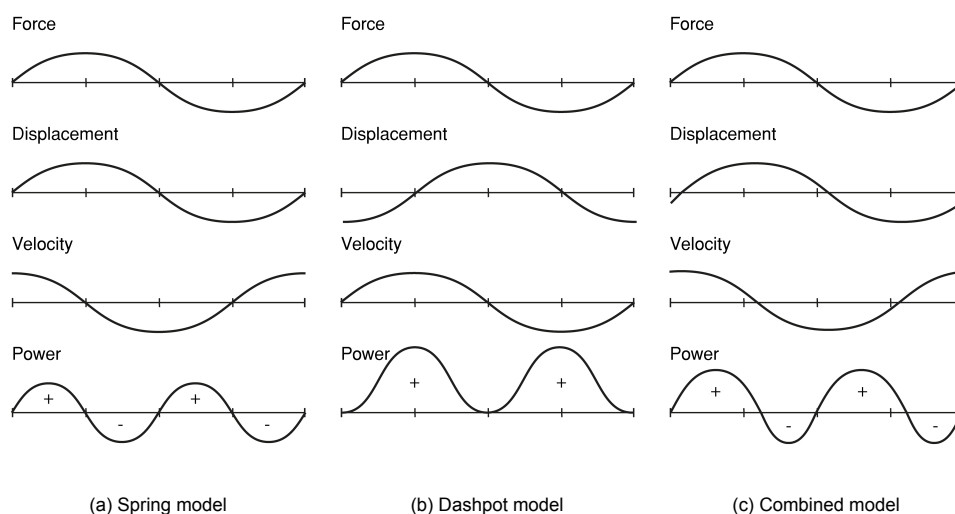


Figure 2.7: Three different cyclic loading viscoelasticity models. Obtained and modified from [31]

PolyEtherKetoneKetone and PolyEtherEtherKetone Properties

PEKK and PEEK are the polymer materials of interest for this research project, and are therefore briefly elaborated on in this section. Polypropylene (PP) is added for comparative reasons. The fast increase of interest for PEKK and PEEK composite products in the aerospace industry is related to the favourable mechanical and thermal properties [52]. The high mechanical properties can be related to the absence of many single bonds and the presence of benzene rings (C_6H_6) in combination with double bonds [41, 53, 54], which for example lack in the repeating unit of PP [55]. The difference between the presence of strong and weak bonds in the molecular structures can directly be related to the dynamic moduli of PEEK, PEKK and PP presented in table 2.1 [41, 42]. Because of the frequency dependent properties and the lack of available data which match the operating frequency of the Ultrasonic Tacking (UST) equipment, E' and E'' are provided in the low (measurement equipment) frequency range. This ensures the most accurate comparison possible without utilising DMA equipment and performing extrapolation techniques. The T_g and T_m are also included in table 2.1. These temperatures obtained from literature can vary slightly because the glass transition and melting do not occur at one specific temperature, and both temperatures are often defined in a slightly different manner [41]. Besides, T_m and T_g depend on the many other aspects such as rate of cooling and processing steps involved in the polymer synthesising process [50].

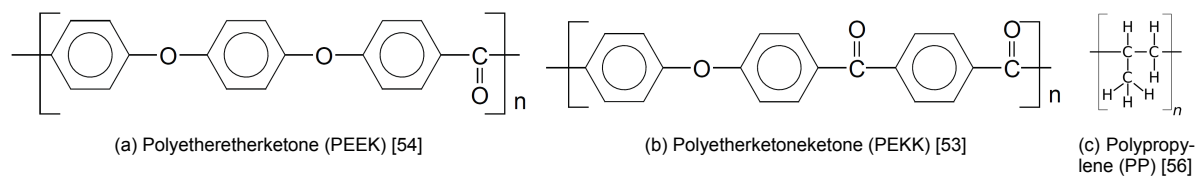


Figure 2.8: Molecular structure repeat units of PEEK, PEKK and PP

	PEEK	PEKK	PP
E' [GPa] (f [Hz])	3.8 (1) [57]	3 (0.2) [58]	1.1 (1) [59]
	4.0 (3.5) [7]	3 (0.2) [60]	1.7 (1) [61]
E'' [GPa] (f [Hz])	0.016 (3.5) [7]	0.010 (0.2) [58]	0.10 (1) [62]
	0.025 (1) [57]	0.015 (0.2) [63]	0.11 (1) [61]
T_g [°C]	143 [64]	160 [65]	10 [62]
	145 [52]	159 [66]	15 [61]
T_m [°C]	334 [54]	334 [65]	163 [67]
	350 [52]	337 [66]	170 [62]

Table 2.1: Storage and loss modulus summary of PEEK, PEKK and PP in the low frequency range

2.2. The Physics of Ultrasonic Welding

This section covers the physics of USW, what can be described using five steps [7]. The five interrelated sub-processes are described by 1; mechanical vibrations of the equipment and part (section 2.2.1), 2; heating of the TP material (section 2.2.2), 3; heat transfer in the part (section 2.2.3), 4; squeeze flow and wetting of the TP polymer (section 2.2.4) and finally, 5; the interaction of the polymers at the surface described by inter-diffusion and entanglements (section 2.2.5).

2.2.1. Wave propagation and attenuation

Sound and energy fringe patterns introduced by a sonotrode were captured (figure 2.9) in a rod placed on a steel anvil support [19]. Zones of maximum vibrational amplitude (upper photograph) and maximum stress and strain (lower photograph) were observed at different locations in the rod, schematic visualized in the graph. According to figure 2.9, the location of maximum stress/strain closest to the sonotrode (σ_1, ϵ_1 at $x = \lambda/4$) shows fusion of the polymer, in contrast to the location of σ_2, ϵ_2 at $x = 3\lambda/4$ where no polymer fusion was observed. Equation 2.3 was used to describe the locations X of maximum vibrational amplitude in the rod where λ represents the wavelength as calculated with equation 2.1. Note that $X = 0$ at the sonotrode tip. Based on the fringe patterns provided, the zones of

maximum stress/strain (equation 2.4) can be described with a quarter wavelength phase shift with respect to equation 2.3. The locations of maximum stress and maximum strain do not perfectly coincide in reality because of viscoelastic behaviour of TP polymers (force and displacement graph in figure 2.7c). For simplicity this effect is neglected in the remaining part of this section.

$$X_{A_{max}} = \frac{n\lambda}{2} \quad n = 0, 1, 2, \dots \quad (2.3)$$

$$X_{\sigma_{max}, X_{\epsilon_{max}}} = \frac{n\lambda}{2} + \frac{\lambda}{4} \quad n = 0, 1, 2, \dots \quad (2.4)$$

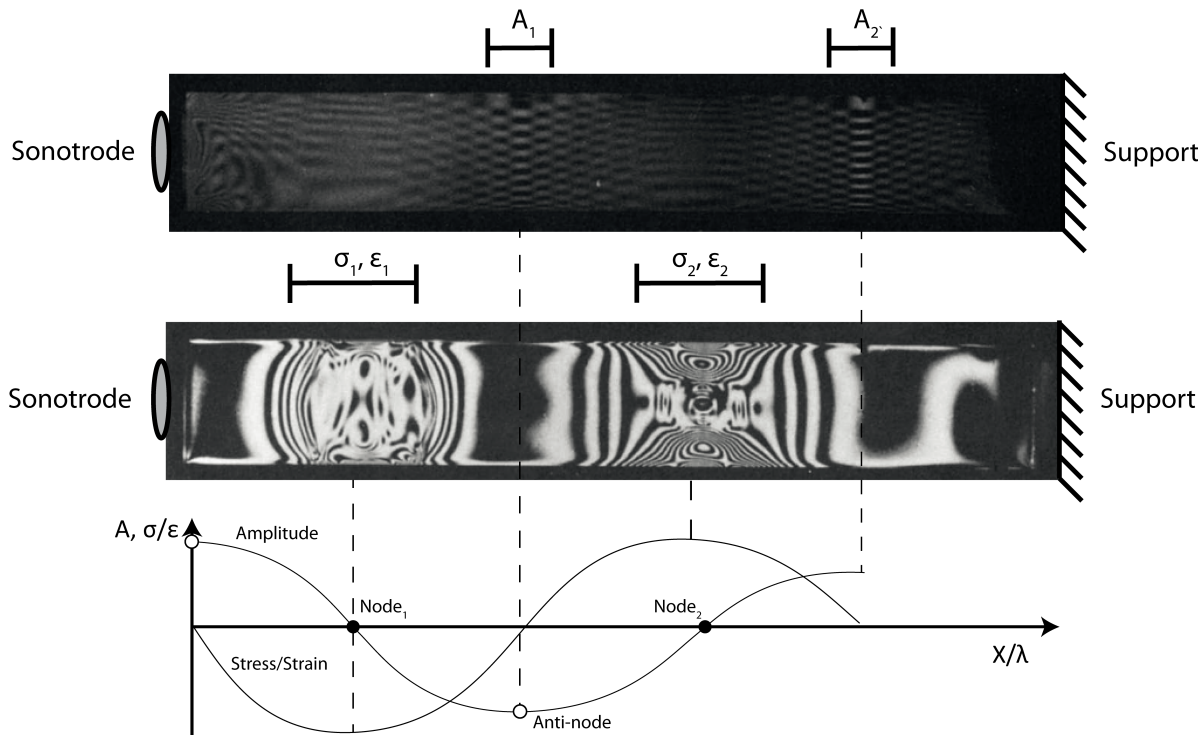


Figure 2.9: Captured sound (top) and energy conversion (middle) fringe patterns in a rod. Included with stress/strain and amplitude graph for a linear viscoelastic material over one wavelength. Obtained and modified from [19, 68]

The difference in location between the maximum vibrational amplitude and maximum stress/strain can be explained using the following description. Due to the harmonic motion of the sonotrode tip, longitudinal standing waves of vibrational amplitude are introduced in the part [23]. The wave form can be considered as a longitudinal wave because the vibrational amplitude is in the same direction as the direction in which the wave propagates [13]. Standing waves are characterized by static waves having nodes (zero vibrational amplitude) and anti-nodes (maximum vibrational amplitude), as depicted in the graph of figure 2.9. The horizontal axis in this graph presents the through thickness direction starting at the upper surface of the part. The phase difference between the stress/strain and displacement graph can be understood when considering the motion of individual particles [13, 69]. A particle at a displacement node does in theory not move whereas particles slightly to the left and right of this node constantly move. Because these particles move in opposing directions compression and rarefaction effects are present. This constant change in stress state, at any location except for the displacement nodes, results in fluctuating strain in the material. As one can imagine, particles further away from the displacement node have a larger relative motion resulting in larger stresses as presented in the graph of figure 2.9. The stress depicted in this graph is associated with the strain in the material. The distinction between the location of maximum vibrational amplitude and polymer fusion can be explained by this analysis when one considers that heat generation is related to internal strain [19]. A more detailed relation between the internal strain and heat generation is presented in section 2.2.2.

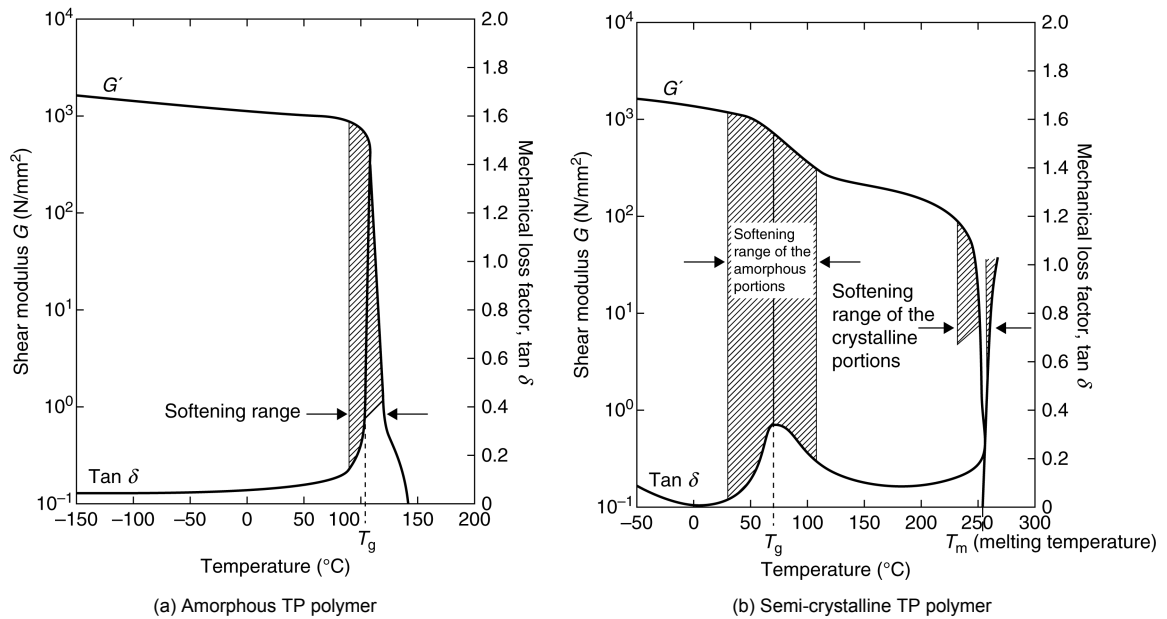


Figure 2.10: Influence of shear modulus and $\tan \delta$ on temperature change for amorphous and semi-crystalline polymers. Obtained from [12]

No fusion of TP polymer was observed at and near the location of the second displacement node because the ultrasonic waves attenuate as they propagate [68]. The attenuation of waves originates from the dissipation of energy into heat, what is directly related to E'' [17]. The importance of E' and E'' in relation to ultrasonic wave propagation and attenuation for amorphous and semi-crystalline polymers is presented in figure 2.10. Note that this figure contains the shear modulus G' instead of E' . However, graphs of both moduli can be considered the same as they present the same behaviour at T_g and T_m , if applicable [41]. Welding amorphous polymers using ultrasonic technologies is less challenging compared to welding semi-crystalline polymers because of the disorder in molecular structure arrangement, meaning that little energy is required to realize a bond [20]. In other words, E' remains relatively large up to T_g for amorphous polymers resulting in a small amount of attenuation of ultrasonic waves up to the interface [12, 70]. It is observed in figure 2.6b that E' is rather low after passing the T_g for semi-crystalline polymers. Ultrasonic waves in this phase of the process are mostly attenuated instead of propagated to the interface, due to the relatively low E' . Up to the temperatures close to the T_m the ultrasonic energy is dissipated into heat in the amorphous regions rather than transmitted to the interface [12]. In other words, the ultrasonic waves get damped in the amorphous portions of the semi-crystalline polymer [70]. The depicted narrow softening range in figure 2.10 can be explained by the large decrease in mechanical properties while approaching the T_m , preventing ultrasonic waves from propagating through the material [8, 12].

The distance between the upper surface of the part and the welding interface is a measurement of dividing the USW process in two groups namely, near-field and far-field welding [17, 32]. For near-field welding, the distance between the sonotrode and the interface is small compared to the wavelength of the induced sound wave. In agreement with the attenuation behaviour of ultrasonic waves and the dissipation of ultrasonic energy into heat, it is concluded that welding in the far-field is a challenging process [19]. For such processes, the materials should be selected with care and the welding interface should be positioned at a displacement node, thus a strain anti-node [19, 68, 71]. In case of near-field welding, the vibrational amplitude at the welding interface is close to the vibrational amplitude of the sonotrode [8, 17], meaning that attenuation of vibrational amplitude can be completely neglected in the near-field regime [72].

The E' and E'' values presented in table 2.1 in combination with T_g and T_m emphasize why ultrasonic welding of composites containing TP polymers used for structural applications in the aerospace industry (PEEK and PEKK) is more challenging compared to TP polymers having lower mechanical properties

such as PP [7]. High mechanical properties, such as stiffness are inherently linked to the degree of crystallinity quantifying the ordered regions in the molecular arrangement [41, 73]. Such polymers behave more 'spring-like' resulting in more stored energy, as explained by the basic dashpot-spring model presented in section 2.1.2 [20].

2.2.2. Heating Mechanisms

The relation between the stress/strain distribution in the part, and the generation of heat is elaborated on in this section. Early studies showed that heating in the USW process occurs because of frictional heating at the surface in combination with internal viscoelastic heating due to internal strain oscillations [33]. Nevertheless, some of the studies acknowledge viscoelastic heating as the main heating mechanism and neglect the effect of surface frictional heating [7, 33, 74] whereas others consider the latter as an important source of heat generation [9, 48, 75]. While observing the six studies mentioned, it was found that this difference was in relation with the physical surface contact area at the interface prior to welding. Studies utilising an energy director (explained in section 2.2.6) covering only a small portion of the complete welding interface area indicated viscoelastic heating as the main heating mechanism. Frictional heating was considered an important source of heat generation when the energy director covered the complete interface area. In the Automated Tape Laying (ATL) process much contact between the two parts is present, for this reason both heating mechanisms are considered and presented below.

Viscoelastic Heating

Viscoelastic heating, often referred to as volumetric heating, originates from molecular friction (i.e. molecules which rub against each other) [20]. The dissipation equation of ultrasonic energy [$\text{J m}^{-3} \text{s}^{-1}$] (i.e. heat generation) in a viscoelastic material can be derived based on the work done of a single ultrasonic vibration cycle. The heat generation of a unit cell per unit time, due to the internal friction between molecules can be described as

$$\dot{Q} = f \oint \sigma(t) d\epsilon(t) = f \sigma_0 \epsilon_0 \omega \int_0^{2\pi/\omega} \sin(\omega t) \cos(\omega t - \delta) dt = f \pi \sigma_0 \epsilon_0 \sin \delta \quad (2.5)$$

where f is the vibration frequency of the ultrasonic system, ω the angular velocity ($\omega = 2\pi f$), δ the out-of-phase angle and the dimensionless stress and strain amplitudes are σ_0 and ϵ_0 , respectively [47]. The loss modulus of a polymer can be derived as

$$E'' = \left(\frac{\sigma_0}{\epsilon_0} \right) \sin \delta \quad (2.6)$$

and can be substituted in equation 2.5, resulting in equation 2.7 [47, 75]. The latter can be considered as the generalized equation to calculate the average energy dissipation due to viscoelastic heating per unit time [7, 20, 47].

$$\dot{Q} = \frac{\omega \epsilon^2 E''}{2} \quad (2.7)$$

Studies using thermocouples to measure the temperature inside TP parts during USW observed low heating rates at relatively low temperatures which tremendously increased at higher temperatures [33]. The increased heating rate is explained by the increase of E'' near the T_g , resulting in more energy dissipation as explained by equation 2.7.

Surface Frictional Heating

On microscopic level, composite parts do have surface irregularities [76]. Such irregularities, often referred to as asperities experience larger internal strains compared to the rest of the TP polymer material. Higher heating rates can be observed at the welding interface compared to the body of the TP composite part [33]. Larger strain amplitudes, in combination with the non-linear relationship between the energy dissipation and the strain amplitude as described by equation 2.7 provide the reason why such high heating rates are observed at the interface. Reduction in frictional heating can occur at elevated temperatures close the flow of the polymer which is high likely due to the removal of the surface asperities. For surface frictional heating to occur sufficient intimate contact between the upper and lower substrate is required, which can be achieved by applying a pressure throughout the welding cycle [9].

2.2.3. Heat Transfer

Heat transfer can be described as the flow of heat, originated from an energy director, to cooler regions in the part [7]. Although the transfer of heat from warm regions to cooler regions in pure TP polymer USW can be neglected [33], it is acknowledged as an important aspect for welding FRP composites [7]. The heat transfer in FRP composites must be considered as anisotropic because of the large differences in material conductivities [7, 48]. As a comparison, Polystyrene (PS) does have a thermal conductivity k of approximately $0.16 \text{ W m}^{-1} \text{ K}^{-1}$ [77], which is relatively close to the thermal conductivity of PEEK ($0.29 \text{ W m}^{-1} \text{ K}^{-1}$) [64]. For a standard carbon fibre the thermal conductivity is larger than $400 \text{ W m}^{-1} \text{ K}^{-1}$ [64]. Putting this in perspective, aluminium has a thermal conductivity of $247 \text{ W m}^{-1} \text{ K}^{-1}$ [78]. The observed difference in thermal conductivity of neat polymer material and fibres is also present when the thermal conductivity of a composite laminate is expressed in longitudinal, transverse and through thickness direction. The thermal conductivity of 0.15 mm thick Carbon Fibre (CF) UD tapes containing a TP Polyamide-12 (PA12) polymer, analysed for laser assisted thermoplastic welding, is $7.78 \text{ W m}^{-1} \text{ K}^{-1}$ in fibre direction (longitudinal direction) and only $0.46 \text{ W m}^{-1} \text{ K}^{-1}$ in transverse and through-thickness direction, which is relatively close to the thermal conductivity of neat PA12 of $0.23 \text{ W m}^{-1} \text{ K}^{-1}$ [79]. The numbers in the aforementioned examples emphasize the necessity of considering the anisotropic heat transfer in USW for FRP composite parts containing CF.

2.2.4. Squeeze flow and wetting

Squeeze flow of resin occurs once the temperature at the interface is sufficient high enough, above T_g for amorphous and above T_m for semi-crystalline polymers [7, 48]. The wetting of the substrates due to squeeze flow of polymer material depends on the viscosity of the molten polymer [7]. Additionally, surface wetting is also influenced by the degree of crystallinity of the polymer because wetting becomes confined with an increased degree of crystallinity [5]. Once the squeeze flow wets the interface either partially or complete, polymer chains can start to diffuse across the interface [5, 80] as explained in the succeeding section. Intimate contact between the two substrates is accomplished once complete wetting occurred [49].

2.2.5. Bonding Mechanisms

As with the other fusion bonding methods described in the introduction of this report, bonding of two materials using USW relies on inter-diffusion and entanglements of TP polymer chains across the welding interface followed by consolidation of the TP polymer [49, 80]. Molecules are always in motion, even at room temperature [49]. Diffusion or reptation can be explained by the relative motion between molecules [33, 81]. At elevated temperatures the relative motion between molecules increases and diffusion of polymer chains across the interface can occur when intimate contact is ensured by applying a welding force, so called inter-diffusion [49, 81]. Removal of the interface between two thermoplastic polymers is often referred to as healing of the material [81]. Healing of a TP polymer is described using a five step approach by Wu et al. [80], as depicted in figure 2.11. The first two steps are not relevant for describing the fusion of materials for USW since these steps describe the ability of a polymer chain end to initiate diffusion immediately after fracture [82]. Step 3, as visualized in figure 2.11, is in agreement with the 'flow and wetting' step mentioned in the first paragraph of this chapter. Surface wetting during the process of USW is initiated at T_g and T_m for amorphous and semi-crystalline polymers, respectively [81]. Step 4 describes the initial inter-diffusion phase where only short segments have slightly diffused across the interface [80] without realising any entanglement. Step 5 describes the complete diffusion and entanglement of individual polymer chains across the interface [49, 80]. The end of the polymer bonding or healing step, in theory is accomplishing a bond strength equal to the strength of the virgin material [82]. The time required for inter-diffusion to take place is in the order of 10^{-7} seconds [7].

Besides the process parameters described above, the degree of crystallinity is an important polymer characteristic to consider when describing bonding mechanisms and the final bond strength [49]. When the temperature at the interface drops below T_c , the formation of crystals is initiated. The ability of semi-crystalline polymer chains to diffuse is drastically decreased upon the formation of crystals because of the lowered chain mobility [49]. In general, formation of crystals prior to inter-diffusion and entanglement is disadvantageous for the weldability of semi-crystalline polymers whereas formation of crystals after the chains have diffused and entangled improve the weldability, as it increases the bond strength.

$$\sigma = f(T, p, t, \phi_c) \quad (2.8)$$

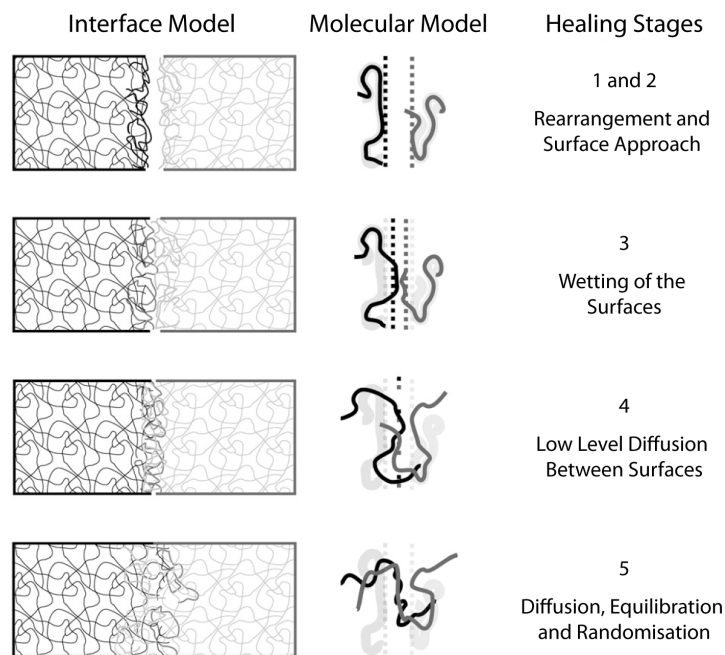


Figure 2.11: Bonding steps for inter-diffusion of polymer chains across welding interface. Obtained and modified from [80]

Equation 2.8 describes the bond strength as a function of the interface temperature T , the applied pressure p , the processing time t and the degree of crystallinity ϕ_c [49, 81]. This equation, in combination with the polymer nature as described above, shows that realising a strong bond is a complex process depending on many process and material aspects.

2.2.6. Parameter Influences to Ultrasonic Welding

This section describes knowledge obtained from literature regarding influential parameters and their corresponding effect to the USW process. The effects of the vibrational amplitude, welding force, welding time, frequency and energy directors are described.

Amplitude

The first parameter described is the vibrational amplitude of the sonotrode tip. According to section 2.2.2, a direct relation exists between the amplitude of the sonotrode tip (vibrational amplitude) and the strain in the material (strain amplitude, ϵ in equation 2.7), independent on the propagation and attenuation of the longitudinal waves in the material. In other words, a larger sonotrode amplitude results in an increase of material displacement, and consequently a larger strain amplitude. In work related to USW of PEEK APC-2 composites, Benatar and Gutowski [7] describe the effect of the sonotrode amplitude. The USW stack was equipped with various boosters having different booster gains. Specimens were not welded using a 1.5 gain booster whereas welding was more successful using a 2.5 gain booster. This can be understood by the increased viscoelastic heat generation calculated with equation 2.7, due to the larger vibrational amplitude and consequently a larger strain amplitude. Like figure 2.3 implies, increasing the gain of the booster results in a larger sonotrode amplitude. In relation to this, it was concluded that a higher booster gain was required to increase the amount of energy in the material, in order to exceed the relatively high T_m of the semi-crystalline PEEK polymer [7]. In essence, this relates to a larger motion of molecules rubbing against each other providing more frictional heat at molecule level [20].

Welding Force

To ensure intimate contact between the two parts to be welded, a force is applied to the parts using an actuator as described in section 2.1.1 [23]. Although the method of force application slightly differs, the tip of the sonotrode exerts the applied force on the parts for spot welding [23], static USW [33] and continuous USW [22]. Having insufficient surface contact (microscopic asperities) between the parts

to be welded is a result of an applied force which is too low [9]. On molecular level, this means that polymer chains have less possibilities to diffuse across the interface, and consequently there are less possibilities to entangle with other polymer chains resulting in a weaker bond [33]. While utilising a low welding force a weak bond can be observed, which is explained by the presence of entrapped air bubbles at the welding interface [40]. Besides, low applied forces can also lead to poor energy transmission resulting in longer required weld cycles [23].

On molecular level, the weld strength is related to inter-diffusion and entanglements of polymer chains. The most ideal case can be described by polymer chains which diffused across the interface and entangled with other polymer chains [22], refer to figure 2.12a. Misalignment of polymer chains, as a result of a large applied welding force is visualized in figure 2.12b. This excessive flow of resin away from the welding interface, because of a high viscosity in combination with a high welding force, is referred to as the squeeze flow of polymer processing [12]. The polymer chains have the tendency to align themselves in the direction of excessive flow in case of an too large applied welding force [12, 33, 40]. The latter is often observed for polymers having a relatively low viscosity [23].

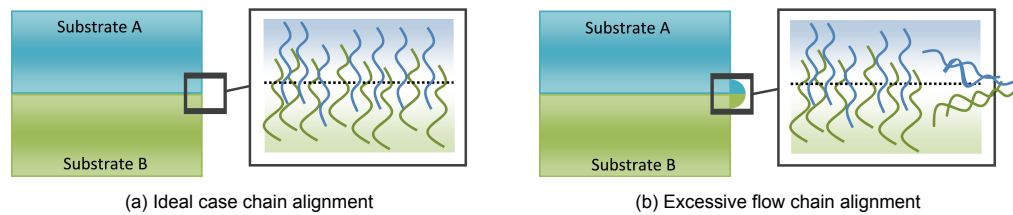


Figure 2.12: Polymer chain alignment across welding interface. Obtained and modified from [22]

In figure 2.13, a relation between the applied welding force and the weld strength is visualized for welding unreinforced polymers [32]. This figure clearly shows that the weld strength of Polyethylene (PE), having a relative high viscosity (table 2.2), is not influenced while increasing the welding force up to 550 kPa. Polymers with a lower viscosity show a small to large drop in the weld strength once the applied force has exceeded the optimum welding force. This is especially the case for PP. The image provided by Rai et al. [37] in combination with table 2.2 experimentally validated the tendency of polymer chains to align themselves in direction of flow when excessive force is applied, especially for polymers having a low viscosity.

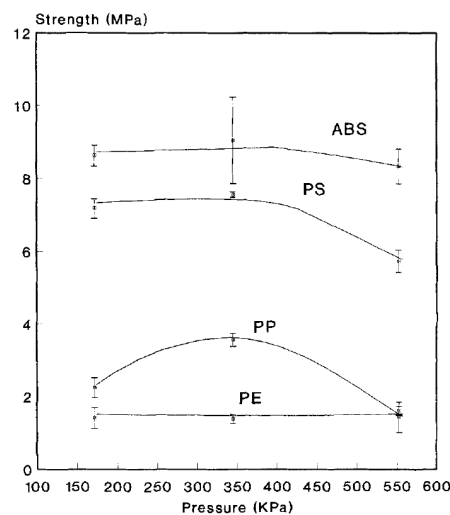


Figure 2.13: Influence of welding force to weld strength for various polymers. Obtained from [32]

To conclude, the most desired welding force is relatively high in the initial phase of the weld cycle for sufficient contact and rather low once the polymer material starts to flow [20]. To elaborate on the latter, polymer chains in this case have time to diffuse and entangle [33].

	PS	PP	ABS	PE
Viscosity [Pa s]	70-100 [77]	100 [55]	140-250 [83]	150-400 [84]

Table 2.2: Viscosity of ABS, PS, PP and PE polymers

Welding Time

The welding time is considered an important parameter for USW [9, 20, 25, 33]. The welding time can indirectly be related to UST by adapting the tape laying speed of the ATL machine. In the earlier discussed work of Tolunay et al. [33], the influence of the welding time was also studied. Without providing the actual temperature profile, Tolunay et al. mentioned that the temperature profile for longer welding times did show besides a temperature increase, no unexpected phenomenon. In other words, the temperature-time graph for 0.1 seconds is a truncated version of the 0.4 seconds graph. For the longer weld cycle, asymptotic behaviour is visible above the T_g resulting in a heating rate of approximately zero. This is related to a rapid decrease of E' to a constant value when T_g is exceeded. The temperature increase while performing longer welding processes is due to having effectively more ultrasonic cycles resulting in more energy input in the material [20]. In contrary, temperature drops at the welding interface were observed by Tolunay et al. [33] after some time in the process. This was explained by the fact that heat from the hotter welding interface zone is conducted to cooler zones resulting in a decrease of interface temperature.

Frequency

As described in the introduction of this report, various frequencies can be utilized in order to be in the frequency range of ultrasonic sound. The maximum power output and corresponding amplitude which can be utilized decrease with increasing operating frequency in the range of 10 kHz to 70 kHz [12, 31]. As already mentioned in section 2.1.1 by using equation 2.1, the resonance length of the three main USW components decrease with increasing frequency. Decreasing the length of the components results in a lower heat capacity what affects the cooling ability [17]. It is mentioned that this results in a limited maximum power setting which can be utilized to prevent overheating of the USW components. Besides, high frequency ultrasonic systems are less prone to damaging the parts and produce less noise compared to low frequency operating systems [31]. As already mentioned in the introduction of this report, a majority of studies dedicated to USW utilize operating frequencies ranging from 15 kHz to 40 kHz instead of frequencies closer to the maximum absorption range, because of the limited power output of the ultrasonic system related to the geometrical and cooling reasons as provided above [31].

Energy Directors

Energy directors are often used for USW of TP composites consisting of unreinforced TP polymer material, often the same type of TP polymer as used in the FRP composite part [5, 12, 21, 23]. Energy directors are introduced to stimulate the welding process because concentrated heating can be realized in the energy director [9], see figure 2.14.

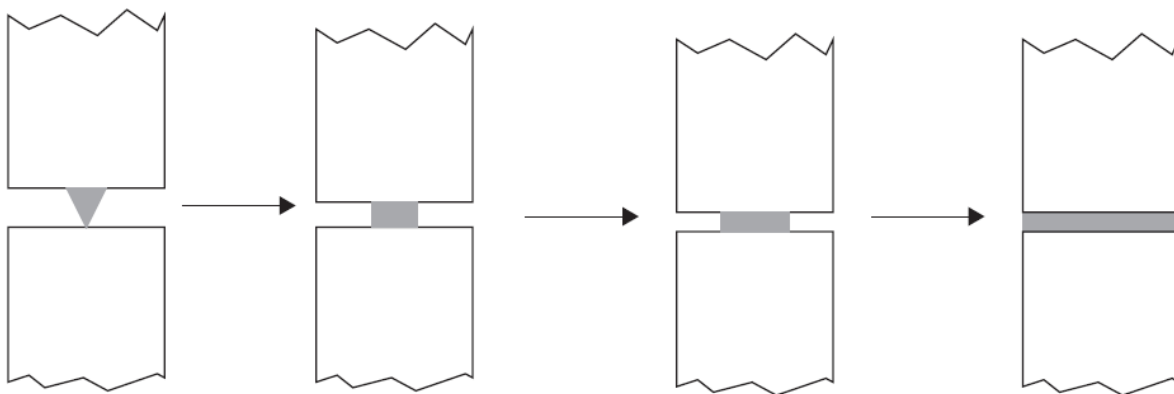


Figure 2.14: Behaviour of energy director throughout the welding process. Obtained from [12]

Heating occurs preferentially at the interface due to the lower stiffness of the energy director, resulting in higher strain levels compared to the stiffer surrounding material [17]. Surface asperities due to the roughness of a material can function as natural energy directors [5, 48]. Sometimes relying on natural energy directors is undesired and artificial energy directors are applied [21]. Artificial energy directors are utilized in various shapes [5, 12, 21, 23] by moulding it to a (composite) part when production is finished [18] or by already considering the energy director in the design and making it an integral part of the joint [32].

It is believed that the most favourable shape of the energy director depends on the part and joint design because for some cases a triangular energy director is favoured [20] whereas for others a semi-circular energy director is optimal [5, 85]. The semi-circular shape is described as favourable because of their good surface wetting capability due to a greater contact area. The triangular energy director in specific cases is optimal because of the better energy conversion towards the tip of the V-shaped energy director. Besides relative thick energy directors, thin neat polymer films can also be used as energy directors [9, 75]. As an example, for welding two 1.92 mm consolidated composite substrates a polymer film of 0.25 mm can be applied at the interface [48].

Besides the advantages of an energy director, a disadvantage mentioned is the possibility of fibre disruption at the surface of the composite part due to the presence of neat polymer material. Additionally, an energy director also gives rise to resin rich areas being less stiff and strong what could influence the mechanical properties of the final product [5, 48]. The application of energy directors in the continuous UST process is questionable since applying a neat polymer layer between each individual UD tape layer would result in adding a significant amount of unreinforced polymer. However, the effect of energy directors can possibly contribute to the knowledge of material weldability. Especially considering that surface asperities [5, 48] and resin rich layers in the composite material [7] can function as energy directors.

2.3. The Quantification of Welding Quality

Methods to determine the tacking quality of the USW process are commonly utilized in order to describe the weldability of a specific TP composite material, and to study the influence of process parameters [86–89]. The bond strength of ultrasonic welded specimens is commonly used to quantitatively describe the quality of the bond [72]. No method nor equipment to determine the bond strength of the tacked TP UD tapes was available at Boikon before the start of this project. Previously, the bond strength of the UST process was evaluated by manually peeling off an individual tape layer. This manual process can be reproduced in a manner that can be quantified by selecting an experimental method capable of performing a peel test [89, 90]. Other experimental methods than peel strength assessment methods have not been considered for this project because the peel-off motion most closely reproduces the earlier performed manual peel tests. The T-peel test, fixed arm peel test, floating roller peel test and the mandrel peel test are frequently used peel strength assessment methods [91], and are described in section 2.3.1 - section 2.3.4 respectively.

2.3.1. T-peel Test

The T-peel test, schematic illustrated in figure 2.15, evaluates the peel strength by means of pulling in a vertical direction while both flexible adherends are clamped [92]. As described, the most ideal peel angle for the T-peel test is 90 degrees (figure 2.17a). However, peel angles of exactly 90 degrees are hard to realize for two reasons [93]. If slight stiffness variations are present in the upper and lower adherend, the unpeeled section of the sample will not remain straight. The unpeeled section of the sample will bend upwards when the stiffer part is located at the bottom part of the bonded sample and visa versa, as illustrated in figure 2.17b and figure 2.17c. In contrast to testing adhesives, samples having a relatively high stiffness can never result in a peel angle of 90 degrees, as illustrated in figure 2.17d, even when the stiffness of both adherends is exactly the same [92, 94].

2.3.2. Fixed-arm Peel Test

The fixed-arm peel test, schematic illustrated in figure 2.16, only differs from the T-peel test in two aspects [94]. In contrast to the (ideal) 90 degree peel angle, the fixed-arm peel test can be conducted with different peel angles θ by selecting different base fixtures. Note that the base fixture is positioned

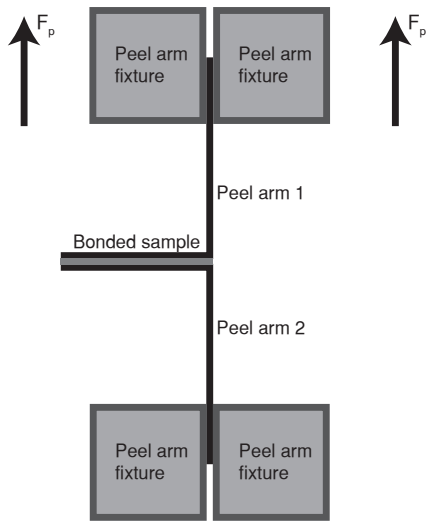


Figure 2.15: Schematic illustration of the T-peel test

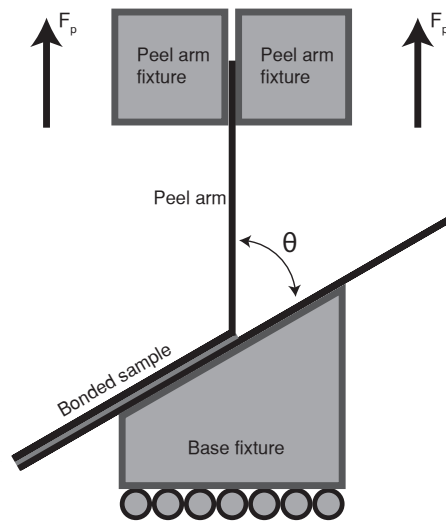


Figure 2.16: Schematic illustration of the fixed-arm peel test

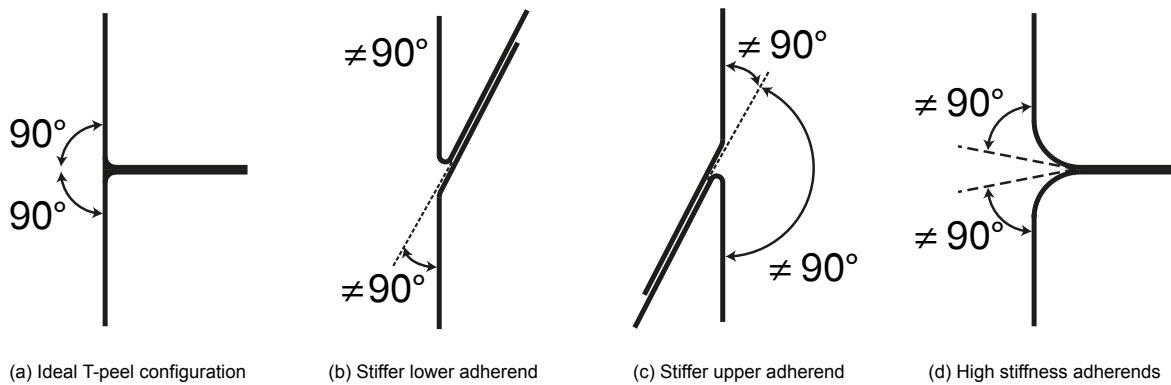


Figure 2.17: Various possible T-peel test situations

on a horizontal displacement unit to conform to the vertical motion of the test bench. Additionally, the fixed-arm peel test requires that one of the substrates is positioned at the rigid base fixture. The latter is also the case for the consecutive roller assisted peel tests [91, 94, 95]. The configurations sketched in figure 2.17b and figure 2.17c are not a concern for the fixed-arm peel test since one of the adherends is applied to the rigid fixture. Similar to the T-peel test (figure 2.17d), obtaining the exact same peel angle as the base fixture angle is rather impossible when assessing the peel strength of bonded samples with a relatively high stiffness.

2.3.3. Floating Roller Peel Test

The floating roller peel test, schematically depicted in figure 2.18, does require a rigid adherend in combination with a flexible adherend. The peeling motion is initiated by a vertical displacement, indicated by the arrow. The main difference between the floating roller peel test and the two previous described tests is that the peel behaviour is conform a roller with a fixed radius [94, 95]. If the rollers are selected properly, a constant peel angle can be realized because the flexible adherend follows the curvature of the roller. To ensure conformity of the flexible adherend, the roller radius is generally determined based on two criteria [91]. In case an unbonded sample cannot follow the curvature of the roller, the selected roller radius is too small [88]. This means that when the flexible tape should follow the curvature of the roller, the maximum bending strain of the sample is exceeded resulting in failure of the sample prior to peel-off. In case of the UD tapes, this would result in fibre failure. Besides unbonded samples, bonded samples should also have conformity to the roller [91, 94]. As figure 2.18 illustrates, for conformity of bonded samples $R_0 \geq R_1$ must hold [94]. If conformity is not achieved, a roller with a smaller radius

should be selected. The centres of roller number 2 and 3 are not positioned at the same vertical position to ensure that the rigid adherend is positioned in the fixture such that the flexible adhered is in contact with roller number 2. Based on a couple of manual peel-off trials trying to prove the concept, it was discovered that the bond strength of the continuous tack (two sonotrode positions) is relatively low. The bond between the flexible adherend and the rigid adherend ensures contact to roller number 2 and 3. In a non-equilibrium position of the rigid adherend, the low bond strength easily results tilting. In other words, contact is lost between the rigid adherend and roller number 2 or 3, depending on the position of the rigid adherend. Reducing the length of the rigid sheet overlap would resolve this problem which subsequently results in a shorter test stroke.

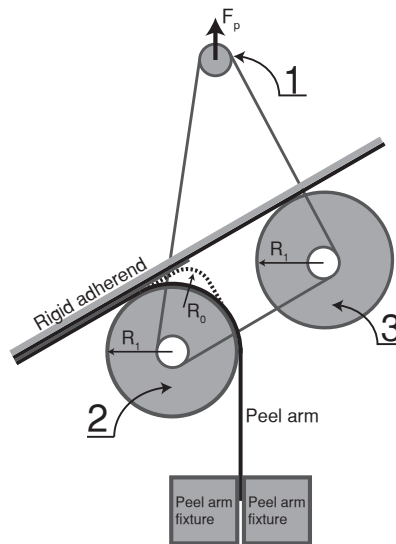


Figure 2.18: Schematic illustration of the floating roller peel test. Constructed using [94]

2.3.4. Mandrel Peel Test

The second roller assisted peel strength experimental method is called the Mandrel Peel (MP) test, depicted in figure 2.19. Similar to the floating roller peel test, this test also requires one flexible adherend and one rigid adherend. For this test the rigid adherend slides horizontally with a velocity equivalent to the peel rate. The alignment force F_a is used to ensure conformity of the flexible adherend to the mandrel [87] which can be realized by using dead weights or a pneumatic cylinder [88, 90]. Similar to the floating roller peel test, the MP test should also comply with $R_0 \geq R_1$ in order to meet conformity [91]. Besides the ability to vary the mandrel radius, the MP test can also use F_a to ensure conformity [88], as depicted in figure 2.20.

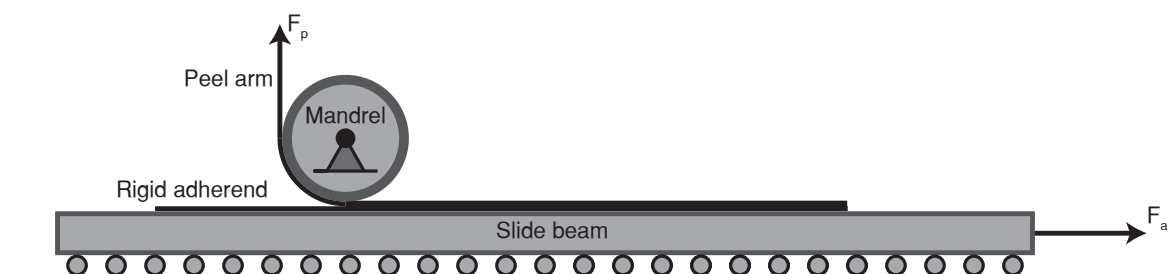


Figure 2.19: Schematic illustration of the mandrel peel test. Constructed using [87]

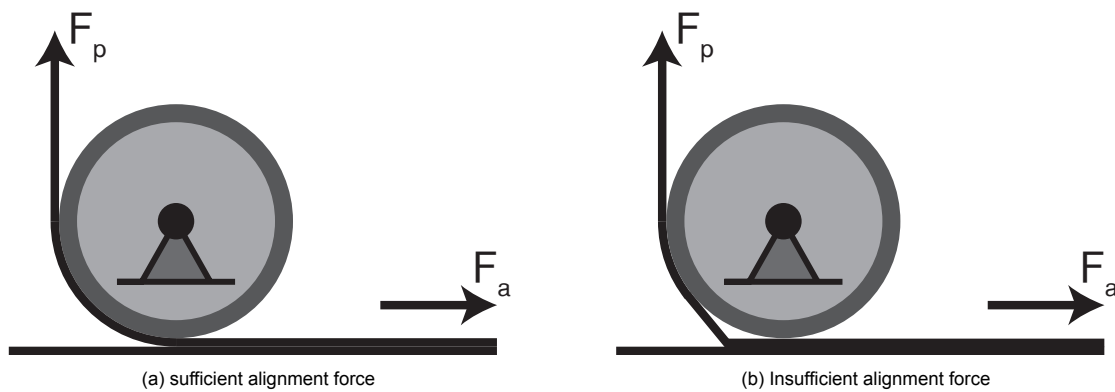


Figure 2.20: Influence of alignment force for conformity of the mandrel peel test. Constructed using [88]

2.4. Statistical Methods for Design of Experiments

Section 2.4.1 describes the basics of DOE and motivates why RSM is selected as type of DOE for this project. Furthermore, section 2.4.2 provides the details of the RSM model.

2.4.1. Design of Experiment Motivation

The DOE approach is a commonly utilized method to study the influence of parameters to the output for an improved understanding of the process, which could eventually result in an optimized process [96, 97]. Various types of DOE are available, each having their own advantages and disadvantages [98, 99]. Nevertheless, each DOE method originates from the following equation

$$Data = Model + Residual \quad (2.9)$$

with a generic goal to minimize the residual term [98, 100, 101]. In terms of DOE, predictors (input parameters) and responses (measured results) are common terminology [98].

In (composite) process optimization, the full factorial design [97], the fractional factorial design, the Taguchi method [102, 103] and the Response Surface method [72] have been used for designing and analysing experiments. The remainder of this section briefly describes the motivation of the selected DOE for this project. More details about the selected RSM are provided in section 2.4.2.

Full Factorial DOE

The full factorial design consists of L^k experimental runs where L and k are the amount of levels studied per parameter and the number of parameters respectively [98]. The full factorial method requires a relatively large amount of experimental runs, resulting in a labour intensive method [98, 99, 101]. Nevertheless, this type of DOE is perfectly capable of providing the interactions between predictors and the response(s).

Fractional Factorial DOE

In case a less labour intensive DOE is desired, the fractional factorial design can be selected [98]. The main difference between the full factorial design and the fractional factorial design is the reduced amount of levels for each predictor. Two predictor levels are often selected when this approach is used [72, 101, 104]. The more time efficient experimental process is associated with a reduction of model accuracy because only two predictor levels are considered [98]. The latter means that only linear interactions can be predicted when this DOE is utilized.

Taguchi DOE

The Taguchi method requires less experimental runs compared to the fractional factorial DOE. and determines based on the signal-to-noise ratio which predictor values are optimal for a desired response. This approach has been utilized many times in the past in the field of ultrasonic welding [20, 21, 102]. In these studies the goal was to find the most optimal welding settings for realising a strong bonded part. Although the Taguchi method is powerful in optimization of parameters, it cannot provide interactions between parameters [72, 98, 99].

Response Surface DOE

The RSM consists of a two level factorial design with the addition of axial and centre points [72, 99, 101]. In contrast to the fractional factorial method, RSM is able to include curvature in the model due to the added axial points. The RSM provides a response surface in three-dimensional space [105]. The direction of steepest ascent/descent indicates the direction with highest potential for process optimisation [101]. Although this response surface is not extended outside the range of the predictor levels, it can indicate the direction with highest potential for the desired response.

DOE Motivation

The DOE selected for this project is RSM because interactions between (main)parameters and optimisation possibilities are of interest. This signifies why the Taguchi method is less feasible for this specific study, as it does not provide information on parameter interactions. Additionally, little information about the relation between the UST parameters (predictors) and the bond strength (response) meaning that linearity cannot be ensured. The latter motivates why the fractional factorial DOE method is not selected. RSM is selected above the full factorial method because it is a more time efficient approach with similar capabilities in predicting interactions and possibilities for process optimisation.

2.4.2. Response Surface Methodology

The most basic RSM model is based on a linear model where the response can be described with

$$y = \beta_0 + \sum_{j=1}^k \beta_j x_j + \epsilon \quad (2.10)$$

where the β_0 , β_j for $j = 1, 2, \dots$ and ϵ are the constant term representing the plane intercept, the coefficients of the corresponding predictors and the model error respectively [98–100]. When the nature of the response is unknown, meaning that perfect linear interactions cannot be ensured a higher order RSM should be used. The following equation:

$$y = \beta_0 + \sum_{i=1}^k \beta_i x_i + \sum_{i=1}^k \beta_{ii} x_i^2 + \sum_{1 \leq j \leq i}^k \beta_{ij} x_i x_j + \epsilon \quad (2.11)$$

which can predict curvature in the response surface, contains first order effects (first summation), second order effects (second summation) and interactions between predictors (third summation) [106].

There are various types of RSM [99, 105] from which the second order Central Composite Design (CCD) is selected for this project as it has proven its effectiveness in other studies related to welding applications [72, 107, 108].

Mathematical Model

The CCD can be used up to 10 predictors and can include multiple responses [99, 105]. The model of a three predictor CCD with each three levels is presented in figure 2.21a. This model requires N experimental runs with

$$N = 2^k + 2k + C_0 \quad (2.12)$$

where 2^k , $2k$ and C_0 correspond to the two-level factorial design points, the axial points and the number of centre points.

For each predictor, the points at the cube edges (cube points) should be selected based on process experience and should comply with the region of interest [101]. With the definition of the cube points (X_{i_L} and X_{i_R} for $i = 1, 2, \dots$) the axial points (X_{i_A} for $i = 1, 2, \dots$) can be calculated with

$$X_{i_A} = \frac{X_{i_L} + X_{i_R}}{2} \pm \alpha \cdot \frac{X_{i_L} - X_{i_R}}{2} \quad (2.13)$$

where α specifies the distance from the axial points to the centre point [101]. This property can be calculated by

$$\alpha = 2^{(k/4)} \quad (2.14)$$

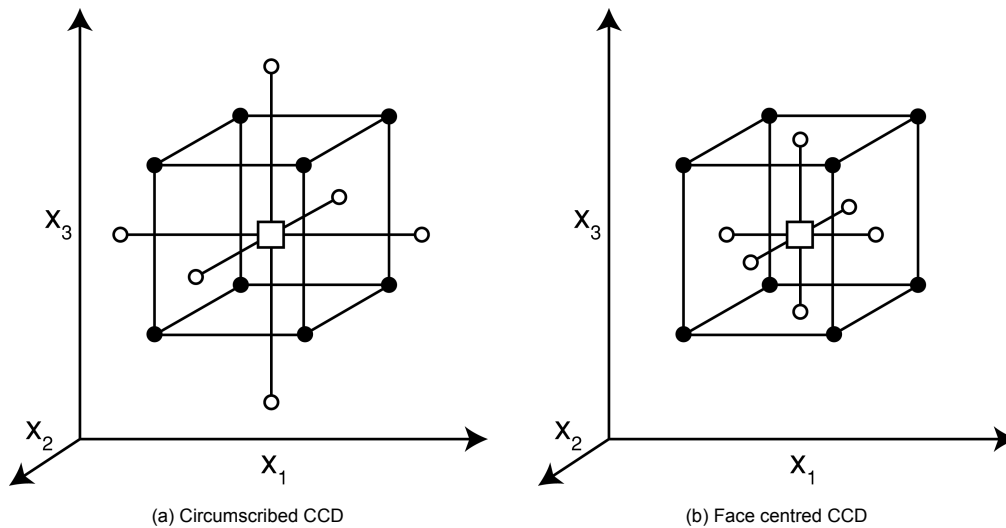


Figure 2.21: Three predictor, three level (a) Circumscribed and (b) Face centred central composite designs (○ = axial points, ● = factorial points and □ = centre point). Constructed using [106].

for k predictors [106]. The model depicted in figure 2.21b corresponds to $\alpha = 1$ which is called a face-centred CCD as the axial points are positioned on the faces of the cube [99].

An example of a three predictor, one response face-centred CCD design containing three centre points is created using Minitab and provided in table 2.3. With use of the standard order (StdOrder) column in combination with the point type (PtType) column can be used to understand how the design is constructed [105]. Presented in the table and according to equation 2.12, this model contains eight cube points (PtType 1), six axial points (PtType -1) and three centre points (PtType 0). Nevertheless, the standard order is not used for the statistical analysis but purely for visual representation. Experimental runs are generally performed based on a random order to uniformly distribute unobserved systematic changes, which are not related to the response over the complete set of experiments [105]. Replicates grouped in blocks are common practice in a DOE [106, 108], such that the experimental error of the model can be minimized [98]. Additionally, replications increase the accuracy of prediction of predictor interactions. Without replications conclusions can be based on the experimental error instead of the actual interaction(s) [98, 105]. Considering η_s replicates, the total number of axial points equals $2k\eta_s$ [109]. The design presented in table 2.3 does not contain replicates, thus only one block is required. The last three columns of table 2.3 show the levels of the three predictors (Pred1 - Pred3) in coded variables, of which the use becomes necessary when two or more independent variables are included in the model [105]. Coded units are effective in ensuring that regression coefficients can be compared between models, and are scaled from -1 to 1 as depicted in figure 2.22 [101, 110].

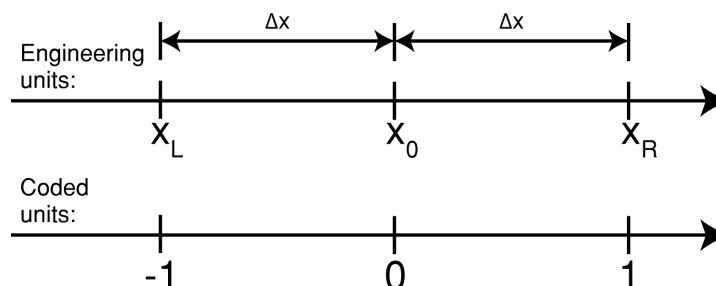


Figure 2.22: Transformation of predictor levels from engineering units to coded units. Obtained and modified from [105].

StdOrder	RunOrder	PtType	Block	Pred1	Pred2	Pred3
1	15	1	1	-1	-1	-1
2	1	1	1	1	-1	-1
3	9	1	1	-1	1	-1
4	8	1	1	1	1	-1
5	6	1	1	-1	-1	1
6	11	1	1	1	-1	1
7	2	1	1	-1	1	1
8	16	1	1	1	1	1
9	10	-1	1	-1	0	0
10	14	-1	1	1	0	0
11	4	-1	1	0	-1	0
12	7	-1	1	0	1	0
13	5	-1	1	0	0	-1
14	12	-1	1	0	0	1
15	17	0	1	0	0	0
16	3	0	1	0	0	0
17	13	0	1	0	0	0

Table 2.3: Face centred central composite design example

Assumptions

Prior to using the CCD results, it is essential to check that none of the assumptions of the classical statistical framework are violated [72, 99, 100, 109]. First of all, it should be ensured that the responses are normally distributed [105, 109]. A normal distribution can be used to characterize data when the majority of the data is centred around the mean value [100]. A histogram of the residuals and a normal probability plot can be generated using the statistical software package Minitab and should be used to determine if the normality assumption holds for the current dataset [105]. Figure 2.23 shows an example of a non-normal distribution plot. This can be concluded because of the misalignment of responses with respect to the linear red line. For perfect normality all the data points must be positioned on the red line. Violation of the normality assumption may result in inaccurate results and consequently misinterpretation of the process [111]. For this reason data transformation methods are often introduced to achieve normality [109], which are mentioned in the next paragraph.

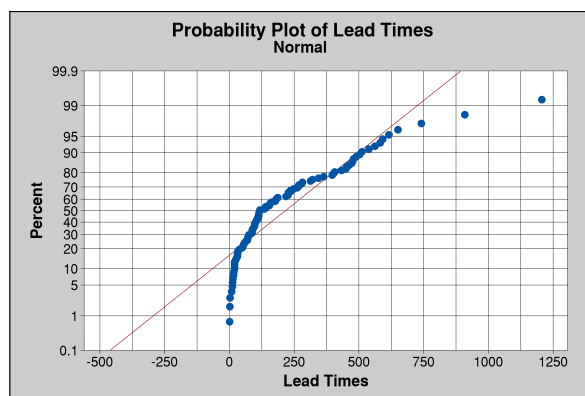


Figure 2.23: Non-normality response distribution plot. Obtained from [72]

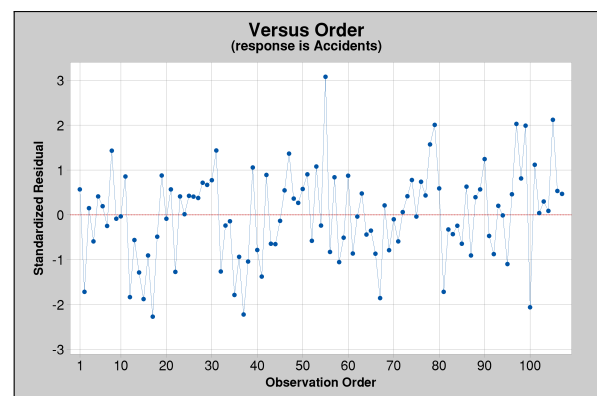


Figure 2.24: Example plot of residuals versus observation order

The next assumption is related to the independence of the residuals [100, 105]. A residual plot with respect to the observation order can be used to test for this assumption. An example of such plot is provided in figure 2.24 which shows a random behaviour of the residuals. If no clear pattern can be observed from such graph it can be stated that the residual terms are uncorrelated and the assumption is obeyed [105].

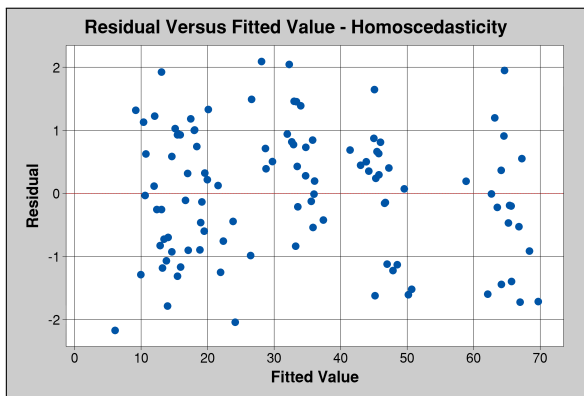


Figure 2.25: Residual vs. fitted value plot - homoscedasticity

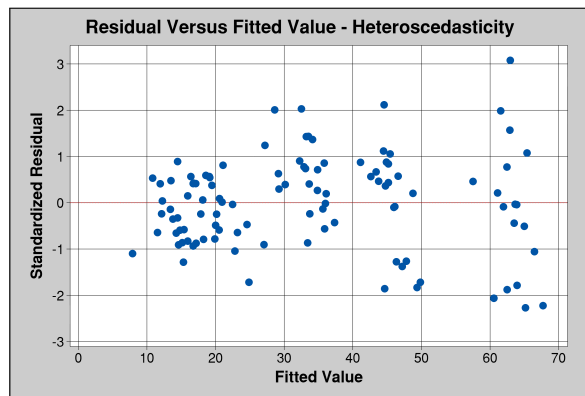


Figure 2.26: Residual vs. fitted value plot - heteroscedasticity

Finally, for the statistical regression method to be accurate and reliable the data should be homoscedastic [105, 109]. This assumption implies that the variance in responses at different predictor levels should be approximately equal. A residual versus fitted value plot can be used to visually determine if the data is homoscedastic. In case of (approximately) equal variances the residual versus fitted plot would look similar to the plot provided in figure 2.25. An example with unequal variances is shown in figure 2.26, which is called heteroscedastic. Heteroscedasticity often originates from the use of measuring devices as the measuring accuracy is generally a percentage of the measured value [101]. This means that the residuals are likely to become larger for high value measurements compared to low value measurements.

Besides the aforementioned visual approach, Levene's test is a commonly applied technique to test for equal variances [100, 101, 112]. The null hypothesis of Levene's test states that there exists equality in variances, meaning that homoscedasticity is observed. This null hypothesis is rejected at a significance of $p \leq 0.05$ meaning that the variances are unequal, thus the data is heteroscedastic. If the null hypothesis is accepted (i.e. $p > 0.05$) it can be stated that the variances are not significantly different (homoscedasticity) [100]. When heteroscedasticity is observed, using either the residual versus fitted value plot or Levene's test a data transformation is required to prevent violation of this specific assumption.

Data transformations

In case of violation of the normality and/or homoscedasticity assumption it is common to apply a data transformation to all response values prior to analysis of the results [72, 99, 109]. If this technique is applied correctly the responses become stabilized such that normality and/or homoscedasticity can be guaranteed. In mathematical terms the transformation can be described with

$$y_i^* = f(y_i) \quad (2.15)$$

where y_i^* is the transformed value of the response value y_i by using the transformation function f . The square root, the logarithm and the reciprocal of the response value are common transformation functions [72, 109]. Generally the behaviour of the spread in data determines which transformation function is best to be used [101, 109]. For example, a logarithmic transformation suits best for a dataset showing standard deviations proportional to the measurement means [105].

Besides the fact that data transformations are an useful and effective method to ensure normality, it also introduces some points of attention when the RSM results are studied. The results of the non-transformed dataset should not be ignored, this to ensure that transformed dataset does not provide completely different results [109]. Additionally, if a regression equation is used to statistically determine the response based on certain predictor values it should be noted that the response requires an transformation to return to the original scale [105].

Evaluation of Results

After all the assumptions are obeyed, the RSM results can be studied. This section provides an overview how the results provided by Minitab should be interpreted. First of all, the statistical sig-

Source	DF	Adj SS	Adj MS	F-value	P-value
Model	C-1
Blocks	B-1
Linear terms	P
Squared terms	P
Interaction terms	P
Error	N-C
Lack-of-fit	M-C
Pure error	N-M
Total	N-1

Table 2.4: Minitab standard format Analysis of Variance result table, N = total number of observations, B = number of blocks, P = number of predictors, C = number of regression coefficients, M = number of unique test combinations x number of blocks. DF Equations obtained from [99, 105, 106, 110, 113]

nificance of the sources included in the model must be analysed, this is done based on the Analysis of Variance (ANOVA) part of the RSM. Thereafter, the importance of a source with respect to the response can be determined. Additionally a model summary is provided which describes the overall fit of the model. Finally, RSM provides knowledge about process optimisation possibilities based on the surface response plots [72, 101].

Table 2.4 provides a standard format ANOVA result table of a second order RSM model [105]. The first column describes various sources, the experimental data is represented by a combination of the model and the error [105]. Beside blocks, the model is described by linear (predictor1) and quadratic (predictor1·predictor1) terms combined with interactions of the linear terms (predictor1·predictor2).

The lack-of-fit in combination with the pure error establish the total error of the model [105]. The lack of fit, which can only be determined if replicates are included in the DOE, quantifies how well the model fits the actual data [99, 105, 106]. If $p \leq \alpha$ the model does not accurately represent the experimental data, consequently $p > \alpha$ means that it cannot be concluded that the statistical model does not fit the experimental data [105, 110]. The pure error generally describes the most variation in residuals, due to fluctuations in measurements and is estimated by variations observed in the centre runs of the CCD model [106].

The second column provides the Degree(s) of Freedom (DF) which represents the amount of independent and unbiased comparisons which can be made for a specific quantity [98, 100, 101]. The total DF can be split in two categories, the model and the error. Both, linear and squared terms do have a DF of unity, considering that the predictors are continuous and not categorical [105, 110, 114]. Additionally, without categorical predictors each 2-way interaction does have a DF of one. Degrees of freedom must be available to estimate the error ($N - C$) [105]. For high order models (high value of C) large number of experimental runs must be performed, if necessary with additional replicates.

Column three provides the Adjusted Sum of Squares (Adj. SS). To start, the Sum of Squares (SS) describes the total error between the predicted model and the original data and is calculated with

$$SS = \sum(x_i - \bar{x})^2 \quad (2.16)$$

where x_i and \bar{x} are the i^{th} response value and the mean of all observed responses respectively [100]. The residuals are squared to prevent that the summation is influenced by a combination of positive and negative residuals [105]. This SS describes the accuracy of applying the mean value as statistical model and is often referred to as Total Sum of Squares (SS_T), calculated with

$$SS_T = SS_M + SS_R \quad (2.17)$$

containing Model Sum of Squares (SS_M) and Residual Sum of Squares (SS_R). The SS_M describes the increase in accuracy when the best fitted model is used, in comparison with mean value model which is considered as the most basic model available [100]. Even with the use of the best fit model, residuals between the actual and predicted data are present which are characterized by SS_R . Equation 2.17 can

also be described as

$$Adj. SS_T = Adj. SS_M + Adj. SS_R \tag{2.18}$$

quantifying the total variation in data [72, 106]. The variation in response contributed by a term is denoted as Adjusted Model Sum of Squares ($Adj. SS_M$), which is determined by the variation between the full model and a model neglecting that specific term [100]. For an example with three predictors (X_1, X_2 & X_3) this is mathematically described as

$$Adj. SS_M(X_1|X_2, X_3) = |SS_M(X_1, X_2, X_3) - SS_M(X_2, X_3)| \tag{2.19}$$

where $SS_M(X_1|X_2, X_3)$ is called the difference in SS for predictor X_1 [114]. Usually the SS or $Adj. SS$ values are not directly used for interpretation of the results but are used to calculate the contributions, F-values and p-values [101].

Dividing the $Adj. SS$ by the DF of results in the Adjusted Mean of Squares ($Adj. MS$), provided in the fourth column of table 2.4 which explains the amount of variation [100, 105]. The $Adj. MS$ is used to calculate the F-value (fifth column) of a source term by

$$F = \frac{Adj.MS}{Adj.MS_R} \tag{2.20}$$

with $Adj.MS_R$ as the mean square of the residuals [100]. The calculated F-value is used to determine the probability of evidence to accept or reject the null hypothesis, defined as no interaction between the source term and the response [72]. In other words, p-values can be used to determine influential factors with respect to the response [99]. The level of significance for a test is often defined as $\alpha \geq 0.05$, meaning that a 5% chance exists that it is falsely concluded that a relationship between predictor and response exists [72, 101, 115, 116].

An example F-value distribution plot for 1 DF in de nominator and 39 DF in de denominator is provided in figure 2.27. The DF correspond to the DF of the terms in equation 2.20. For this case with a significance level of $\alpha = 0.05$ the critical value F-value is defined as 4.091. F-values larger than the critical F-value provide statistical significance, resulting in $p < \alpha$. Meaning that the null hypothesis (no interaction between predictor and response) is rejected, vice versa for F-values smaller than the critical F-value [110]. Additionally, the greater the F-value (the smaller the probability value), the more evidence exists against the null hypothesis [99].

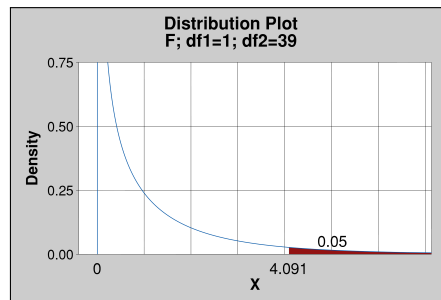


Figure 2.27: F-value (1,39) distribution plot including critical F-value

The contribution in percentage of a source with respect to the response can be provided by Minitab and is based on

$$Contribution = \frac{(Adj. SS)_{source}}{(Adj. SS)_{total}} \tag{2.21}$$

describing the amount of variation observed by that source with respect to total observed variation [101, 105, 117]. Note that the numerator and denominator of equation 2.21 can be extracted from the second data column of table 2.4.

The model summary provided by Minitab consists of four parameters, the standard deviation, R-squared, R-squared(adjusted) and R-squared(predicted) [110]. The standard deviation is a measure of how close the actual data is separated from the response surface and does have the same unit as the

response of the model [99]. Therefore, a low standard deviation is favoured. The equation for the standard deviation equals

$$S = \sqrt{\frac{1}{N} \sum_{i=1}^N (x_i - \mu)^2} \quad (2.22)$$

where N , x_i and μ are the total number of observations, the i^{th} observation and the overall mean response [105]. R-squared (R-sq), calculated with

$$R\text{-sq} = \frac{Adj.SS_M}{Adj.SS_T} \cdot 100\% \quad (2.23)$$

expresses the amount of variation in the response which can be explained by the model [100]. In other words, it is a measure for goodness of fit of the model. Models with mean response values of different magnitudes can be compared more accurately using R-squared instead of the standard deviation, due to the fact that S is correlated to magnitude of the mean of the overall response. R-squared(adjusted) is adjusted for the amount of predictors and the total amount of observations, this is a useful property when comparing the accuracy of models containing different amount of predictors and/or observations [110]. This is not the case for the current project, this property is therefore not considered. The last statistical property of the model summary, R-squared(predicted), describes the ability of the model to predict the response value for predictor combinations beyond the obtained data. The R-squared is determined by systematically removing an observation from the model, and comparing actual value with the predicted value by the model [101, 105].

As mentioned before, response surfaces and contour plots are used for process optimisation and can be realized based on regression equation of the model. Figure 2.28 and figure 2.29 provide an example response surface and contour plot respectively [110]. Besides the 3D and 2D representation, no differences exist between both graphs. Hold values are required for models containing more than two predictors because this type of representation can besides the response only include two predictors. The hold values in terms of the regression equation are simply predictors which are fixed at a certain value while the other predictors are varied to obtain the corresponding predicted peel strength. Based on the aforementioned graphs the predictor settings can be determined such that optimum response is achieved [99]. Finding a new region to operate in is sometimes the goal of a study rather than finding the point of optimum response, in this case the direction of steepest descent/ascent shows the direction with the highest potential for process optimisation [99, 109].

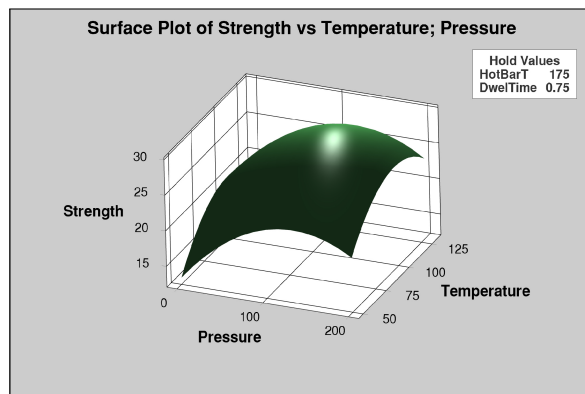


Figure 2.28: Example response surface plot. Data obtained from [110]

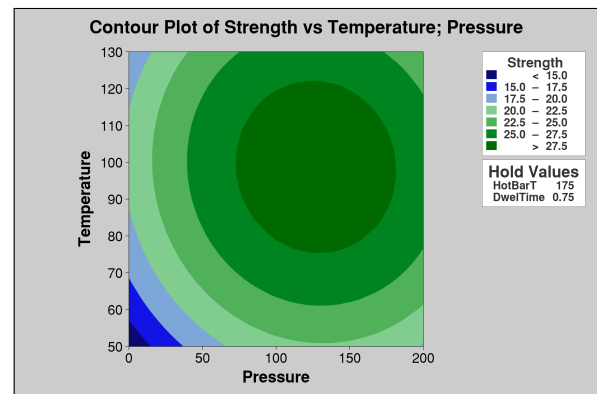


Figure 2.29: Example contour plot. Data obtained from [110]

3

Microstructural Characterization of Unidirectional Tapes

Section 3.1 describes the methodology used to characterize the microstructures of Unidirectional (UD) tapes. Section 3.2 describes the microscopic activities, including how the samples are prepared. The micrographs obtained are analysed and are eventually used as input data for post-processing of the data. The design of the analytical model is presented in section 3.3. The results are provided and discussed in section 3.4. Section 3.5 provides conclusions to the method of analysing and the results presented.

3.1. Methodology of Experiment

Differences in tacking quality are observed in the past between (apparently) similar and various Carbon Fibre (CF) UD tapes utilized at Boikon. For example, it occurred in the past that material A could not be tacked while material B showed a perfect bond between both tapes utilising the same Ultrasonic Tacking (UST) tacking parameters. Therefore, it is of interest to acquire a thorough understanding of the input UD tape. The relevant UD tapes of this project can be ordered by the ability to tack. Starting with the most challenging tape the order is: CF-Polyetheretherketone (PEEK) from Teijin, CF-Polyetherketoneketone (PEKK) from Toray and CF-PEKK from Solvay. While tacking Thermoplastic (TP) tapes, the TP polymer resin establishes the bond [8, 31]. Considering that artificial resin layers (Energy Director (ED)) are added to composite parts to enhance the weldability [74, 85], the microstructure of the tapes utilized at Boikon are studied with microscopic equipment and quantified using a Voronoi tessellation algorithm. The goal of this experiment is to quantify the physical differences of the CF-PEKK and CF-PEEK UD tapes, and eventually relate this to the tacking challenges encountered. Various quality criteria are introduced to evaluate TP tapes such as the accuracy of fibre volume content, constancy of fibre volume content, tape thickness and the homogeneity of fibre-resin distribution [118]. The latter quality criteria is considered as the main driver for this chapter.

In order to quantify the microstructures, detailed cross-sectional micrographs of the UD tapes are required. The micrographs are used to extract the fibre locations in relation to the TP resin, either PEKK or PEEK. The position of each fibre in the cross-sectional plane is described using a two-dimensional Cartesian coordinate system. The fibre locations are used as input for a Voronoi pattern. For a two-dimensional image this method, also referred to as Dirichlet Tessellation, divides a plane in several areas called Voronoi cells or Voronoi polygons [119]. The construction principle of a Voronoi pattern can be described according to images created with the online interactive tool provided by Khan Academy ¹. Figure 3.1 depicts the construction of a Voronoi pattern in four steps. Circles are drawn concentric at each input point with increasing diameter up to the point of intersection with another circle, see figure 3.1b. A line tangential to the circle is constructed upon intersection, up to intersection of another tangential line. These tangential lines are the edges of the Voronoi cells. The Voronoi pattern is final-

¹www.khanacademy.org

ized once the complete plane is filled with Voronoi cells, meaning that all edges have intersected with others, depicted in figure 3.1d.

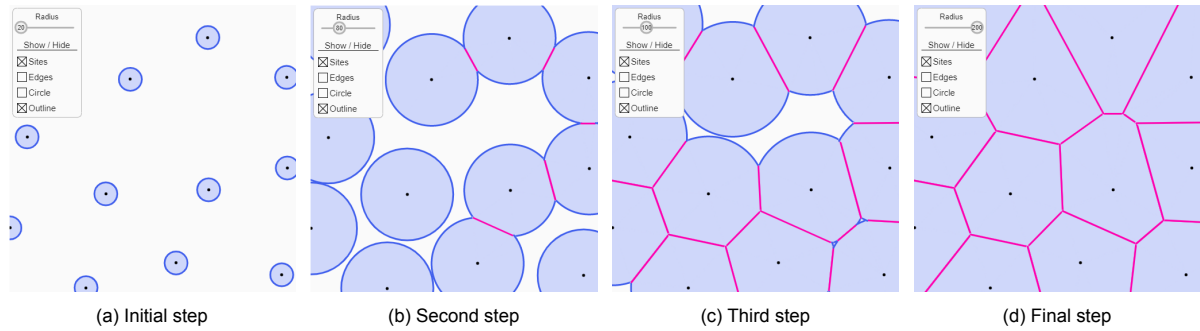


Figure 3.1: Voronoi pattern visualized using four subsequent steps

Depicted in figure 3.1d, each individual Voronoi cell corresponds to a single input point. A remarkable property of a Voronoi cell is that any random selected point in that cell is closest to that specific corresponding input point [120]. This property is used to quantify the amount of resin that belongs to a specific individual fibre. Based on a pre-defined boundary, the area of the Voronoi cells are calculated. A local fibre-resin ratio can be calculated with dividing the fibre cross-sectional area by the area of the corresponding Voronoi cell. This local fibre-resin value is used to quantify the fibre-resin architecture using two different analysis method. The first method divides the tape in several segments in thickness direction, meaning that each segment is described with an average fibre-resin ratio. A graph realized with the average fibre-resin data of each segment is used to present an overall through thickness fibre-resin distribution of an UD tape. Earlier mentioned is the addition of a resin rich layer at the interface of both both parts to bond, a so called ED, to enhance bonding capabilities. To determine to which extend an UD tape features a resin rich layer at the top or bottom surface the Voronoi cells intersecting with the tape edges are of relevance. Extracting the local fibre-resin ratios of the boundary Voronoi cells is useful to describe whether an UD tape is more resin rich or fibre rich at the top and bottom surfaces. The two analysis methods described above are performed on multiple micrographs after which the results are combined in order to describe the fibre-resin architecture of the three UD tapes.

3.2. Sample Preparation and Micrograph Analysis

The Keyence VK-X1000 3D laser scanning confocal microscope, available at the Aerospace faculty of the Delft University of Technology, was used to obtain high quality cross-section micrographs of the UD tapes. This microscope was selected because of its automatic stitching function. This function can generate one large image from multiple smaller images, meaning that a high magnification image over a large section is feasible. To analyse the UD tapes with this microscope, the UD tape samples must be embedded. Embedding of the samples enable proper fixation and positioning of the samples with respect to the lens of the microscope.

	1.1	1.2	2.1	2.2	3.1	3.2	Mean
CF-PEEK Teijin	0.22	0.23	0.22	0.23	0.22	0.23	0.225
CF-PEKK Solvay	0.21	0.20	0.19	0.20	0.19	0.19	0.197
CF-PEKK Toray	0.15	0.16	0.15	0.14	0.15	0.15	0.150

Table 3.1: CF-PEKK and CF-PEEK UD tape microscopy sample thickness measurements in mm

Table 3.1 presents the thickness of the 15 mm (|| to fibre) x 10 mm (\perp to fibre) samples, measured at two random locations of each sample. The first samples produced for the microscopy experiments were embedded with a mixture of Technovit 4071 resin and Technovit 4071 harder. However, the fast curing process introduced air bubbles in the embedded sample which considerably reduced the micrograph quality. For this reason Struers EpoFix slow cure, transparent embedding resin was selected



Figure 3.2: Photograph of UD samples in sample holder before embedding

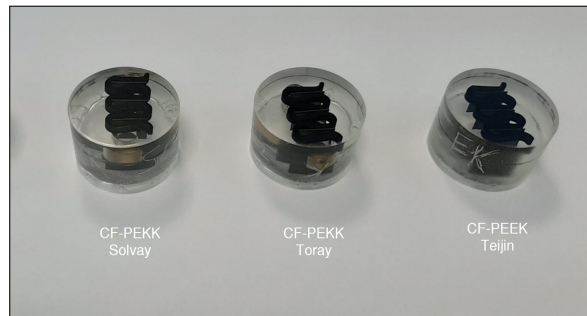


Figure 3.3: Photograph of embedded and prepared UD tape samples for microscopy

for preparing the actual samples. Figure 3.2 shows the samples placed in the sample holder and the cups in which the samples are embedded. After the mixture of hardener and resin was poured in the sample cup holder, entrapped air was removed from the embedding resin with the CitoVac vacuum impregnation unit. After release of the vacuum, the embedding resin required a 12 hours cure. The samples were sanded and polished using the Struers Tegramin equipment for high quality specimen preparation. Proper grinding and polishing is of importance, otherwise the fibres are not exposed to the upper surface of the embedded samples making it impossible to capture high quality images of the tape cross-section. Figure 3.3 presents the final embedded samples used for the microscopic activities. Micrographs were captured using the Keyence microscope with 50X magnification and applying coaxial lighting. This magnification was the highest available and therefore resulted in the most detailed cross-section images possible. Due to the stitching function the captured area was not limited as a result of the high magnification. A consequence of using such high magnification is the duration to capture the full width (10 mm) of the sample, capturing one image took approximately one hour. Three images with approximate size of 17.000 x 700 pixels were captured, large enough to capture the full sample cross-section. The captured images were saved with a standard image file extension using the Keyence MultiFileAnalyzer software. A small captured section of each UD tape is presented in figure 3.4. Remarkable characteristics observed in the tapes are presented in detail in figure 3.5. The earlier mentioned variation in thickness between the three UD tapes analysed is also visible in these images. In previous research, Schledjewski and Schlarb [118] addresses common material defects like matrix accumulation and insufficient micro impregnation of the TP resin which are also observed in the micrographs of the UD tapes.

3.3. Design of Analytical Material Analysis Model

The analytical model to analyse the PEEK and PEKK UD tapes consist of two parts, namely fibre location extraction from the micrographs and post-processing of the data to eventually determine and present the local fibre volume content of each Voronoi cell. The method of fibre coordinate extraction is elaborated on in section 3.3.1, post-processing of the data is described in section 3.3.2.

3.3.1. Fibre Coordinates Extraction

To accurately determine and extract the fibre locations from the micrographs various methods and software have been considered. According to literature, the circular Hough transformation is a common applied technique in scientific image analysis to identify circular objects based on shape detection of lines [121]. This algorithm provides the diameter of each circular shape detected and is capable of detecting near circular ellipsoids [120]. However, the Hough algorithm becomes calculation intensive for large images due to numerical processing of the parameter space [120]. Dividing an image into several smaller images would resolve this problem. However, fibres which are cut off at the edge are difficult to detect due to the lack of circular shape. Applying the circular Hough transformation to the images captured provided inaccurate results because multiple fibres were not located in combination with erroneous provided fibre locations. Applying the same algorithm to reference images of a Glass Fibre (GF)-Polypropylene (PP) sample provided much better results with respect to the CF tapes. Because the average diameter of GF is larger compared to CF, it can be stated that higher magnification images

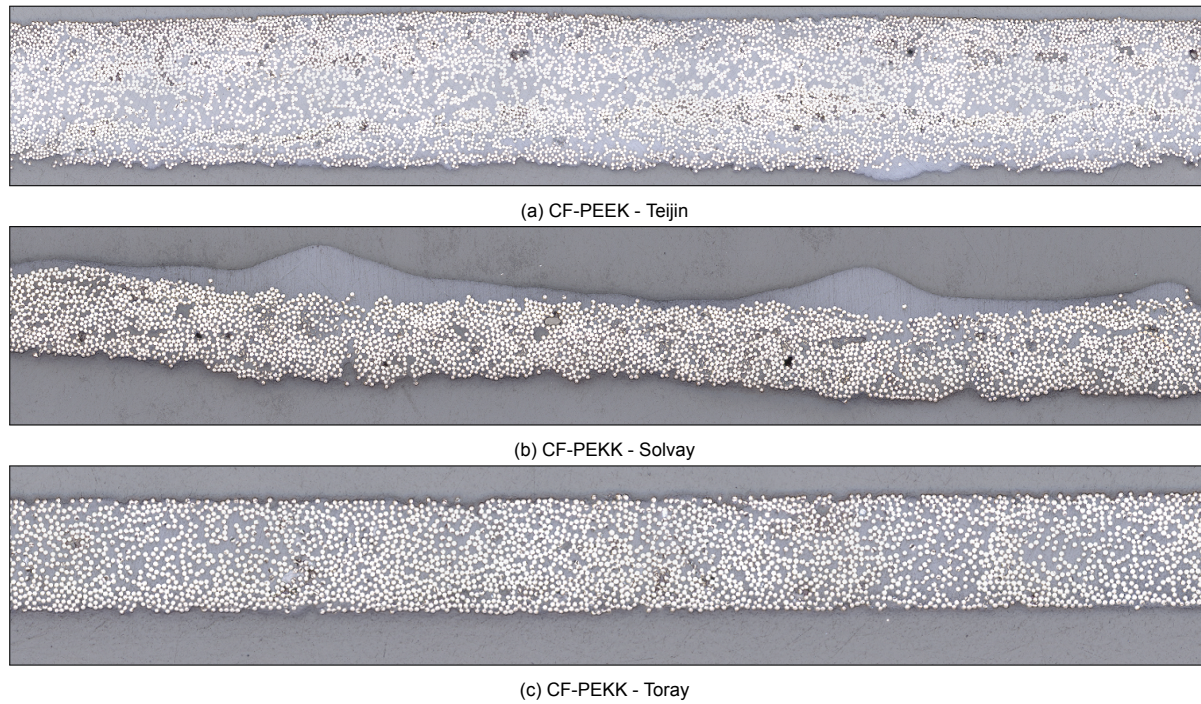


Figure 3.4: Overview of micrographs of the PEEK and PEKK tapes

are required in order to apply the circular Hough transform to CF images. The latter is in agreement with work from Zangenberg et al. [120], where the the circular Hough transform was applied successfully to CF micrographs obtained using a Scanning Electron Microscope (SEM) with a remarkable higher magnification. A SEM was considered but not selected due to the limitations in micrograph size.

Detecting the fibre locations based on pixel intensity showed enhanced accuracy and consistency with respect to the circular Hough transform algorithm. The open source image processing software package ImageJ is capable of detecting objects based on pixel intensity, the so called 'find maxima' function [122]. The captured micrographs described in section 3.2 are divided into equal-width images with pixel (px) dimensions as presented in table 3.2. The dimensions in pixels are not exactly the same because each of the three larger micrographs, with approximately the same dimensions, are divided in 20 smaller images. Images analysed using the 'find maxima' function of ImageJ must be blurred in order to increase the accuracy of local maximum detection [123]. By blurring the images the pixel intensity of each pixel is replaced with an averaged intensity based on the surrounding pixels. This limits the false detecting of local maxima. The 'Smoothing' function in ImageJ is used for this and the most optimal 'Smoothing' parameter for each UD tape is presented in table 3.2. The noise tolerance parameter defines the difference in pixel intensity with respect to the surroundings a pixel should at least have in order to become a local maximum [122]. In other words, increasing the value for this parameter reduces the amount of detected maxima. The smoothing and noise tolerance parameter settings are determined based on trial and error by checking the accuracy of detecting all fibres while reducing the erroneous detection of locations without a fibre. The parameters are tuned based on a small micrograph section and are thereafter applied to each individual micrograph section. The differences in optimal search parameters between the CF-PEEK tape and the two CF-PEKK tapes can

	Height [px]	Width [px]	Smoothing	Noise tolerance	Local maxima
CF-PEEK Teijin	734	856	4x	>3	2601
CF-PEKK Solvay	679	867	9x	>10	1004
CF-PEKK Toray	738	880	9x	>10	1051

Table 3.2: ImageJ parameters used for the local maxima detection

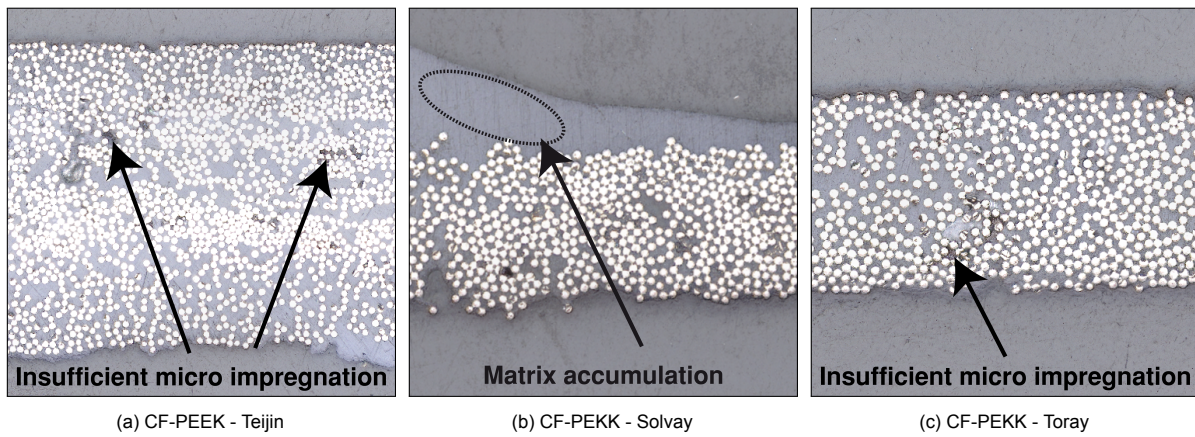


Figure 3.5: Micrographs presenting material defects of the PEEK and PEKK tapes

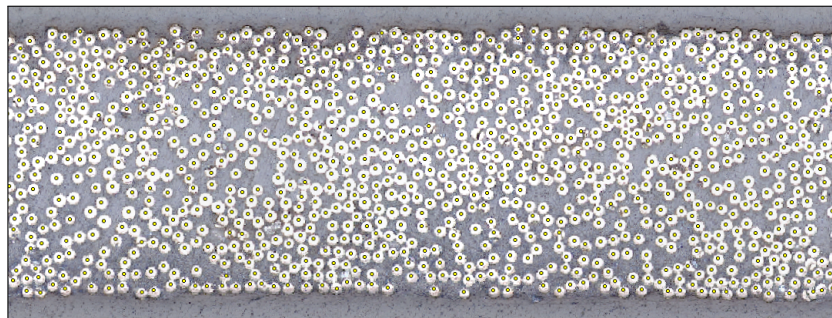


Figure 3.6: UD tape fibre coordinate extraction using ImageJ

be explained by the difference in reflective behaviour of the different fibres, visible in figure 3.5a - figure 3.5c. Figure 3.6 shows a screenshot of a result of the fibre location determination by using ImageJ. Fibres located at vertical boundaries of the image are not selected because of an algorithm preset, mainly because fibres are cut off due to splitting the large image into several smaller images.

The average amount of local maxima (i.e. fibres) of the image sections for each UD tape is provided in the last column of table 3.2. A large variation in detected fibres per image section is observed for the three UD tape micrographs analysed. This difference can be explained with the following analysis. First of all, the width in pixels of the tape sections analysed deviate to some extent. Table 3.3 presents the width of the analysed micrograph sections in meters, the transform from pixels to meters is achieved by measuring the Keyence MultiFileAnalyzer scale with ImageJ. The three UD tapes analysed consist for 34 weight percent (wt.%) of resin, meaning that the UD tapes contain 66 wt.% fibres [65, 66, 124]. However, it cannot be stated that each tape sample analysed contains an identical amount of fibres in weight terms because the ply areal weights [g m^{-2}] of the different suppliers are not identical [65, 124]. The fibre weight of the image per unit length is calculated with

$$Fibre_{IW} = Fibre_{AW} * Width \quad (3.1)$$

where $Fibre_{AW}$ is the fibre areal weight multiplied with the width of the captured image in meters. Because only the thickness and width of a cross-section can be considered, this parameter is expressed in terms of unit length x . The amount of fibre area required to achieve the fibre weight (per unit length) of the image depends on the density of the fibre. Both PEKK tapes contain HexTow AS4D fibres [65, 66] with a density of 1.79 g cm^{-3} [125], almost similar to the 1.78 g cm^{-3} density of the CF Tenax-E fibres used for the PEEK tape of [124, 126]. The overall cross-sectional area covered by fibres in a particular micrograph section $A_{fibre(MS)}$ can be determined according to

$$A_{fibre(MS)} = \frac{Fibre_{IW}}{\rho_{fibre}} \quad (3.2)$$

	Width [m]	Ply AW [g m ⁻²]	Fibre AW [g m ⁻²]	Fibre IW [gx ⁻¹]	A _{fibre(MS)} [m ²]	A _{fibre} [m ²]	Fibres
CF-PEEK Teijin	4.71E-04	288 [124]	190 [124]	0.0895	5.03E-08	1.96E-11	2561
CF-PEKK Solvay	4.77E-04	220 [66]	145 [66]	0.0692	3.87E-08	3.53E-11	1097
CF-PEKK Toray	4.84E-04	221 [65]	145 [65]	0.0706	3.94E-08	3.53E-11	1118

Table 3.3: Results explaining the difference in local maxima observed in the micrographs sections

where ρ_{fibre} is the density of the carbon fibre. The last column of table 3.3 presents the theoretical amount of fibres, calculated with

$$Fibres = \frac{A_{fibre(MS)}}{A_{fibre}} \quad (3.3)$$

where A_{fibre} is the average cross-sectional area of a fibre. The theoretical number of fibres presented are the number of perfectly circular fibres to meet the 66 wt. % condition.

The large difference in the theoretical amount of fibres to be detected, between the PEEK and PEKK tapes mainly originates from the variation in ply areal weight and the amount of fibres required to comply with the total fibre area of the cross-section, due to varying fibre diameters. The calculated theoretical amount of fibres do not perfectly match the amount of extracted local maxima as presented in table 3.2. The percentage differences between the theoretical analysis and the extracted local maxima for Teijin, Solvay and Toray are 1.54%, 9.26% and 6.37%, respectively. Erroneous detection of fibres result in a higher amount of local maxima. However, it is expected that this is not likely because all images are manually checked after the ImageJ algorithm is applied. The most likely cause of this difference on the analysis side is due to the assumption that all fibres are circular and have a constant cross-section, which is not the case by analysing micrographs like figure 3.5a - figure 3.5c. Additionally, the 34 wt% of resin is an averaged parameter which can slightly vary throughout the UD tape and therefore introduce slight inconsistencies in the amount of fibre and resin present in a tape section.

3.3.2. Fibre Coordinate Data Post-Processing

By using ImageJ it is possible to apply the Voronoi pattern to an image, however the data post-processing possibilities of ImageJ are limited. For this reason Python is selected as data post-processor. Post-processing of the data can be described by using 10 function blocks, as presented in figure 3.7. Each Python function of the code provided in appendix A can be described by one of the function blocks. In this section the underlying principle of each function block is elaborated on.

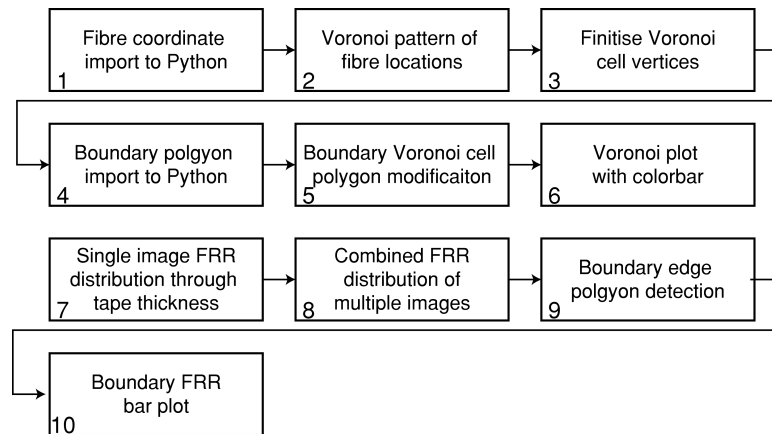


Figure 3.7: Material analysis with Voronoi pattern functional blocks

The fibre coordinates extracted using ImageJ of each image section are imported to Python. Because of a different definition of axis system, the y-coordinates from ImageJ are flipped over the horizontal axis to match the regular axis system of Python. Function block 2 represents the formation of the 2-dimensional Voronoi pattern applied to the fibre locations. The basic Voronoi tessellation function in

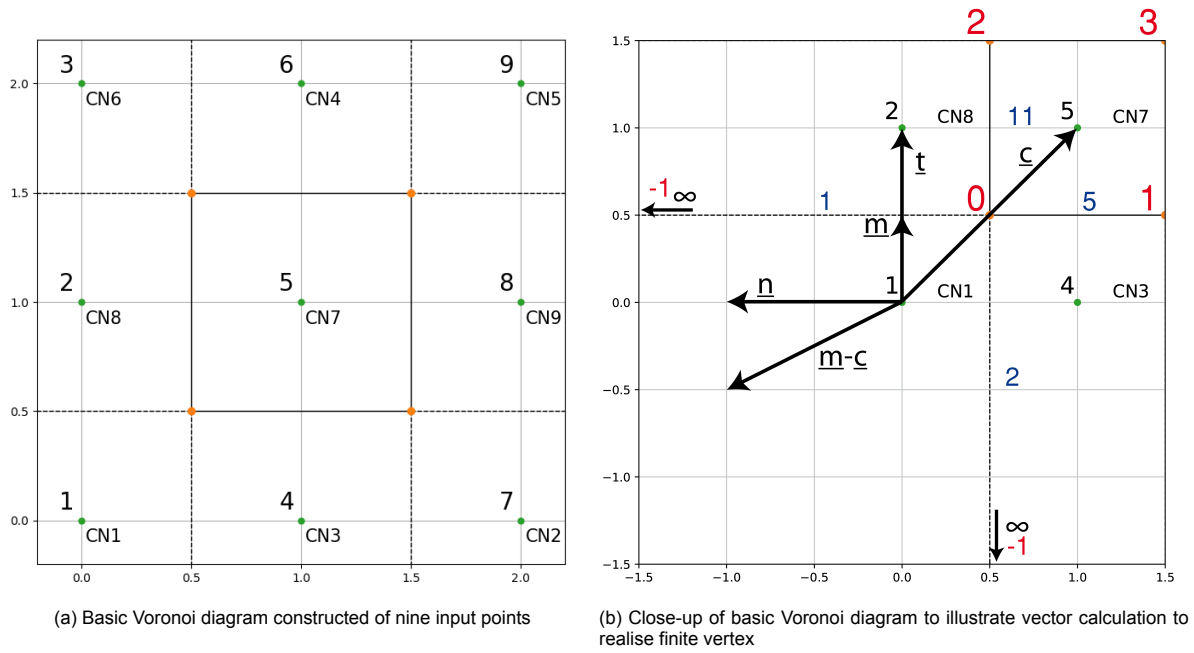


Figure 3.8: Visualization of transformation from infinite to finite Voronoi vertices of a basic diagram

Python provides several outputs [76]. The x- and y-coordinates of the Voronoi cell vertices are given next to the Voronoi regions. The region lists the Voronoi vertex indices creating a particular Voronoi cell. By analysing figure 3.1d, it is clear that several Voronoi cell vertices are not located on the plane of the analysed section, these vertices are at infinity and denoted with index -1.

The Voronoi vertices at infinity are made finite in order to perform further analysis such as area calculation of the Voronoi cell. The main principle behind function block 3 can be described with the following equation

$$[Finite\ point] = [Voronoi\ vertex] + ([Direction] \cdot Radius) \quad (3.4)$$

where the radius is a scalar term, the Voronoi vertex and direction terms are 2x1 vectors. The exact process to finitize the Voronoi vertices at infinity is described in detail in the remaining part of this paragraph.

Figure 3.8a shows a basic Voronoi diagram constructed of nine input coordinates, depicted as green dots. The Voronoi cell vertices are illustrated with orange dots. The four black continuous lines represent Voronoi ridges which are part of the finite region whereas the black dashed lines are ridges going to infinity. The Voronoi Cell Numbers (CN) are also added to the figure. Note that the order of CN's is chosen by Python, and not in such way that it corresponds to the input coordinate numbers. A close-up of the lower left corner of the Voronoi diagram is presented in figure 3.8b. The red numbers are the indices of the Voronoi vertices, where -1 represents an index at infinity and the blue numbers represent Voronoi ridge indices. The Voronoi vertex of ridge 1 is used to further describe the method to make the Voronoi vertices finite. This process is only initiated if a Voronoi cell is constructed with one or more vertices at infinity. This is clearly the case for Voronoi cell number 1 because it is constructed by vertices with index 0 and -1. Voronoi ridges can be interpreted as lines drawn perpendicular to a line connecting two input coordinate positions, this can also be seen in figure 3.1d. In the case of figure 3.8b, ridge 1 is the perpendicular line between input point 1 and 2. A normalized tangent vector is derived in between the vectors describing input location 1 and 2, described with p_1 and p_2 . The tangent vector equals

$$\underline{t} = \begin{bmatrix} X_{p2} \\ Y_{p2} \end{bmatrix} - \begin{bmatrix} X_{p1} \\ Y_{p1} \end{bmatrix} = \begin{bmatrix} 0.0 \\ 1.0 \end{bmatrix} \quad (3.5)$$

and the normalized tangent vector

$$\underline{\hat{t}} = \frac{\underline{t}}{\sqrt{X_t^2 + Y_t^2}} = \begin{bmatrix} 0.0 \\ 1.0 \end{bmatrix} \quad (3.6)$$

remains the same for this particular situation. Next the normal vector of \underline{t} is derived by exchanging the x- and y-coordinate of \underline{t} and multiplying with -1, resulting in:

$$\underline{n} = -1 \cdot \begin{bmatrix} Y_t \\ X_t \end{bmatrix} = \begin{bmatrix} -1.0 \\ 0.0 \end{bmatrix} \quad (3.7)$$

The next vector required to determine the direction vector, \underline{d} of equation 3.4 is calculated by considering the midpoint and centre vector. The midpoint (\underline{m} in figure 3.8b) is determined with

$$\underline{m} = \begin{bmatrix} \frac{X_{p1}+X_{p2}}{2} \\ \frac{Y_{p1}+Y_{p2}}{2} \end{bmatrix} = \begin{bmatrix} \frac{0.0+0.0}{2} \\ \frac{0.0+1.0}{2} \end{bmatrix} = \begin{bmatrix} 0.0 \\ 0.5 \end{bmatrix} \quad (3.8)$$

and the centre vector (\underline{c} in figure 3.8b) is determined based on the centre of all input points. The direction vector, \underline{d} requires to calculate the dot product of the vectors $\hat{n} - \underline{c}$ and \hat{n} , which in this case gives a positive value because the angle between the vectors is smaller than 90 degrees. This implies that the direction in which the infinite point is made finite is equal to the direction of the normal vector. If for example the centre position would be completely different, the dot product can be become negative meaning that the angle between both vectors is larger than 90 degrees and less than or equal to 180 degrees. The latter would mean that the infinite Voronoi vertex is made finite in the opposite direction of the normal vector. The 'Radius' term in equation 3.4 describes the distance with which the Voronoi vertex is made finite. For this example the radius has been selected to be four, for the actual UD tape analysis the radius is selected to be twice the value of the largest fibre x-coordinate or y-coordinate. For this specific case, the infinite Voronoi vertex is made finite starting at the Voronoi vertex on the other side of the Voronoi ridge, which is already in the finite region, in direction of the \underline{d} vector. Additionally, the finite point at $x = -3.5$ and $y = 0.5$ replaces the point at infinity. When all these steps are repeated for the infinite point of Voronoi ridge 2, Voronoi cell 1 is described by finite Voronoi vertices. The process described above is repeated for each Voronoi vertex at infinity.

Other research related to the application of the Voronoi algorithm to GF composite samples simply ignore the Voronoi cells at the image boundary because in their case they cannot be evaluated explicitly [120]. Because especially the local Fibre-Resin Ratio (FRR) at the tape edges is of interest for the UST process, a method is developed to define the tape boundary such that fibres located close to the tape edges can be included in the analysis. Function block 4 is related to the process of defining the tape boundaries by constructing a polygon in ImageJ. A defined boundary results in a finite Voronoi cell meaning that the area of the cell can be calculated. Because especially the boundary fibre-resin architecture is of interest, a detailed and accurate UD tape boundary definition is required. Therefore a manual method of defining the boundary by constructing a polygon in ImageJ is used. This process involves a polygon definition by using the 'Polygon selection' option in ImageJ. Figure 3.9 shows a micrograph of the CF-PEKK tape from Solvay with a boundary polygon defined. To ensure a smooth obtained polygon, three additional points are added between each defined point by using interpolation. Function block 4 is finalized with a transformation of polygon coordinates to an export file, which can be imported to Python.

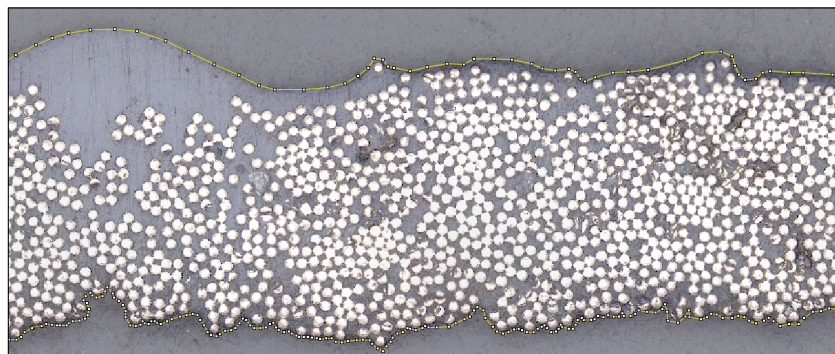


Figure 3.9: CF-PEEK Solvay tape boundary definition by constructing a polygon in ImageJ

	$D_{\text{fibre}} - \text{theoretical} [\mu\text{m}]$	$D_{\text{fibre}} - \text{measured} [\mu\text{m}]$
CF-PEEK Teijin	5.0 [126]	4.99
CF-PEKK Solvay	6.7 [125]	6.31
CF-PEKK Toray	6.7 [125]	6.31

Table 3.4: Theoretical and average measured fibre diameters of Tenax-E-24K and HexTow AS4D-12K fibres

The next Python function, described by function block 5, ensures that all Voronoi cells are shaped according to the tape boundary polygon. The Voronoi cells with ridges which are modified according to the process described in function block 3 are intersected with the defined boundary polygon. The polygon clipping function of python can be used to detect whether a polygon intersects with a specified boundary [76]. In case of the UD tapes, if an intersection occurs the original Voronoi cell ridge is modified according to the tape boundary resulting in a closed polygon with edges corresponding to the tape boundary. The latter means that the area of this specific cell can be defined. In case of no contact with the boundary polygon, the Voronoi cell remains unchanged. The ConvexHull function from the SciPy Spatial module is used to define the area of the Voronoi cells [76]. The microstructure of the UD tapes is characterized by defining the local FRR. This ratio is calculated with

$$FRR = \frac{A_{\text{fibre}}}{A_{\text{Voronoi cell}}} \quad (3.9)$$

where the fibre cross-sectional area is assumed to be circular and constant. The fibre diameter of the three different tapes were measured at various locations of various images by using ImageJ. Using the pixel to mm ratio, an average pixel diameter was determined. Table 3.4 provides the theoretical and average measured fibre diameter of all three UD tapes. A slight variation between the theoretical and measured value for the fibres of the PEKK tapes is observed, however this variation is consistent between both tapes which can be related to the fact that the tapes both contain HexTow AS4D-12K fibres [65, 66]. The average measured fibre diameters were used to calculate the FRR of each Voronoi cell, to remain consistent with the micrographs obtained.

Each Voronoi cell is filled with a colour based on the FRR value, ranging from 0 to 1. A FRR of 0 physically means that the Voronoi cell is infinite whereas a FRR of 1 implies that the area of the Voronoi cell is equivalent to the average fibre cross-sectional area. A Voronoi diagram including FRR colour plot of a CF-PEEK tape section from Teijin is provided in figure 3.10. By analysing this image it immediately becomes clear that the fibre-resin distribution is not homogeneously distributed. The red coloured Voronoi cells present cells with a FRR larger than 1, which is physically impossible. This means that the calculated area of the Voronoi cell is smaller compared to the average cross-section area of a fibre. A FRR larger than 1 can be explained with two possible situations. Either the Voronoi cell is defined not precisely meaning that the actual area surrounding the fibre is larger, or the average fibre cross-sectional area is not in agreement with the cross-section of that specific fibre. A FRR larger than 1 would negatively influence further analysis performed and therefore the FRR of such Voronoi cell is set to 1. In addition, if more than 1% of the total Voronoi cells provide an FRR of larger than 1, an error message is provided and consequently the analysis parameters such as the fibre positions or boundary definition should be re-examined.

The variation in FRR of each Voronoi cell is further analysed, this is described by function block 7. To determine the FRR through the thickness of the tape, the tape is divided into several segments. The Python code written for this function performs checks in which segment a fibre is located and considers the FRR ratio of that specific Voronoi cell to be part of the segment. Due to the small thickness of a single ply UD tape, the tape samples did not remain straight throughout the embedding process. Besides this, it is also possible that the captured image is not completely parallel to the UD tape sample. Therefore, dividing Voronoi diagram figures like figure 3.10 into perfect horizontal segments would provide inaccurate data. To be able to accurately divide the tape into thickness segments, an inclination is introduced to the segments, visualized by black coloured lines. These lines are described by the basic linear $y = ax + b$ equation where the inclination of the lines is based on the midpoints of the left and right tape boundaries. Due to a variance in tape thickness, the amount of segments is varied such that each tape is divided in an equal amount of segments through the thickness of the UD tape. The

average FRR ratio per segment through the tape thickness is presented in a graph in figure 3.11. Note that the vertical position of the through thickness distribution depends on the vertical position of the tape in the micrograph.

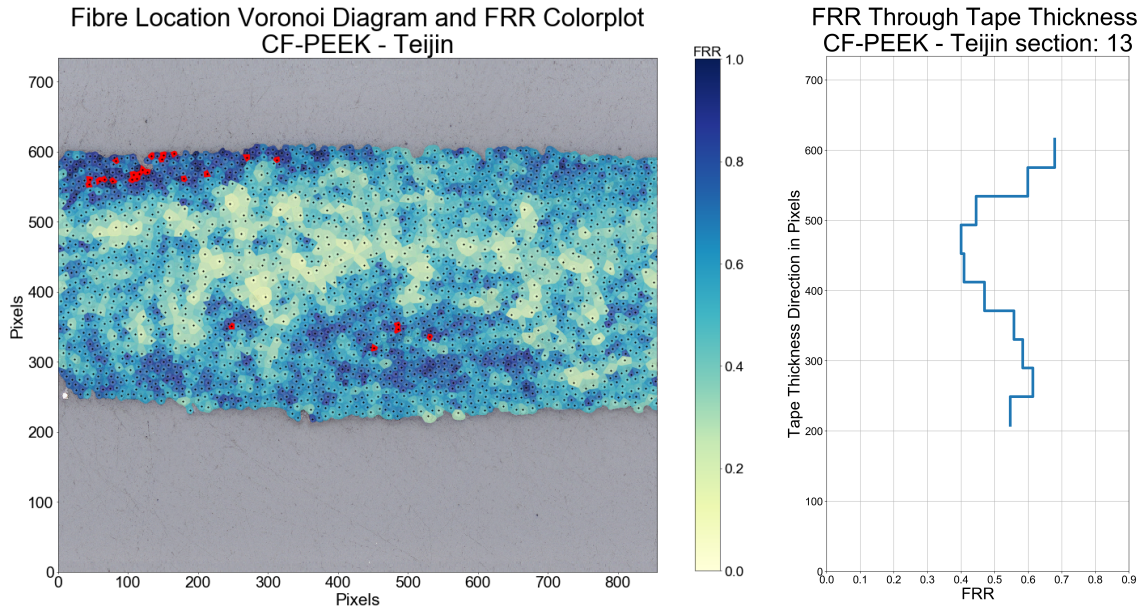


Figure 3.10: Voronoi diagram with FRR colour plot of Teijin CF-PEEK tape section Figure 3.11: Corresponding through tape thickness FRR distribution of Teijin CF-PEEK tape section

The output of function block 7 is used as input for the Python function described by function block 8. Because multiple micrographs are analysed per UD tape, a combined average FRR plot through the tape thickness is calculated. These results are presented in section 3.4.

As already mentioned in section 3.1, function block 9 and 10 are implemented to analyse the fibre-resin architecture at the tape edges. The boundary Voronoi cells are detected by using part of function block 5. If the area of a Voronoi cell is not influenced by the polygon clipping it means that the cell is not constructed by a boundary polygon, and visa versa. The FRR of the Voronoi cells in contact with the upper and lower tape edge are considered for this part of the analysis, meaning that a concentrated tape top and bottom surface analysis is performed. Figure 3.12 shows detected boundary Voronoi cells in a micrograph of the Solvay tape. Function block 10 characterizes the process of realising a FRR bar plot of Voronoi cells located at the tape edges, either the top or bottom surface.

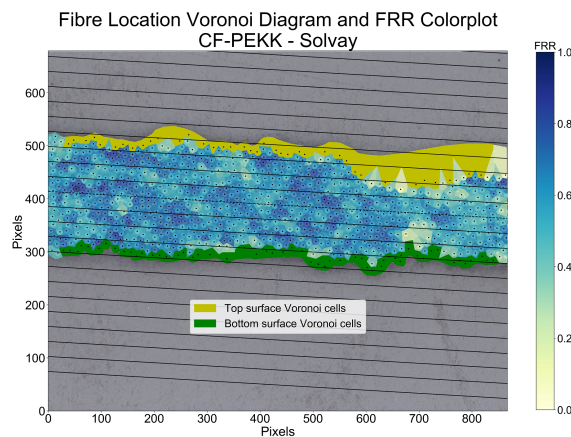


Figure 3.12: Upper and lower boundary Voronoi cell detection of Solvay CF-PEKK tape

3.4. Results and Discussion

For the completeness of the analysis, two neighbour micrographs with the Voronoi diagram and colour plot applied are provided of each UD tape analysed in figure 3.13 - figure 3.15. Large variations in homogeneity of fibre-resin distribution are observed in the tapes from Teijin and Solvay. The tape from Toray shows minor variation but still does not show perfect homogeneous distributed fibres, which is impossible to find in reality [118].

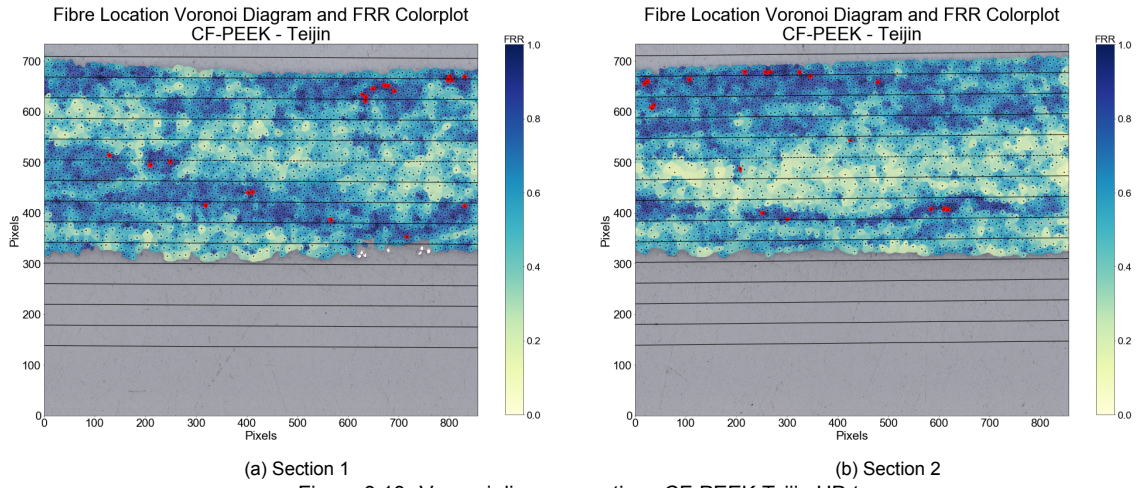


Figure 3.13: Voronoi diagram sections CF-PEEK Teijin UD tape

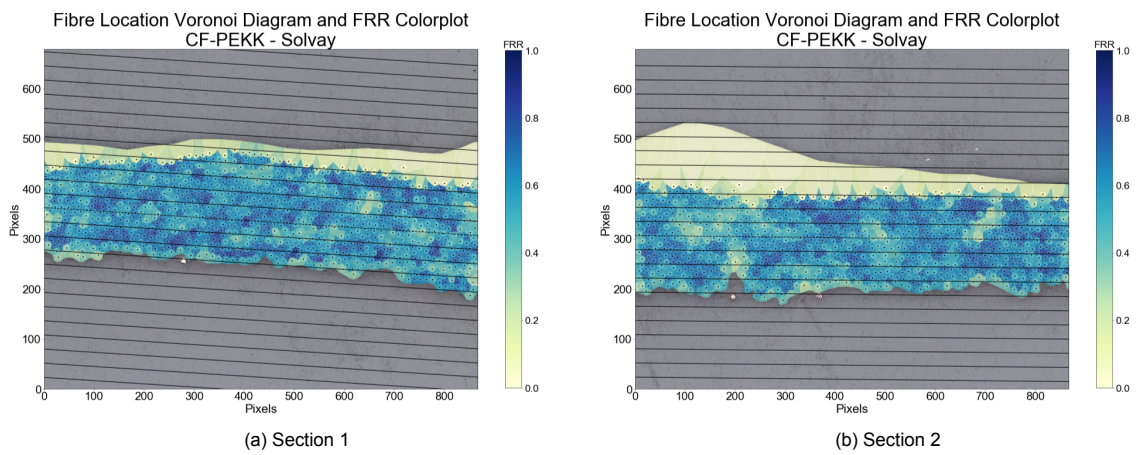


Figure 3.14: Voronoi diagram sections CF-PEKK Solvay UD tape

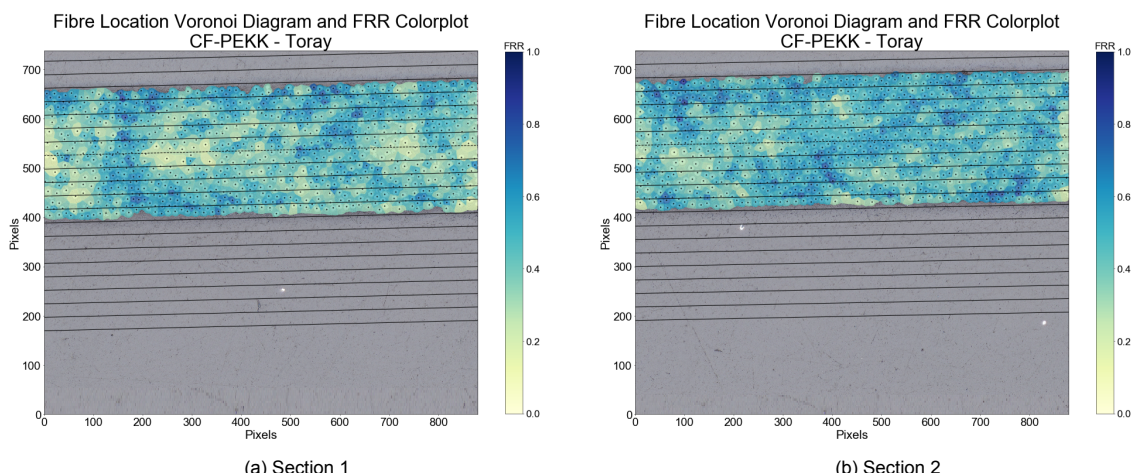


Figure 3.15: Voronoi diagram sections CF-PEKK Toray UD tape

In figure 3.16 - figure 3.18 the FRR distributions of the tapes analysed is presented. These graphs are constructed by combining individual results, similar to those presented in figure 3.11, of several micrographs in one figure. The blue dashed lines represent the (average) tape top and bottom surface. The first noticeable aspect of the results is the different positioning of the FRR plot of the Solvay CF-PEKK tape. In this case the total thickness of the 10 segments is not equivalent to the mean tape thickness, presented in table 3.1. The latter can be explained by the large presence of TP matrix accumulation, especially at the top surface. This additional matrix material is not included in the total thickness of the 10 segments as each segment in the analysis should at least contain one fibre. The actual position of the through thickness distribution, with respect to the top and bottom tape surface is determined based on the ratio between the amount of resin present at the top and bottom tape edge. This ratio is extracted from the bar plots presented in figure 3.19a - figure 3.19c. This positioning ratio is applied to each of the graphs presented in figure 3.16 - figure 3.18, but have limited effect on the graphs corresponding to the Teijin and Toray tapes due to small to no matrix accumulation at the tape edges. By considering the CF-PEKK section of the micrograph presented in figure 3.5b, it is clear that more TP resin is present at the top surface, for this reason the through thickness FRR plot is slightly moved towards bottom tape surface. The thickness of the PEEK and PEKK tapes from Teijin and Toray respectively, are relatively well described by using 10 segments. As a result of the rather straight surface behaviour in combination with the lack of TP resin accumulation.

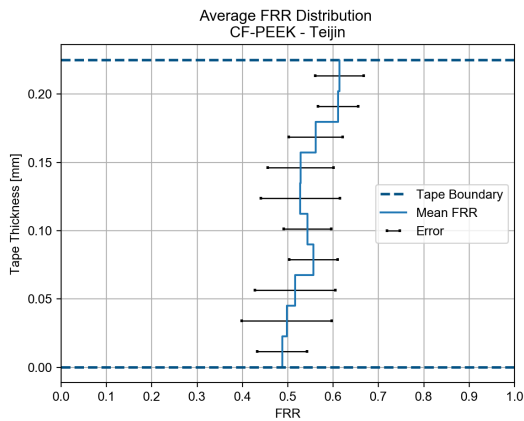


Figure 3.16: Mean FRR through thickness CF-PEEK - Teijin tape

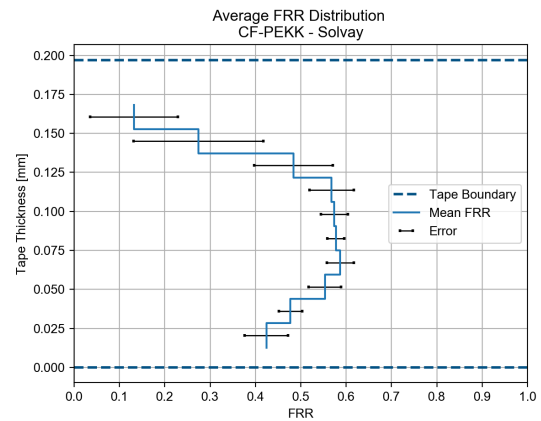


Figure 3.17: Mean FRR through thickness CF-PEKK - Solvay tape

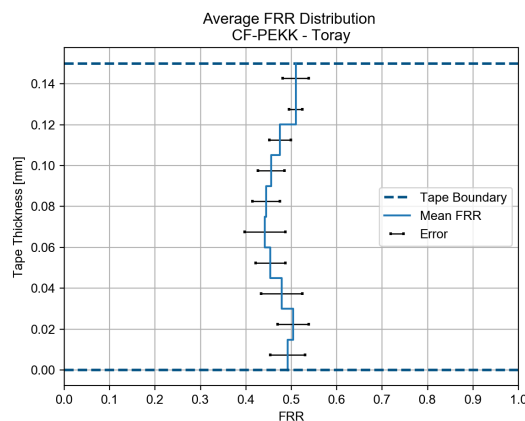


Figure 3.18: Mean FRR through thickness CF-PEKK - Toray tape

The FRR distribution characterizing the Teijin tape displays fibre rich surfaces, especially the top surface. The bottom FRR is equivalent to the bottom FRR of the Toray tape, but shows much more

variation over the various micrographs analysed. This can be explained by regions of fibre clustering, also visible in figure 3.4a. These variations in arrangement of fibres can cancel out for the mean FRR, but introduce large variations in data resulting in large error values. Besides little variation the Toray tape shows a rather constant FRR through the tape thickness. The Voronoi cells at the upper boundary of the Solvay tape are definitely more resin rich compared to the mid-section and bottom surface of this tape. Meaning that this tape is especially resin rich at the top surface. The error bars in figure 3.17 emphasize that these large amounts of TP resin, especially at the top surface of the tape are not consistently present in each micrograph analysed. This is substantiated by looking at the two micrographs presented in figure 3.14a and figure 3.14b. The FRR distribution through the tape thickness of the Teijin and Toray tapes are greatly different compared to the tape from Solvay. The tapes from Teijin and Toray show more fibre rich areas at the tape edges and is more resin rich towards the mid-section of the tape, which is in contrast to the Solvay tape.

Figure 3.16 to figure 3.18 show that each UD tape microstructure is unique. However, these figures do not emphasize the tape boundary FRR. The FRR of the boundary Voronoi cells are heavily averaged and thus influenced by underlying Voronoi cells in these segments. Figure 3.19a - figure 3.19c present the average FRR of solely the Voronoi cells in contact with the tape outer surfaces. It can therefore be described as a concentrated FRR analysis of the tape outer surfaces.

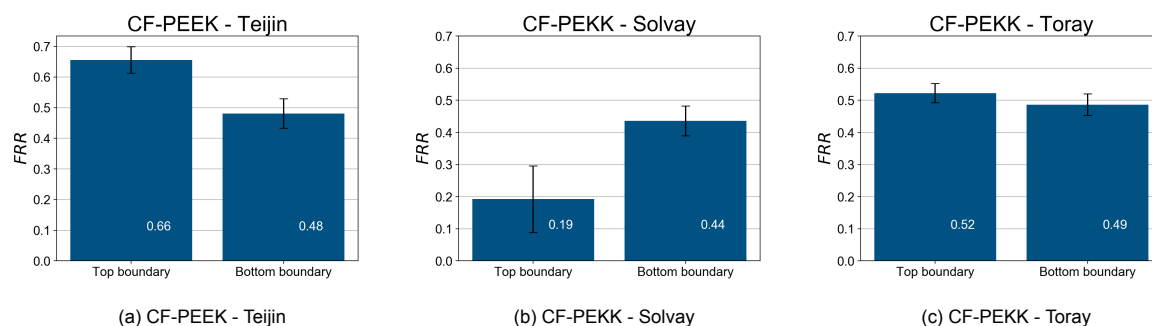


Figure 3.19: Mean FRR bar plot of Voronoi cells intersecting with UD tape top and bottom surfaces

The FRR of the outer segments of figure 3.16 - figure 3.18 are extracted and compared with the localized surface boundary FRR from the bar plots, the results are provided in table 3.5. According to the differences presented, the FRR of the outer segments in the distribution analysis are roughly similar to the FRR of the localized boundary analysis for the Teijin and Toray tape. This can be explained by considering the rather straight surface behaviour. Due to the segmental approach, fibres and corresponding Voronoi cells located in the vicinity of the tape surfaces are included in the outer segments. Meaning that the underlying Voronoi cells of the tape surfaces are characterized with a roughly similar FRR compared to the Voronoi cells in contact with the tape boundaries. Considering that the localized analysis is more accurate in describing the FRR it is concluded that the through thickness distribution slightly over-predicted the amount of resin at the top surface for the Teijin and Toray tape. The opposite is true for the bottom surface of these tapes.

	Distribution analysis		Concentrated analysis		Δ	
	Top FRR	Bottom FRR	Top FRR	Bottom FRR	Top FRR	Bottom FRR
CF-PEEK - Teijin	0.619	0.487	0.656	0.481	6.8%	1.2%
CF-PEKK - Solvay	0.132	0.424	0.192	0.436	45.5%	2.8%
CF-PEKK - Toray	0.501	0.492	0.523	0.486	4.4%	1.2%

Table 3.5: Accuracy analysis results of outer tape surfaces FRR between distribution analysis and localised analysis

The differences between the distribution analysis and the localized analysis are relatively large for the Solvay tape. The differences are related to the irregular surface shape of the tape, especially due to the amount of waviness at the top surface of the tape. By closely looking to the top surface of

figure 3.12, it can be concluded that only two Voronoi cells are included in the most upper segment of the through thickness distribution. With this comparison it is clear that the localized analysis, which only considers the Voronoi cells in contact with the tape edges, is a more in describing the microstructure at the Solvay tape surfaces. Figure 3.19b shows that the FRR of the bottom surface is twice the FRR of the top surface, meaning that the top surface of the Solvay tape is at least twice as resin rich compared to the bottom surface.

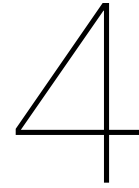
3.5. Concluding Remarks

Applying the Voronoi algorithm to the cross-sectional micrographs, in combination with the local FRR can be used to quantify and describe the microstructures of the CF UD tapes from Teijin, Solvay and Toray. The results presented in the previous section emphasize the large variety in microstructure of the UD tapes analysed. Besides the variation in TP resin and the type of CF, the microstructure greatly varies between the various tapes. Because the analysis of each tape includes several micrographs, the degree of variation present in a specific tape can be quantified.

The CF-PEEK Teijin tape is characterized by a resin rich region towards the bottom surface of the tape in combination with regions of fibre clustering. The bottom surface FRR of the Teijin tape is equivalent to the FRR at the bottom surface of the Toray tape. Nevertheless, the bottom surface of the Teijin tape comprises more variation compared to the Toray tape. The latter shows the most consistent and homogeneous microstructure of all three tapes analysed with minor matrix accumulation in the mid-section of the tape, compared to the outer surfaces. The PEKK tape from Solvay displays much surface waviness on microscopic level, combined with a resin rich upper surface. Compared to the mid-section of this tape, the bottom surface can be described as slightly resin rich.

Based on the results of the three tapes analysed, it is concluded that the localized analysis is favoured for tapes showing much surface waviness combined with matrix accumulation at the outer surfaces. The outer surfaces of straight tapes such as those from Teijin and Toray can be correctly described by the segmental through thickness analysis, and do not necessarily require the localized analysis. This because the surface boundary FRR is not heavily influenced by underlying Voronoi cells with corresponding FRR for straight surfaces.

The results obtained from the characterization of the microstructures analysed are in agreement with the aforementioned order of ease of tacking. The resin rich upper surface of the PEKK tape manufactured by Solvay explains why processing this specific tape is less challenging compared to the other PEKK and PEEK tapes. Especially the fibre rich top surface of the tape manufactured by Teijin explains why processing the PEEK tape is challenging. The bottom surface FRR of the Teijin tape and Toray tape are identical, for both types of analysis. However, the variation of FRR at the bottom surface is 20% to 30% larger for the Teijin tape. Meaning that larger inconsistencies (fibre clustering) are present for the Teijin tape including scattering of resin rich regions present at the bottom surface (visible in figure 3.4a). The inconsistent bottom surface combination with the fibre rich top surface emphasizes the difference in ease of tacking between the Teijin and Toray tape. Considering the relevant material properties for UST of PEEK and PEKK are roughly identical (refer to table 2.1), it is concluded that the microstructure of a UD plays a major role in the UST process.



Quality Quantification of Tacked Unidirectional Tapes

Section 4.1 describes the methodology of the experiment to quantify the bond strength of tacked Unidirectional (UD) tapes. Section 4.2 motivates the use of the Mandrel Peel (MP) test. Important design considerations are presented in section 4.3, redesign aspects are mentioned in section 4.4. Section 4.5 describes the validation of the MP setup. A few concluding remarks are presented in section 4.6.

4.1. Methodology of Experiment

As mentioned before, no experimental setup was available at Boikon at the start of this project. A trade-off is established to determine which peel strength assessment method suits best to this project. Afterwards, the MP setup was designed and build at the facility of Boikon, with a minimal budget and without the use of a sophisticated mechanical test bench. ASTM standards are present how to perform peel tests using specific MP equipment [87, 127]. No literature was found addressing tacking quantification of Thermoplastic (TP) UD tape samples prior to consolidation based on peel strength. Therefore, the prescribed ASTM standards are not obeyed due to the lack of data for comparison. A MP setup able to provide reliable and consistent data meets the requirement to reflect on the change in bond strength when tacking parameters are altered. Before designing the MP setup several preliminary tests were performed to proof the concept of applying this specific peel test to tacked UD tapes prior to consolidation. HiCAD, a 3D CAD software package was used to design the MP setup, using some guidelines from literature. Little time was spend for the design phase as it was believed that design flaws are easily filtered out throughout the construction phase. While assembling the MP setup some parts did not work out as planned, and were modified accordingly. This results in rapid realisation of the MP setup. Validation was considered a highly important process since this eventually defines how accurate the experimental setup is.

4.2. Motivation of Mandrel Peel Test

A trade-off table presented in table 4.1 has been established to determine, based on the method descriptions provided in section 2.3, which method best suits this project. The four experimental methods described in section 2.3 are evaluated based on five selected criteria. Before selection of the experimental method, it was studied if one of the UD tapes could be applied to a rigid metal strip by using 3M double sided adhesive tape. For every bond condition tested (i.e. various tacking parameters utilized), the tacked bond between the two UD samples failed when manually peeling off the upper adherend. This showed that the experimental methods are not limited to tests containing two flexible adherends.

The first criteria is related to the ability to achieve a constant peel angle when performing peel strength tests for identical tapes tacked with different tacking parameters. For the T-peel and Fixed-arm peel test, a constant peel angle cannot be ensured when the peel strength of stronger bonds is assessed. In other words, a stronger bond is more constraint resulting in a different peel angle with respect to

	T-peel test	Fixed-arm test	Floating roller test	Mandrel test
Constant peel angle	False	False	True	True
Ability to compare tapes with different stiffness	False	False	True	True
Dimension limitations of samples due to weak bond	False	False	True	False
Active possibility to modify conformity	N.A.	N.A.	False	True
Level of difficulty to design, built and validate setup	Low	Moderate	High	High

Table 4.1: Trade-off table peel strength assessment method

a relatively weak bond. A constant peel angle can be ensured for the two roller assisted peel tests when determining the peel strength of identical tapes with varying Automated Tape Laying (ATL) settings. A constant peel angle can be ensured because the flexible adhered follows the curvature of the roller/mandrel, if conformity is realised.

This project is related to UD tapes containing Carbon Fibre (CF) fibres with a Polyetheretherketone (PEEK) or Polyetherketoneketone (PEKK) TP polymer from different suppliers. To compare bond strengths of these tapes, it is necessary that the experimental method selected is capable of eliminating any difference in tape characteristics, for example the stiffness of the tape. The bending stiffness greatly influences the bending radius which consequently influences the peel force measurements. The floating roller and MP test have the ability to measure the friction of the system by testing an unbonded sample. A favourable aspect of this friction run is that it also includes the force required to bent the flexible adherend over the curvature of the roller/mandrel and can therefore be eliminated from the bond strength [88].

The peel force of a continuous Ultrasonic Tacking (UST) process is high likely to have quite some variation due to the fibre-resin variation in the UD material in combination with a rather sensitive tacking process. The latter is substantiated with peel force results from welded woven composite parts [89], and welded UD samples [88]. For this reason it is of interest to observe the peel force over a longer section, enabling the possibility to average the bond strength over a certain length. The stroke of the linear vertical displacement unit is considered identical for each experimental method, and is therefore not part of the trade-off. Nevertheless, the floating roller peel test experiences some limitations, due to the low bond strength, in terms of sample length to prevent tilting of the rigid adherent.

As described, conformity is an important aspect for the assisted roller methods because this increases the reliability of the obtained data and makes comparison between tapes possible. Ensuring conformity can be done by increasing or decreasing the roller radius. Besides this, the MP test is generally equipped with an alignment force to stimulate conformity, see figure 2.20.

Since none of the four peel strength experimental methods is available at Boikon, the method selected should be designed, built and thoroughly validated within the timespan of this project. The T-peel test only requires two fixtures which can be attached to the linear vertical motion system. For the fixed-arm peel test, a base fixture with specified inclination is required. This increases the difficulty to built with respect to the T-peel test. The fixture required for the floating roller (figure 2.18) is a quite critical part, especially the positioning of the rollers. The other roller assisted peel test is also relatively difficult to realize. Mainly because of the mandrel in combination with the horizontal displacement unit.

The arguments provided above, in combination with table 4.1, motivates that the MP test is the most feasible strength assessment method for this project.

4.3. Design of Experimental MP Setup

The horizontal displacement of the MP test is commonly realized with a roller conveyor in combination with a rigid slide beam [90] or a linear guide rail [91]. A small roller conveyor of 35.5 mm height and 39.5 mm width with minimal roller resistance was in sufficient length available at Boikon, and was therefore selected as a starting point for the design phase of the MP test. As mentioned in section 2.3.4, the minimum mandrel radius R should be such that the maximum elongation of the fibres in the UD tapes is not exceeded meaning that

$$R_{mandrel} > \frac{h}{2\epsilon_1} = \frac{0.2}{2 * \frac{1.8}{100}} = 5.56\text{mm} \quad (4.1)$$

where h and ϵ_1 represent the thickness and the maximum strain in fibre direction of the peel arm, respectively. The relevant UD tapes for this project have an approximate thickness of 0.2 mm. The fibres in the PEKK UD tapes are AS4D carbon fibres [66] which have an ultimate elongation of 1.8% [88, 125]. The CF in the PEEK tapes are Tenax- fibres with an elongation at break of 2.1% [126]. To be conservative, 1.8% is taken as ϵ_1 for equation 4.1. This results in a minimum mandrel radius of 5.56 mm, because of availability a mandrel with 20 mm radius was employed. The setup total length was set to 1000 mm, such that approximately 500 mm of continuous tack can be assessed.

The roller conveyor dimensions, the minimum mandrel radius and the total setup length were the three starting points for the design phase. Figure 4.1 provides an image of the final design. The mandrel is attached to the two vertical pillars in such a way that the distance between the metal slide beam and the mandrel's curved surface can easily be adapted. The width of the slide beam is 48.5 mm so that it is equal to the width of the UD tapes utilized at Boikon. Four vertical positioning plates were included in the design to ensure that the sideways motion of the slide beam is restricted. The tacked UD tape can be applied to the slide beam by using 3M double sided adhesive tape and is then pulled upwards by following the curvature of the mandrel.

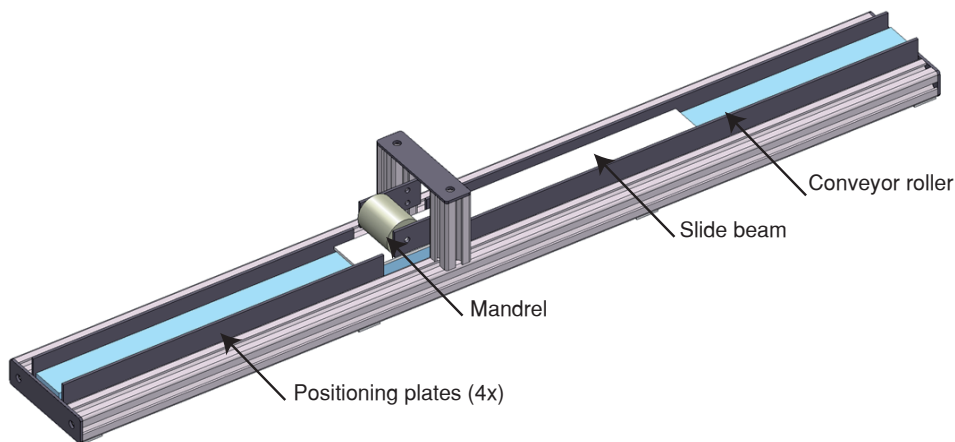


Figure 4.1: 3D HiCAD design of the mandrel peel test setup

The design of the linear vertical displacement unit is presented in figure 4.2. A Bahr Modultechnik trapezoidal spindle with a 510 mm stroke in combination with a Beckhoff servo was selected to realise the linear motion. A timing belt with a 22 teeth pulley and a 60 teeth pulley transfers the rotational motion of the servo to the spindle. An appropriate fixture to fixate the UD tape to the linear vertical displacement unit was utilized in the workshop of Boikon without creating a 3D design first, because of the simplicity of this part. The 40 mm offset between the carriage plate and the force gauge plate was required to prevent contact between the UD tape fixture and the spindle. A force gauge from PCE Instruments was utilised for this application to accurately measure and log the peel force. The selected force gauge is capable of measuring forces up to 50 N with a 0.01 N resolution and 0.5 % accuracy.

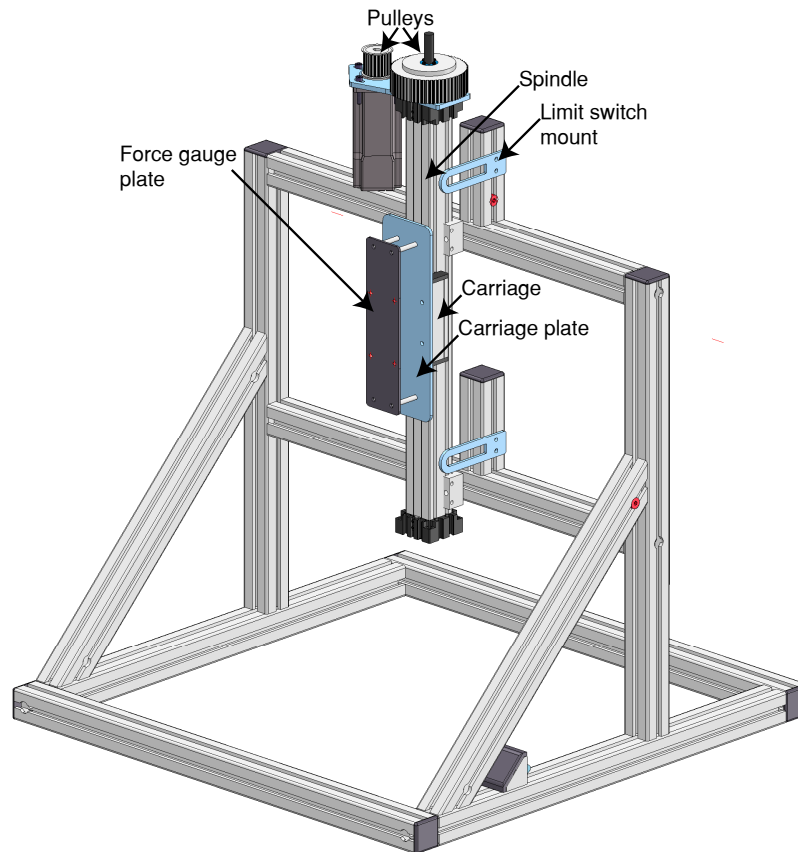


Figure 4.2: 3D HiCAD design linear vertical displacement unit

4.4. Construction of Experimental MP Setup

A photograph of the MP test setup is provided in figure 4.3. Note that the photograph was taken after a peel test was completed, meaning that this is the most upward position of the linear vertical displacement unit. Figure 4.4 shows in more detail how the linear vertical displacement unit interacts with the MP test by using the tape fixture depicted in figure 4.5.

Comparing the MP test from the photograph with the initial 3D design from figure 4.3, several differences can be observed. First of all, the vertical position plates were removed in the final design. During initial test trails it was found that the interaction between the slide beam and the vertical positioning plates heavily influenced the friction of the system in an inconsistent manner. Removing the vertical positioning plates did not introduce sideways motion of the slide beam if the UD tape was applied to the slide beam accurately, meaning without an angle. Furthermore, the 3 mm thick slide beam was replaced by a rectangular aluminium profile with a 50 x 20 mm cross-section. During initial test trials the thin slide beam showed minor deformation which influenced the measured peel forces. In addition, the weight of the slide beam is increased by adding a steel profile in the rectangular profile to ensure overall contact between the slide beam and the roller conveyor, this modification resulted in two slide beams of exactly 3 kg. The final modification with respect to the initial 3D design is related to the implementation of an alignment force to ensure conformity of the flexible adherend to the curvature of the mandrel. As mentioned in literature, simple dead weights can function as alignment force [88, 90]. A rope with four 300 gram weights was attached to the slide beam, as can be seen in figure 4.6. The upper pulley is used to minimise the friction of the moving rope whereas the second pulley was included to reduce sideways motion of the rope between both pulleys in order to have a more constant alignment force.

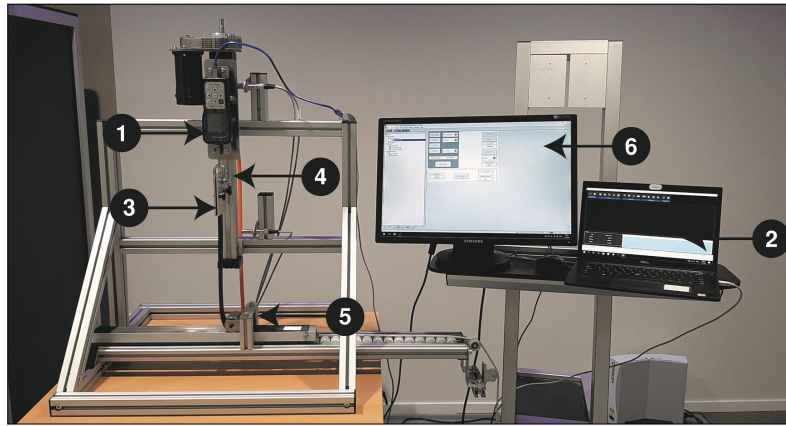


Figure 4.3: Mandrel peel test experimental setup. 1: Force gauge, 2: Computer with data logging software, 3: Tape fixture, 4: Trapezoidal spindle drive, 5: Mandrel peel test setup, 6: PLC software interface

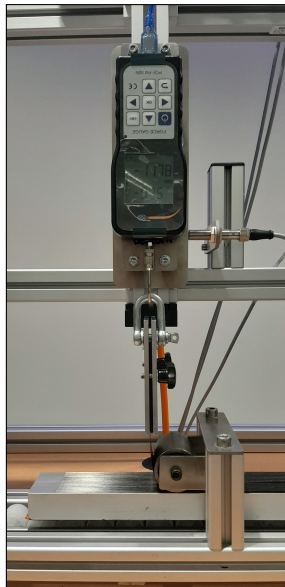


Figure 4.4: Close up of interaction between force gauge and mandrel peel test setup



Figure 4.5: Photograph of UD tape fixture

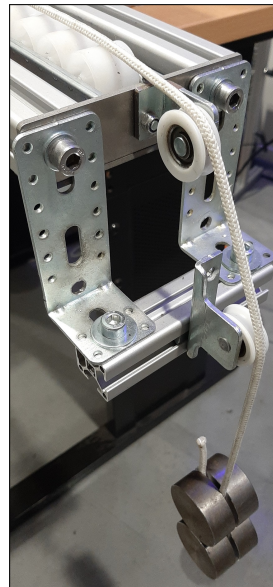


Figure 4.6: Photograph of pulley system for alignment weights

4.5. Validation of Experimental MP Setup

The experimental setup presented in the previous section is validated by using various trial runs in order to determine the reliability and accuracy of the setup. Two identical slide beams are utilized to decrease the time interval between initiating various tests. While neglecting the bond strength data from the samples analysed, the force required to move the slide beams in combination with the friction of the system was logged and studied. Figure 4.7 presents the force versus displacement graphs of three friction runs at 0.5 mm s^{-1} peel rate for both slide beams using CF-PEEK samples. For each run the average friction force is calculated between $x = 50 \text{ mm}$ and $x = 200 \text{ mm}$, these specific parameters are chosen to reduce any possible begin and end effects of the dynamic setup. The three graphs presented in figure 4.7a can be described with an average friction force of 17.80 N, 18.08 N and 17.68 N, resulting in an average friction of 17.85 N with a standard deviation of 0.17 N. The equivalent friction forces for slide beam 2 presented in figure 4.7b are 17.97 N, 17.55 N and 17.60 N which results in an average friction of 17.71 N with a variance of 0.19 N. The latter emphasizes that the force gauge in combination with the MP test setup for unbonded samples is capable of producing consistent data.

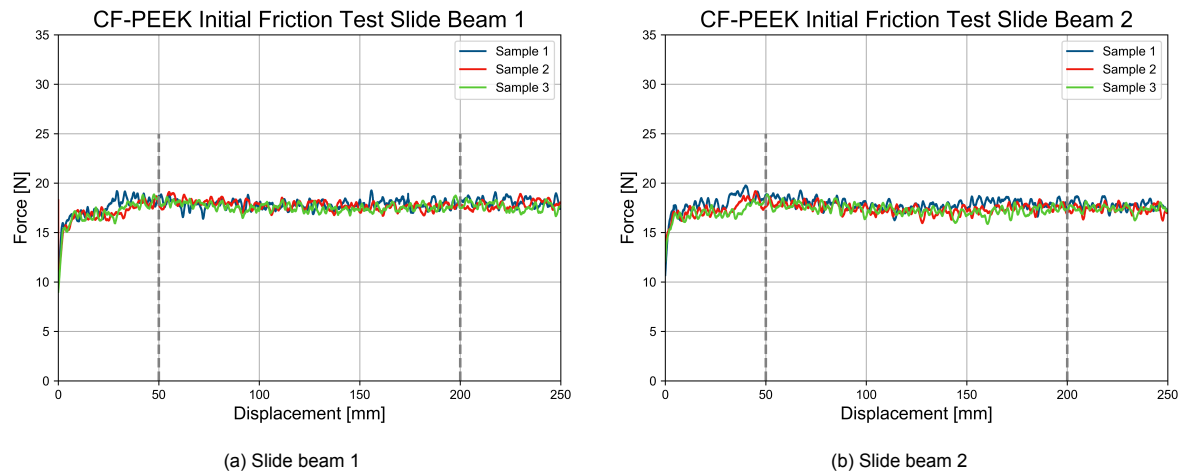


Figure 4.7: Initial friction tests for mandrel peel test setup validation using CF-PEEK samples

According to literature, various peel rates are utilized for the MP test [87, 88, 90, 127, 128]. However, the most common peel rate utilized is 30 mm min^{-1} [87, 127, 128]. In research considering peel rates of 3 mm min^{-1} and 30 mm min^{-1} , it was concluded that the peel rate had no significant influence to the test results [127, 128]. To determine if this also holds for the current MP test setup, three experiments with different peel rates are performed. A higher peel rate is time-wise more efficient, for this reason peel rates of 30 mm min^{-1} , 300 mm min^{-1} and 900 mm min^{-1} are examined. Three replicates are used for each peel rate, meaning that in total nine samples are realized with the Falko ATL by using the same tacking process parameters. The obtained peel force data is presented in figure 4.8 - figure 4.10, the use of the trend lines is explained in the next section. Remarkable is the increase of peel force along the sample length with varying slopes for the three peel rates examined. Similar behaviour was observed by others and explained by describing the effect of fibre bridging at the fracture zone [87, 90]. Fibre bridging increases the toughness of the bonded UD tapes due to fibres which interact between the upper and lower UD tape at, or beyond the fracture zone [87]. Fibre bridging was observed and captured using a camera during the MP test, and became more substantial towards the end of the UD tape sample. Figure 4.11 and figure 4.12 show photographs of fibre bridging observed during peel tests of CF-PEEK tapes.

To quantify the peel force of an UD sample, it is necessary to express the peel force with a single value. When the peel force shows a rather constant graph, it is reasonable to average the peel force over the total sample length [89]. A plateau zone in the peel force graph can also be used to calculate the average peel force of the sample by averaging the peel force over this specific plateau zone [88, 90]. For consolidated UD tapes samples, a plateau can be observed in the peel force versus displacement graph, meaning that the effect of fibre bridging is minimal [90]. By using this plateau value, it is possible to average the peel force over a certain section [88, 89]. In contrast to the aforementioned consolidated UD samples, a plateau zone is not observed in the graphs of figure 4.8 - figure 4.10. This is explained by considering that the fibres for the tacked UD tape samples are not, or only locally consolidated meaning that fibres in the tape are less constrained compared to consolidated laminates. Since neither a constant peel force or plateau zone was observed in the graphs obtained, it was necessary to utilize a different method to express the peel force of a specific sample by using a single number.

An analytical model capable of expressing the peel force and the amount of fibre bridging for an UD tape sample is proposed. The peel force graph between a start and end position is described with

$$y = Ax^2 + B \quad (4.2)$$

by using least squares polynomial fit, where coefficient A and B are used to describe the amount of fibre bridging and the peel force respectively. The trend lines describing each individual UD sample are also presented in the aforementioned peel force graphs. To ensure that the dynamic MP test setup is in steady state condition, begin and end effects are neglected when the measured peel force is described using the model presented above. Only a sample section of 150 mm is considered to ensure

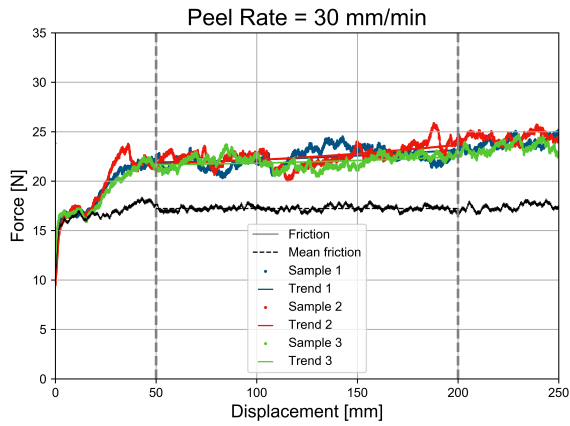


Figure 4.8: Peel rate comparison for mandrel peel test setup validation - 30 mm/min peel rate

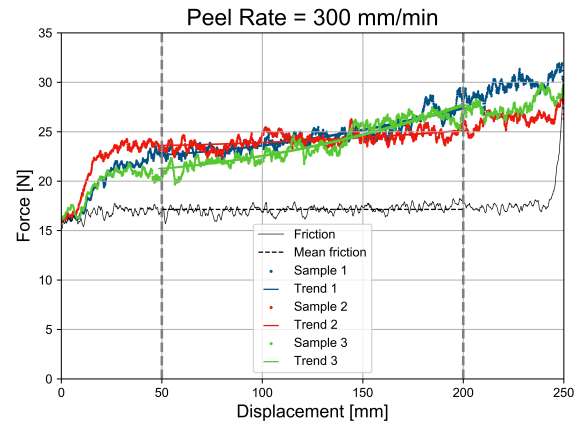


Figure 4.9: Peel rate comparison for mandrel peel test setup validation - 300 mm/min peel rate

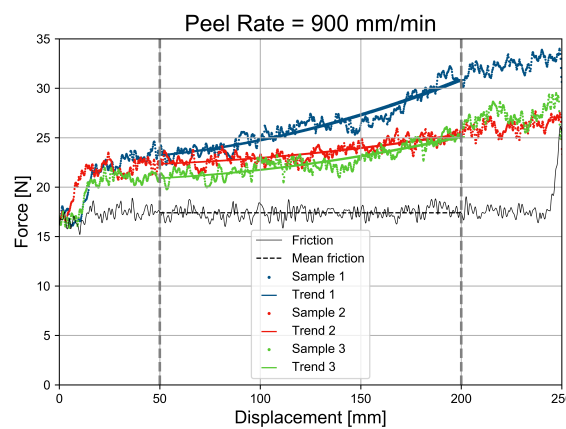


Figure 4.10: Peel rate comparison for mandrel peel test setup validation - 900 mm/min peel rate

this dynamic condition of the experimental setup. Bar plots in figure 4.13 and figure 4.14 show the average A and B coefficients of the three replicates, for each peel rate. The average friction force is subtracted from the peel force graphs in order to describe the bond strength with the coefficient B . The friction force is not described using equation 4.2 because the friction curve is rather constant according to figure 4.7, and is therefore averaged over the same length used for the peel force model. Subtracting the constant friction force (different for each peel rate) from the peel force graphs only influences the B coefficient and does not influence the slope of the graph, meaning that coefficient A remains the same. Applying the exact same model to the graphs presented in figure 4.7 results in A coefficients which are approximately 20 times smaller with respect to the coefficients presented in figure 4.13. This demonstrates that the slope, and therefore coefficient A can be related to the interaction of bonded samples. The latter in combination with the fibre bridging and fibre pull out observed in figure 4.11 and figure 4.12 substantiates the design criteria of the analytical model to relate the coefficient A to fibre bridging/fibre pull-out.

Clearly indicated in figure 4.13 is the difference in coefficient A of equation 4.2 for the different peel rates. The small value for A for the lowest peel rate explains that the peel force remains rather constant over the sample length. The small error value for the 30 mm min^{-1} peel rate, in comparison to the higher peel rates, describes that the peel force graphs are more consistent for the lower peel rate. The average sample peel strength, described with coefficient B varies from 4.4 N to 5.1 N for the three studied peel rates. Eventhough the peel rate has limited effect on the average B value, a relatively large difference is observed when considering the error values. Only a variation of 0.1 N was observed for the 30 mm min^{-1} peel rate, in contrast to 1.1 N for the 900 mm min^{-1} peel rate. The mentioned findings from



Figure 4.11: Photograph showing the presence of fibre bridging during the MP test at the front side of the mandrel



Figure 4.12: Photo showing the presence of fibre pull-out during the MP test at the back side of the mandrel

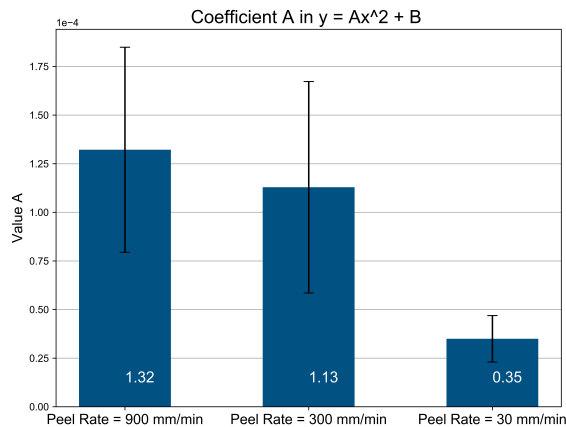


Figure 4.13: Peel force behaviour: peel rate vs coefficient A

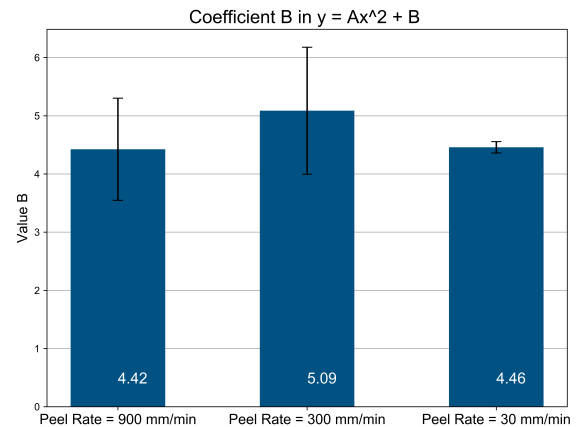


Figure 4.14: Peel force behaviour: peel rate vs coefficient B

Sacchetti et al. [128] and Sacchetti et al. [127] related to the peel rate can be considered partially true for the current MP setup. By describing the peel force graphs with equation 4.2, the average bond strength values are almost identical for each peel rate. The latter is not the case for coefficient A , which is related to the slope of the peel force graph and related to fibre bridging and fibre pull-out.

4.6. Concluding Remarks

Amongst the experimental methods presented in section 2.3, it was concluded that the MP test suits best to replace the manual peel test in order to quantify the bond strength of the UST process. This was mainly based on the aspect to accurately compare the bond strengths of samples processed with different tacking process parameters, and between tapes with different TP matrix materials. The effect of peel rate to the peel force measurements has been thoroughly studied. Consistency and accuracy in peel force measurements are essential aspects of the MP setup in order to quantify the tacking quality of the UST process. Eventhough the experiments are considerably more time consuming with a low peel rate, the limited increase of slope (coefficient A) and low error value for the bond strength (coefficient B) are considered more important and decisive. Therefore a peel rate of 30 mm min^{-1} is utilized for the MP setup.

5

Experiments and Analysis of Tacked Unidirectional Samples

Section 5.1 provides a Bond Line Length (BLL) comparison using micrographs of tacked samples, which is eventually related to the results of the microstructural characterization presented in chapter 3. Section 5.2 describes the parameter study performed using Design of Experiment(s) (DOE) and reflects on the results of the statistical model, including an analysis on the contribution of the predictors to the bond strength. Section 5.3 relates the variation in peel force to observed variance in tape microstructure.

5.1. Bond Line Comparison of Tacked UD Tape Samples

As presented in chapter 3, the microstructures of the analysed Polyetheretherketone (PEEK) and Polyetherketoneketone (PEKK) tapes vary in degree of homogeneity. This section presents the measured bond length based on various micrographs of all three (tacked) Unidirectional (UD) tapes, what is related to the obtained Fibre-Resin Ratio (FRR) distributions. Additionally, the UD PEKK tape manufactured by Solvay is analysed in more detail to see the effect of resin rich surface layers at the interface on the total length of the established bond.

5.1.1. Methodology of Experiment

Three cross-sectional micrographs are obtained of each tape, using a Keyence VK-X1000 3D laser scanning confocal microscope. The obtained micrographs of the locally tacked samples are analysed in ImageJ where the length over which a bond is established is measured, referred to as BLL. The inconsistencies and variations in BLL are eventually related to the microstructural characteristics of the UD tapes. Two additional Solvay PEKK samples are prepared, one containing both resin rich surfaces at the interface while the other does have the fibre rich surfaces facing each other at the interface. This to emphasize the advantageous effect of a resin rich interface on the bonded region.

5.1.2. Preparation and Microscopy of Samples

Two individual layers of UD tape were tacked with the Falko Automated Tape Laying (ATL), according to the settings presented in table 5.1. No visual damage was observed on the samples prepared with the specified tacking parameter settings. As the tape laying head accelerates and decelerates the tacking parameters are changed accordingly using pre-defined tacking parameters. The samples used for microscopy are obtained from the midsection of the sample, defined by 'Test stroke' in figure 5.1. This to ensure that the samples are not influenced by the acceleration and deceleration of the ATL, associated with slightly different tacking parameters. In total five samples are realized, one for each type of UD tape and two additional Solvay Carbon Fibre (CF)-PEKK samples. From each tacked sample three smaller sections were cut such that the bond length can be determined at various locations of the tacked sample, which increases the accuracy of the analysis. Each individual section cut from the samples are within the 'Test stroke' region. Identical preparation steps as presented in section 3.2 were performed for the 15 mm (\parallel to fibre) x 10 mm (\perp to fibre) tacked samples.

	A	P	V
CF-PEEK Teijin	95	17	50
CF-PEKK Solvay	95	12	100
CF-PEKK Toray	95	18	100

Table 5.1: Amplitude [%], Pressure [%] and Velocity [mm s^{-1}] used for bond line experiment samples

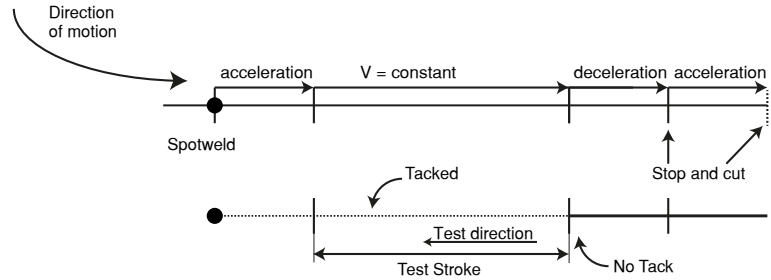


Figure 5.1: Schematic visualization of preparation of UD test strokes

5.1.3. Bond Length Measurements

The length over which a bond was established during the tacking process is measured using the image processing software ImageJ. Figure 5.2 depicts a section of a Toray CF-PEKK micrograph. The arrows visualize how the bond region is measured over a straight line. Due to the design of the sonotrode, ideally a bond is established at multiple individual locations. The imprint in figure 5.2 characterizes one of those locations. The bond length was measured at each of those locations for each sample. The lengths were measured in pixels, and translated to microns afterwards. For completeness the micrograph sections are presented in appendix B showing the regions where a bond was expected due to the design of the sonotrode. If present, the arrows indicate the BLL.

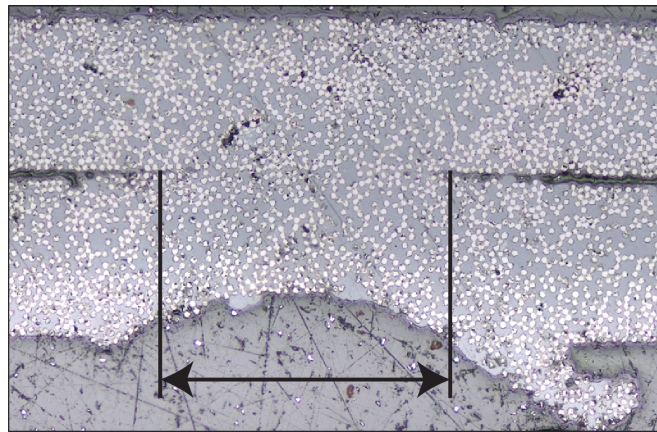


Figure 5.2: Example of bond length determination method

5.1.4. Results and Discussion

The measured bond lengths in microns are represented in a bar chart per sample, as shown in figure 5.3. The inserts in this figure represent the FRR distributions of two stacked tapes. The single ply FRR distributions from chapter 3 are reused, and positioned accordingly. The first thing noticed is the consistent behaviour at which locations a bond is established for the Toray tape, a bond region was consistently observed at four locations for each sample. This is clearly not the case for the Teijin and Solvay tape. Remarkable is that with roughly identical tacking parameters and half the tape laying velocity the Teijin tape is only bonded over a mean length of roughly $300 \mu\text{m}$, what is only 25% of the Toray mean bond line. The ratio standard deviation over mean value ratio results in 19%, 16% and 6% for the Teijin, Solvay and Toray tape respectively. A ratio was used to express the differences as purely comparing the standard deviations would be inaccurate because the magnitudes of the mean values are not identical. The consistency in tack locations of the Toray tape, in combination with the lowest aforementioned ratio is in agreement with the nearly constant (two-ply) FRR distribution. The rather inconsistent behaviour observed from the tacked Teijin and Solvay tapes can be associated with the relatively large error bars in the thickness segments towards the tape interface. Meaning, the variation in the amount of resin and fibres present at the interface of both UD tapes reflects on the established BLL during tacking.

Total Bond Line Length Comparison

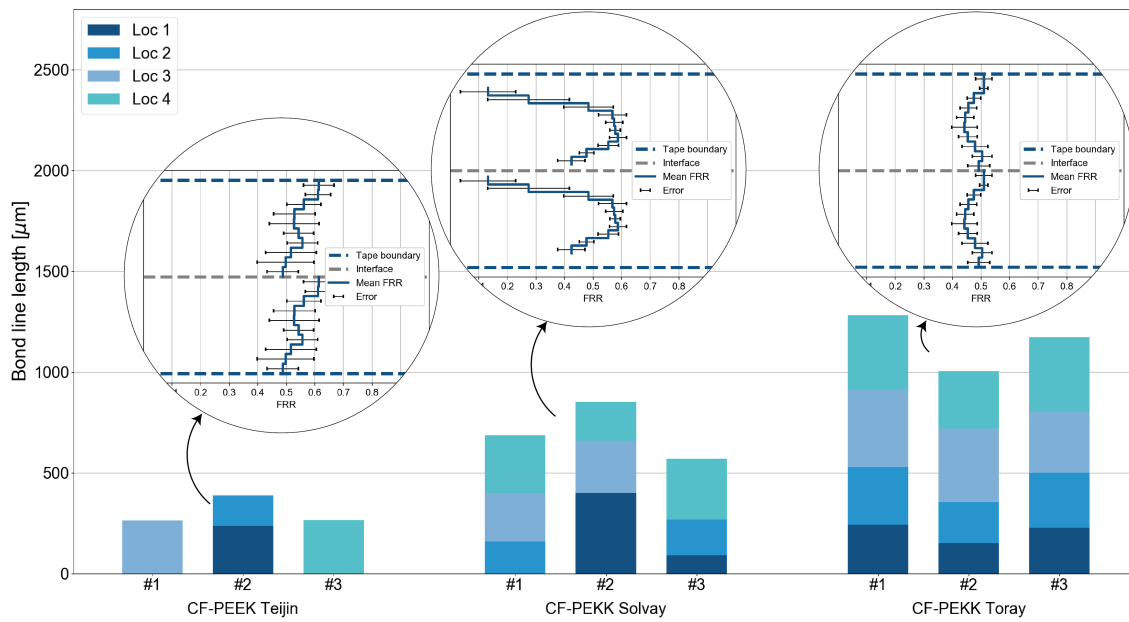


Figure 5.3: Bar chart representing bond line comparison of tacked CF-PEEK and CF-PEKK tapes

Figure 5.4 emphasizes that two resin rich outer surfaces facing each other at the interface results in a large BLL. The mean BLL of the Solvay samples with the resin rich sides facing each other provided a mean bond length of 886 μm , which is twice the value of the samples containing both fibre rich surfaces at the interface. During the embedding process the resin in one sample cup holder did not cure properly, resulting in the loss of the third section of both samples. Nevertheless, based on the two micrographs captured of each sample it can be concluded that more resin present at the interface is favourable for the length of the bond region, and consequently for the strength of the bond.

CF-PEKK Solvay Bond Line Length Comparison

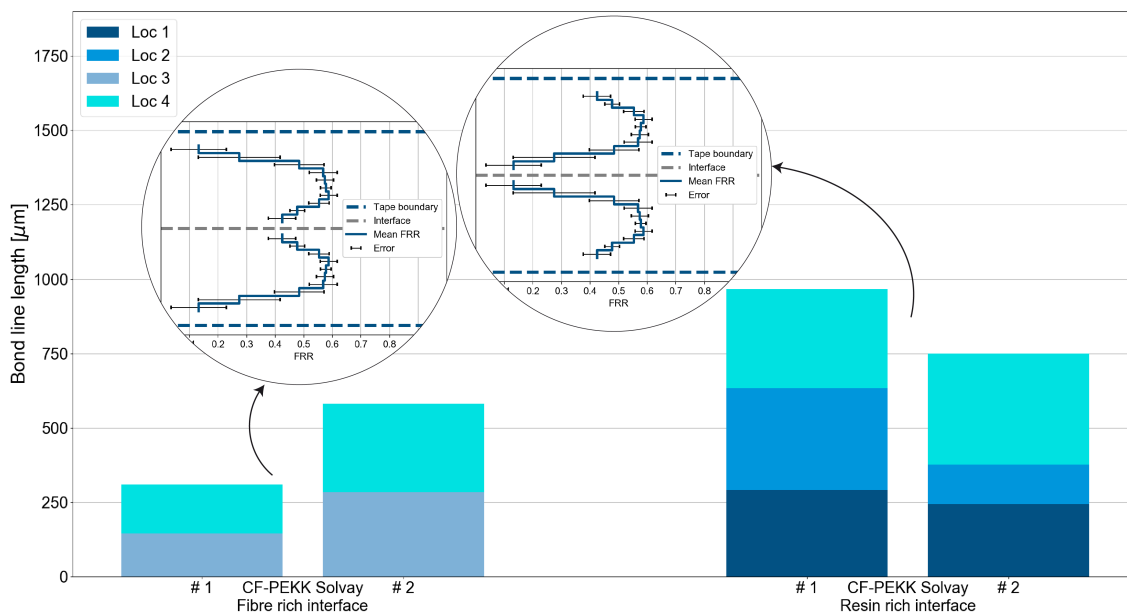


Figure 5.4: Bar chart representing bond line comparison of tacked Solvay CF-PEKK tapes

5.1.5. Concluding Remarks

Based on the presented experiment it is concluded that the microstructural characterization can be related to the degree of consistency in BLL of tacked samples. Consistent bonded regions were observed for the Toray tape which is characterized by a rather constant FRR distribution, especially when considering the two ply FRR distribution. Remarkable is the fact that in terms of bond region a tape with slightly fibre rich surfaces, but with a constant FRR distribution is favoured compared to resin rich tape showing an inconsistent FRR distribution. Furthermore, the influence of resin rich surfaces facing each other at the interface is shown to be favourable for the BLL, even for a tape which is characterized by an inhomogeneous distribution of fibres and resin.

5.2. Influential Tacking Parameter Study

This section describes the study to define the influence of the vibrational amplitude, continuous tacking pressure and the tape laying velocity to the Ultrasonic Tacking (UST) process. Relations are defined based on the measured peel strength using the Mandrel Peel (MP) setup described in chapter 4.

5.2.1. Methodology of Experiment

A three predictor Central Composite Design (CCD) model is used for this experiment. The use of Response Surface Methodology (RSM), and in particular the CCD model is motivated in chapter 2. The predictors are the vibrational amplitude, continuous tacking pressure and the tape laying velocity. For the ease of reading the following abbreviations are used; amplitude, pressure and velocity. These parameters are selected because they are variable parameters, meaning that they can be easily adapted in the UST process. Meaning that the aspects learned from this study can easily be implemented in the UST process. Besides, the parameters amplitude, pressure and velocity were of interest in other studies related to conventional Ultrasonic Welding (USW) of Thermoplastic (TP) (composite) materials with promising results [72, 102, 117]. Note that the tape laying velocity corresponds to the welding time for conventional static USW. The bond strength measured with the MP setup is considered the response of the statistical model.

A CCD model with $\alpha = 1$ is selected (depicted in figure 2.21b), meaning that three predictor levels are used for each individual predictor. For CCD models with $\alpha \neq 1$, five levels are required per predictor what results in additional complexity [99, 101]. In such case not only the experimental runs are becoming more complex, greater opportunities arise for possibilities of introducing error sources related to the experimental setup and the process of operation. Furthermore, other α values than one would result in non integer values, which is impossible to input in the Falko ATL. The model includes three centre points, as recommended [101]. In order to obtain accurate data, three replicates are used and are grouped in blocks. To conclude, for each UD tape material, a face-centred CCD is constructed containing eight factorial points (cube/corner points), six axial points and 3 centre points. As already explained with equation 2.12, this results in $N = 3 \cdot (2^3 + 2 \cdot 3 + 3) = 51$ experimental runs for each type of UD tape.

The samples are prepared with the Falko ATL. To increase the ability to measure differences in bond strength when modifying the influential parameters, a double amount of continuous tacks are realized on the samples compared to the tape laying process during production of laminates. After production of the 51 samples of each UD tape material, using the random order as suggested in section 2.4.2 the bond strength of the tacked samples are quantified following the same random order. The measured peel forces are imported in the Minitab software, which is used for statistical analysis of the data. Before conclusions are drawn based on the statistical analysis, the invoked assumptions of the RSM model are validated.

5.2.2. Parameter space of Influential Parameters

The three different levels of each single parameter span the parameter space, depicted in figure 5.5. The different levels are selected such that for the lowest settings the bond is measurable with the current experimental MP setup. For the upper bound, the peel strength plus the friction of the system should not exceed the 50 N force gauge limit. Additionally, during initial peel tests of samples it was found that occasionally the bond strength was too high what resulted in locally ruptured tapes along the fibre direction. The latter means that a different failure mode is present and tested, in other words

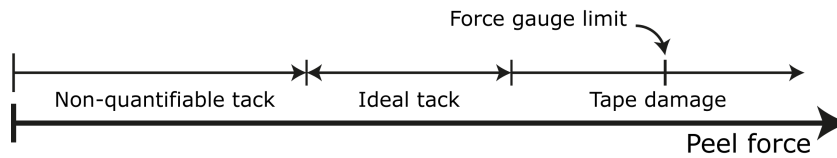


Figure 5.5: Schematic illustration DOE parameter space

	CF-PEEK Teijin			CF-PEKK Solvay			CF-PEKK Toray		
	Low	Medium	High	Low	Medium	High	Low	Medium	High
A [%]	60	80	100	70	85	100	65	80	95
P [%]	40	44	48	12	15	18	19	22	25
V [mm/s]	80	100	120	80	100	120	90	105	120

Table 5.2: Tape dependent parameter space for DOE

the measured force does not accurately represent the peel strength of the tack. These three aspects are considered while determining the parameter space. For each tape analysed a different parameter space is defined for each parameter, this because of the difference in the ability to tack. Based on trial-and-error experiments the low, medium and high parameter levels are determined, presented in table 5.2. It is believed that the pressure required to obtain polymer-polymer contact at the interface of two tape layers is dependent on the amount of TP resin present at the tape interface, and too which extend this resin is accessible for polymer fusion. For example, the relatively high pressure for the Teijin tape parameter space is due to the fibre rich regions at the tape surfaces, refer to figure 3.4a and figure 3.16, meaning that more pressure is required to achieve polymer-polymer contact. The remarkable high pressure required to realize the minimum bond strength threshold for the CF-PEEK parameter space agrees with the minimal measured bond line length at $P = 17\%$, presented in figure 5.3.

5.2.3. Validation of Statistical Model Assumptions

Before using the results of the statistical model, the invoked regression assumptions are validated. Normality, independence of residuals and homoscedasticity should be checked for. The graphs used for checking of these assumptions are provided in figure 5.6 - figure 5.8.

CF-PEEK Teijin DOE

As shown in figure 5.6a, a normal distribution is ensured for this specific DOE since the data points roughly follow the linear red line, except for one outlier. Based on figure 5.6b it can be concluded that no pattern in the residual distribution is observed, meaning that the the assumption related to the independence of residuals holds. According to figure 5.6c the residuals tend to increase as the fitted value increases. As explained in section 2.4.2, the null hypothesis of the Levene's test can be accepted when $p > 0.05$ what means that all variances can be considered equal and homoscedasticity is ensured. In this research the Levene's test is favoured compared to the visual approach. The probability values of the peel force versus amplitude, pressure and velocity are 0.171, 0.106 and 0.051 respectively. Concluding, the data shows homoscedasticity.

CF-PEKK Solvay DOE

Normality is ensured for the DOE performed for the CF-PEKK Solvay UD tape as presented in figure 5.7a. No pattern is observed in the residuals with respect to the observation order (figure 5.7b), meaning that the independence of residuals assumption holds. The Levene's probability values using the same aforementioned order are 0.063, 0.174 and 0.213. All p -values are larger than the probability of 5% meaning that homoscedasticity is ensured.

CF-PEKK Toray DOE

According to figure 5.8a, normality is ensured for the presented data points. Furthermore, dependence of residuals was not found as presented in figure 5.8b. Compared to the other two Versus fits graphs,

figure 5.8c shows the most deviation in residuals upon increase of the fitted value. The latter is defined as a funnel shaped pattern [99, 101]. This is also evident from the Levene's test probability values which are 0.014, 0.000 and 0.135 for the peel force versus amplitude, pressure and velocity respectively. The latter emphasizes that a data transformation on the response of this data set is required.

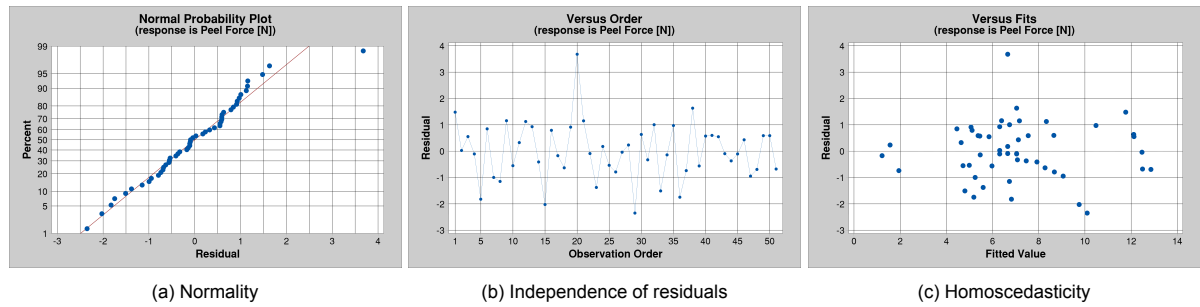


Figure 5.6: Validation of the normality, independence of residuals and homoscedasticity assumptions of CF-PEKK Teijin DOE data

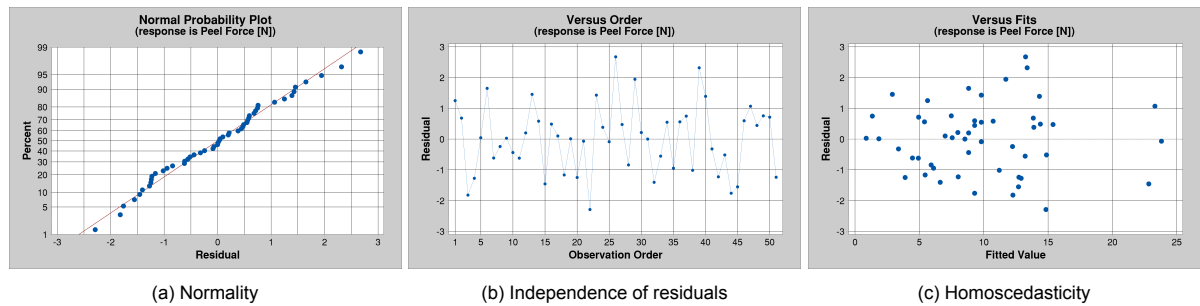


Figure 5.7: Validation of the normality, independence of residuals and homoscedasticity assumptions of CF-PEKK Solvay DOE data

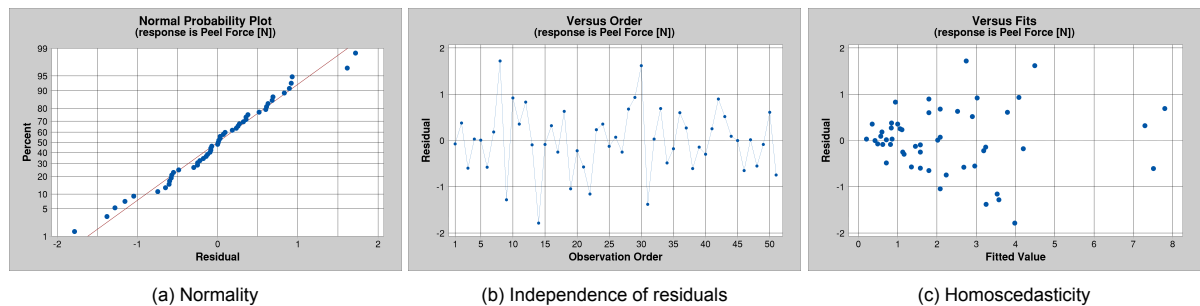


Figure 5.8: Validation of the normality, independence of residuals and homoscedasticity assumptions of CF-PEKK Toray DOE data

5.2.4. The Application of Data Transformation

The measured response data of the Toray CF-PEKK DOE requires a data transformation since it does not comply with the assumptions specified. Figure 5.8c shows that the residuals have the tendency to increase with increasing fitted value. As already mentioned in section 2.4.2, this type of residual behaviour favours a log transform [105, 109]. The data transformation

$$y_i^* = \log(y_i + 1) \quad (5.1)$$

is applied to the raw peel force data presented in appendix C. The data transformation function of $\log(y_i)$ was found not suitable because this resulted in negative peel forces, which is physically impossible [100]. After applying the data transformation the same statistical analysis was performed, resulting

in the graphs provided in figure 5.9. Comparing figure 5.8c with figure 5.9c it can be concluded that the data transformation was effective. The Levene’s probability values for the peel force versus amplitude, pressure and velocity are 0.272, 0.110 and 0.587 respectively. The transformed data is used for further statistical analysis. Nevertheless, the results of the non transformed data set are compared with the results statistical model containing the transformed peel force values. This to ensure that no erroneous conclusions are drawn because of the data transformation.

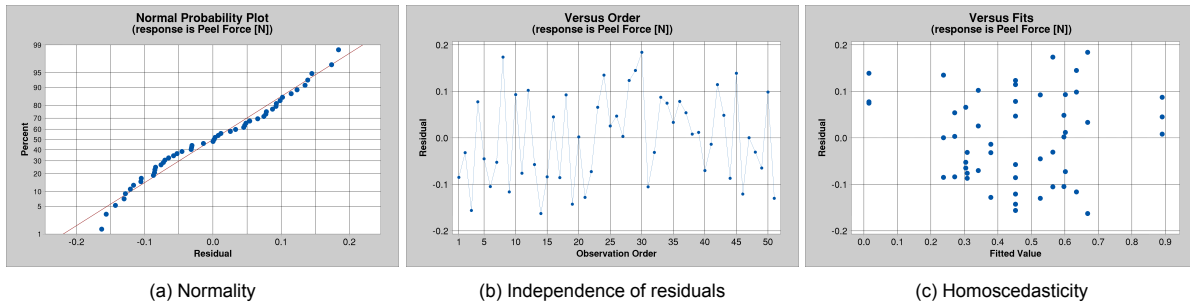


Figure 5.9: Validation of the normality, independence of residuals and homoscedasticity assumptions of transformed CF-PEKK Toray DOE data

5.2.5. Results and Discussion

The full Analysis of Variance (ANOVA) tables of all three tapes analysed are provided in appendix D. For all three DOE there are sufficient Degree(s) of Freedom (DF) for the error estimation, $N - C = 51 - 12 = 39$. The lack of fit p -values are insignificant (> 0.05) meaning that no lack of fit is observed.

The ANOVA presents that all three predictors, amplitude, pressure and velocity have a significant influence to the response of the model. This is stated because the p -values exceed the defined significance level of 5%. Additionally, a strong evidence against the null hypothesis (no interaction between predictor and response) is present as the p -values are ≤ 0.001 . The other sources included in the second order RSM model vary in their significance, in general it can be stated that the squared and two-way interaction terms have little to no influence to the bond strength of the tacked samples. The percentage contribution calculated with equation 2.21 per significant source for each DOE are presented in table 5.3 - table 5.5. Note that the contributions of the insignificant terms which are included in the model are not presented, it cannot be concluded that these specific terms are associated to the model response.

CF-PEEK Teijin	
Source	Contribution [%]
A	47.35
P	4.49
V	27.23
A*A	1.84
P*P	N/A
V*V	N/A
A*P	N/A
A*V	N/A
P*V	N/A

Table 5.3: Contribution of model terms to the response - CF-PEEK Teijin (A=Amplitude, P=Pressure, V=Velocity)

CF-PEKK Solvay	
Source	Contribution [%]
A	29.13
P	47.62
V	14.77
A*A	N/A
P*P	N/A
V*V	N/A
A*P	0.47
A*V	1.02
P*V	1.19

Table 5.4: Contribution of model terms to the response - CF-PEKK Solvay (A=Amplitude, P=Pressure, V=Velocity)

CF-PEKK Toray	
Source	Contribution [%]
A	25.73
P	40.77
V	15.24
A*A	N/A
P*P	N/A
V*V	N/A
A*P	N/A
A*V	N/A
P*V	N/A

Table 5.5: Contribution of model terms to the response - CF-PEKK Toray (A=Amplitude, P=Pressure, V=Velocity)

Described in section 2.4.2 are parameters providing the model summary, which are for each DOE calculated in Minitab and presented in table 5.6. The standard deviation is a parameter relative to the mean of the measurements [100]. Due to slightly different tuning of the parameter space, the

	S [N]	R-sq [%]	R-sq(adj) [%]	R-sq(pred) [%]
CF-PEEK Teijin	1.21	86.10	82.18	77.89
CF-PEKK Solvay	1.26	94.25	94.25	92.16
CF-PEKK Toray	0.25	85.65	81.60	75.75

Table 5.6: Model summaries of PEEK and both PEKK tapes DOE

mean of the measurements of the CF-PEKK Toray DOE is relatively low (back transformation from $y_i^* = \text{Log}(y_i + 1)$ is considered). Therefore, based on the S -value it cannot be concluded that the Toray tape model is more accurate in representing the actual data compared to the other DOE. However, R-squared (R-sq) can be used for this. Roughly 85% of the variance in the response can be explained by the predictors included in the model for the Teijin and Toray tape whereas the statistical model used for the Solvay tape is slightly more accurate (94.25%). The R-squared adjusted values are added for completeness but are not important for this research project since all three models contain three predictors. In agreement with the R-sq values, the predictive capabilities of the Solvay tape model are the highest based on the calculated R-squared(pred) values. In other words, the model is quite accurate when the response of predictor combinations other than included in the DOE are predicted. Based on the model summaries provided, it is concluded that the statistical model used for the Solvay tape is most accurate. Nevertheless, the accuracies of the other two models are still reasonable meaning that the results can be used with confidence.

The (second order) regression equations to calculate the predicted bond strength based on amplitude (A), pressure (P) and velocity (V) parameters provided by Minitab are presented below;

CF-PEEK Teijin:

$$F_{peel} = 17.6 - 0.387 \cdot A + 0.262 \cdot P - 0.129 \cdot V + 0.004 \cdot A^2 \quad (5.2)$$

CF-PEKK Solvay:

$$F_{peel} = -43.0 + 0.500 \cdot A + 2.948 \cdot P - 0.132 \cdot V + 0.002 \cdot A \cdot P - 0.003 \cdot A \cdot V - 0.014 \cdot P \cdot V \quad (5.3)$$

CF-PEKK Toray:

$$F_{peel} = -2.1 + 0.010 \cdot A + 0.061 \cdot P - 0.007 \cdot V \quad (5.4)$$

in which the parameters should be included with engineering units (in %), and not in coded units. Not all nine second order model terms are included in the equations presented, this because several model terms did not show significance with respect to the response. The peel forces calculated with equation 5.4 must be transformed using $10^{F_{peel}} - 1$ to obtain the predicted bond strength in Newtons, this because of the data transformation performed on the Toray DOE peel force measurements.

With use of the regression equations presented above, Minitab provides three-dimensional response surface plots. Each individual graph represents the influence of two predictors to the predicted peel strength, the hold values are selected to be the medium tacking parameters, specified in table 5.2.

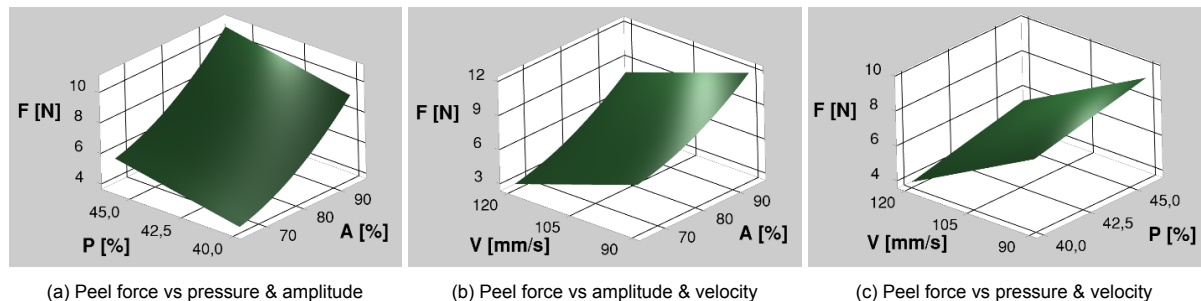


Figure 5.10: Response surfaces showing the relation between predictors (amplitude = A, pressure = P and velocity = V) and response (peel force = F) of CF-PEEK Teijin DOE

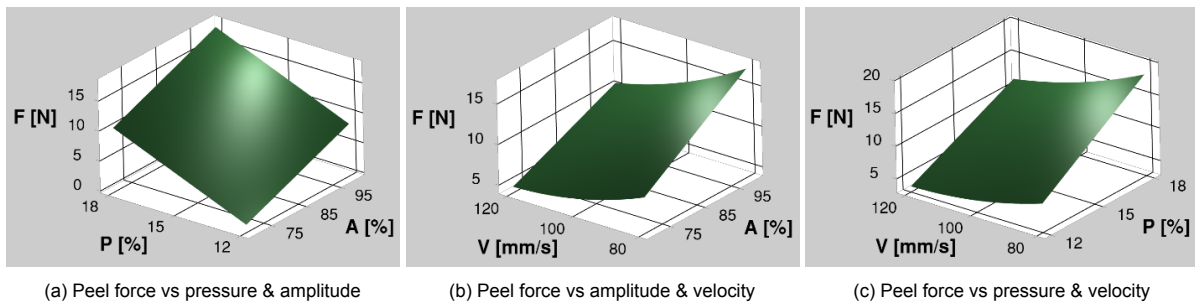


Figure 5.11: Response surfaces showing the relation between predictors (amplitude = A, pressure = P and velocity = V) and response (peel force = F) of CF-PEKK Solvay DOE

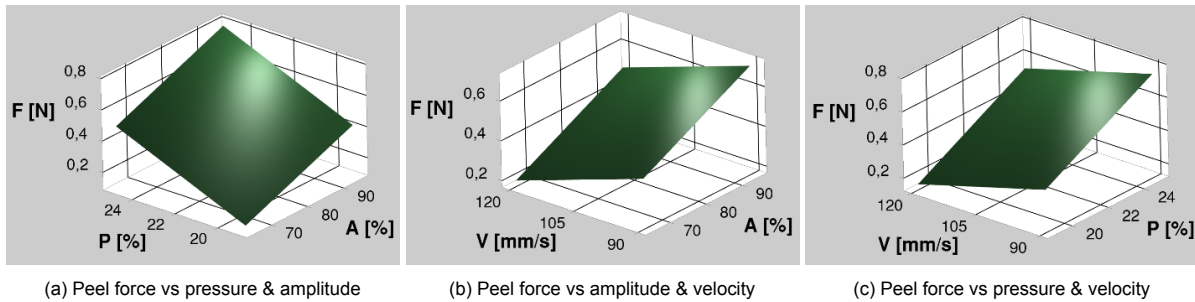


Figure 5.12: Response surfaces showing the relation between predictors (amplitude = A, pressure = P and velocity = V) and response (peel force = F) of CF-PEKK Toray DOE

The response surfaces present little to no curvature, what can be validated by looking at the regression equations provided above. The slope in the response surface of figure 5.10a visualizes what was already presented in table 5.3, the continuous tacking pressure does have limited influence to the bond strength of the Teijin samples whereas the vibrational amplitude does have a major contribution to the bond strength. It is believed that this is related to the fibre rich outer surfaces of the Teijin tape, characterized in chapter 3. Although a high pressure in the parameter space was required for obtaining a bond sufficient strong enough, an increase in pressure does not result in significant more polymer-polymer contact due to the fibre rich regions, emphasizing the low contribution of pressure to the bond strength. Figure 5.10c represents a plane in a three-dimensional space, because the amplitude is hold at a value of 80% meaning that only the linear terms in equation 5.2 are varied for this particular response surface. From this graph it can be concluded that the bond strength of tacked Teijin tapes is rather sensitive to the tape laying velocity.

Each response surface in figure 5.11 shows minor curvature, this because of the two-way interaction terms in equation 5.3. In contrast to the previous mentioned DOE results, the continuous tacking pressure heavily contributes to the bond strength of the tacked CF-PEKK Solvay samples. It is reasonable to assume that an increase of pressure results in more polymer-polymer contact at the interface, especially when considering the resin rich surfaces of this specific type of UD tape. The difference in contribution by vibrational amplitude between the Teijin and Solvay DOE as presented before is also visible while comparing the slopes of the response surfaces along the amplitude axis in figure 5.10a and figure 5.11a. Furthermore, the PEKK tape from Solvay is less sensitive to the tape laying velocity compared to the Teijin tape.

The statistical model used for the CF-PEKK Toray tape lacks any non-linear term, what is clearly visible in the response surfaces. Again the pressure is the most important predictor, with similar behaviour compared to the other PEKK tape.

5.2.6. Concluding Remarks

Based on the *R*-squared values it is clear that the model used to predict the bond strength for the Solvay tapes is most accurate. Before performing the experimental test of the DOE it was believed that the

rather constant FRR distribution through the thickness of the Toray tape, in combination with the results presented in section 5.1.4 would result in the most accurate statistical model. However, the low error of 4.48% could originate from the fact that tacked Solvay tapes are analysed with the MP setup, testing purely the polymer-polymer interface instead of testing other possible (fibre) interactions. For example, the effect of fibre bridging across the interface of tapes having fibre rich surfaces, such as the tapes from Teijin and Toray.

Based on the statistical analysis results in combination with the response surfaces presented in figure 5.11 and figure 5.12 it is stated that the influence of predictors to the bond strength is rather similar for both CF-PEKK tapes. According to the results presented in table 5.4 and table 5.5 increasing the continuous tacking pressure does have the highest potential for realising a strong bond. It is concluded that the amount of TP resin present at the interface, in combination with the accessibility of underlying resin reflects on the contribution of the pressure to the bond strength. However, it was observed throughout the experiments of both DOE that increasing the pressure outside the ideal tack parameter space (figure 5.1) resulted in damaging of the tape. This local damage of the tape samples could lead to measuring the force required to rupture the tape instead of testing the actual bond on the peel strength. Eventhough the goal was not to rupture the tape during the MP experiments this could not always be prevented, especially at predictor combinations involving high pressure levels. This means that it is high likely that the pressure is incorrectly stated as the most contributing parameter to the bond strength. Considering the latter in combination with the fact that excessive damaging of the tapes during the UST process is not desired, it is concluded that the vibrational amplitude is the predictor with the highest potential for process optimization for the PEEK and both PEKK tapes. Besides, increasing the amplitude shows the highest potential for the CF-PEEK tape which is the most challenging tape to process.

5.3. Effect of UD Tape Microstructure on Bond Strength Variation

This section is dedicated to determining the relationship between the UD tape microstructure and variation in the obtained bond strength. Section 5.3.1 describes the methodology of this experiment. Section 5.3.2 provides and discusses the results. Section 5.3.3 concludes on the relation between the microstructure and the measured bond strength.

5.3.1. Methodology of Experiment

In section 5.1 the length of the established bonds was related to the microstructure of the corresponding tape. The current experiment focusses on the variation in bond strength, and relates this to the characterized microstructure. The variation in BLL, schematic visualized in figure 5.3, is determined over the three micrographs analysed and calculated using

$$R_{BLL} = \frac{\sigma(BLL_1, BLL_2, BLL_3)}{\frac{1}{3} \sum_{i=1}^3 BLL_i} \quad (5.5)$$

meaning that the variation in BLL is divided by the mean of BLL. The ratio corrects for differences in mean BLL, enabling to perform an accurate comparison between the three tapes analysed. The peel curves obtained using the MP setup of samples from the influential parameter study (section 5.2) are analysed for the current experiment. The variation in peel curves of the samples realised with the 'low' and 'high' tacking parameters, specified in table 5.2, is determined. The equation to determine the Peel Force (PF) ratio is

$$R_{PF} = \frac{\sigma(PF_{x=50mm \rightarrow 200mm})}{\frac{1}{N} \sum PF_{x=50mm \rightarrow 200mm}} \quad (5.6)$$

where N is the number of data points between $x = 50\text{mm}$ and $x = 200\text{mm}$. Identical to R_{BLL} , R_{PF} is also corrected for different mean values between the PEEK and PEKK tapes analysed. Two R_{PF} ratios are calculated for each individual type of UD tape, one for samples tacked with 'low' settings, one for the 'high' settings samples. The trend observed in the R_{BLL} ratios is compared with the trend of the peel force variation ratios, and eventually related to the FRR distributions.

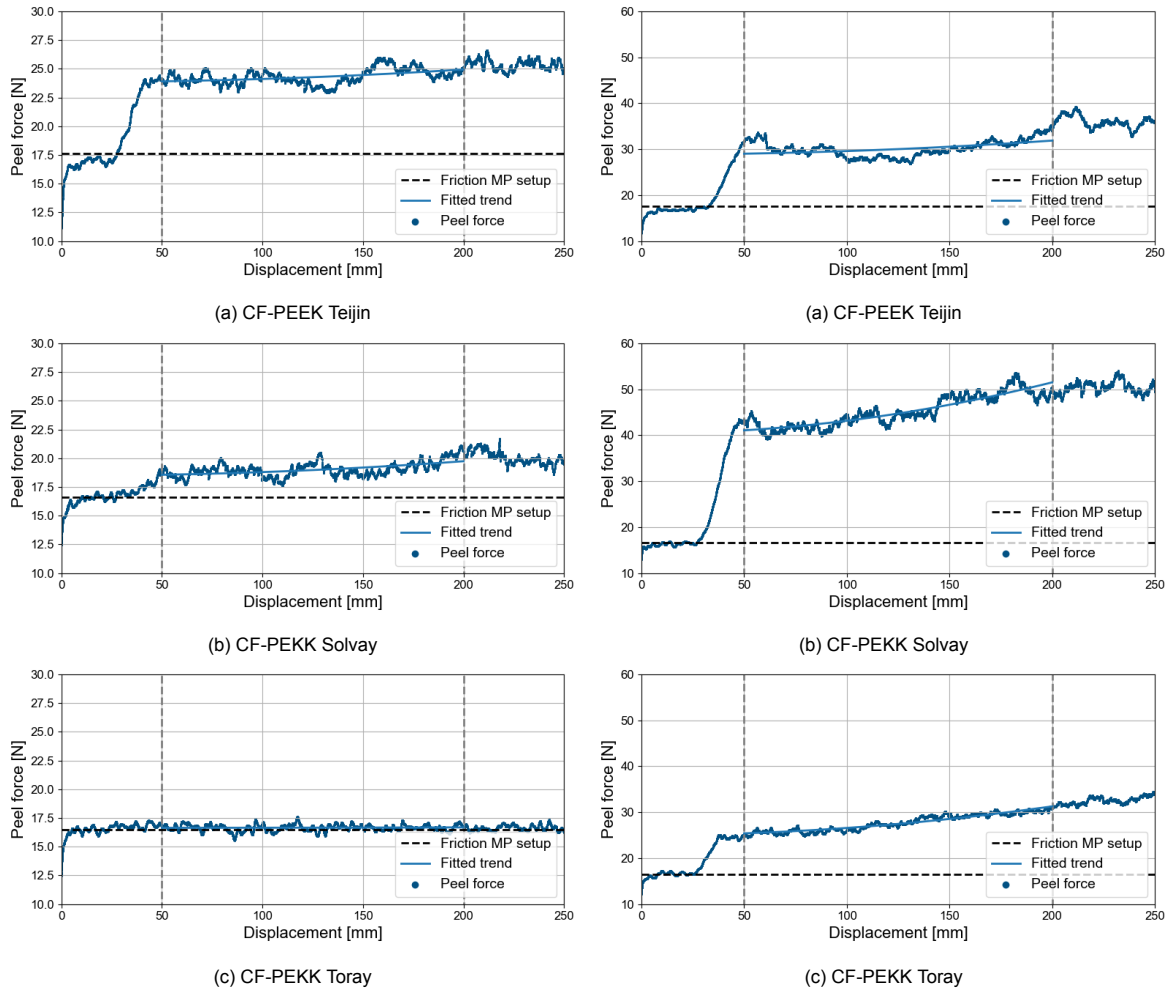


Figure 5.13: Peel force graphs of PEEK and PEKK 'low' tacking parameter settings samples
 Figure 5.14: Peel force graphs of PEEK and PEKK 'high' tacking parameter settings samples

5.3.2. Results and Discussion

The R_{BLL} ratios presented in table 5.7 emphasize that the variation in measured BLL is the largest for tacked Teijin tape, whereas the variation is the smallest for the Toray tape. Figure 5.13 and figure 5.14 present one of the obtained peel curves of the samples prepared using the 'low' and 'high' settings, respectively.

	R_{BLL}	$R_{PF (low)}$	$R_{PF (high)}$
CF-PEEK Teijin	0.192	0.040	0.074
CF-PEKK Solvay	0.164	0.037	0.083
CF-PEKK Toray	0.098	0.017	0.069

Table 5.7: Bond Line Length (R_{BLL}) and Peel Force (R_{PF}) variation ratios of the CF-PEEK tape and both CF-PEKK tapes

The analysis includes three peel curves per set of tacking parameters for each tape, this because the DOE presented in section 5.2 included three replicates. The calculated $R_{PF(low)}$ and $R_{PF(high)}$ for each type of UD tape are presented in table 5.7. Remarkable is that the same decreasing order is observed for the 'low' samples, starting at the Teijin tape. The CF-PEKK tape manufactured by Toray is

characterized by a quite constant FRR distribution with minor variation (see figure 3.18), which is also visible in the relatively low variation ratios $R_{PF(low)}$ (and $R_{PF(high)}$). The approximately similar $R_{PF(low)}$ of the Teijin and Solvay peel curves emphasize that more variation is present with respect to the tape from Toray. The latter can be agreed upon by considering the FRR distributions (section 3.4) in combination with the BLL comparison (section 5.1). Therefore, the degree of consistency in BLL and FRR relates to the amount of variation observed in the peel curves for the 'low' samples. The observed trend does not hold for the variation in peel curves of the 'high' samples. However, the Toray $R_{PF(high)}$ remains the lowest of the three ratios. As already mentioned before, fibre bridging and fibre pull-out occasionally occurred during the MP assessment of samples realized using relatively high tacking parameters. The latter implies that the $R_{PF(high)}$ ratios may be erroneous due to interactions other than failure of the TP polymer bonds, which possibly can introduce much variation in the measured peel strength.

5.3.3. Concluding Remarks

The relation between the consistency in FRR distribution, the BLL and the variation observed in bond strength, R_{PF} is summarized using the visualization presented in figure 5.15. The magnitude of R_{BLL} can provide knowledge about the degree of variation in R_{PF} , and vice versa. For example, a high R_{PF} implies that much variation in BLL is present. It should be noted that this only holds for samples with limited tape damages. Besides, the variation in microstructure of an UD tape can be qualitatively described by the R_{PF} ratio. A low R_{PF} relates to a microstructure with minor variation, similar to the FRR distribution of the Toray tape.

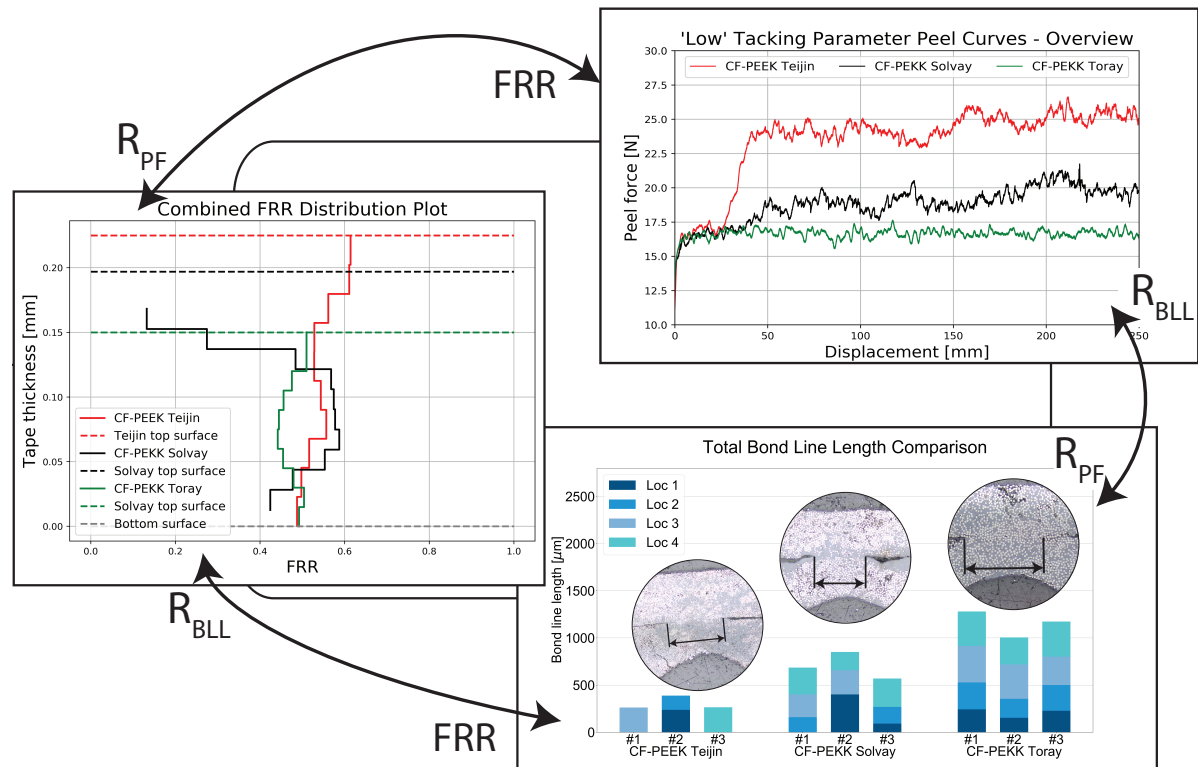


Figure 5.15: Visualization of relations between FRR, R_{BLL} and R_{PF}

6

Optimization of Ultrasonic Tacking Technology

Section 6.1 describes the implementation of a high gain booster and presents the effect of an increased vibrational amplitude on the bond strength. Process optimization in terms of an increased tape laying velocity is presented in section 6.2.

6.1. Influence of Increased Vibrational Amplitude on Bond Strength

Section 6.1.1 describes the experiment methodology to study the influence of an increased vibrational amplitude on the bond strength of tacked samples. Section 6.1.2 describes the implementation of the high gain booster and motivates the tacking parameters utilized for the tacked samples. Section 6.1.3 presents the results and discussion. Concluding remarks can be found in section 6.1.4.

6.1.1. Methodology of Experiment

It was concluded in section 5.2 that increasing the vibrational amplitude does have the highest potential for obtaining a stronger bond, especially for the most challenging tape to tack (Carbon Fibre (CF)-Polyetheretherketone (PEEK) Teijin). Meaning that with a higher amplitude the velocity can potentially be increased to obtain the same bond strength, what results in process optimization.

The vibrational amplitude of the ultrasonic stack is increased by implementing a booster with a higher gain factor ¹. It is unknown if the current sonotrode is able to resist the higher amplitudes, and thus larger stresses. Therefore it was decided to implement a different sonotrode. Potentially sacrificing this sonotrode was desired compared to sacrificing the production sonotrode. The change of sonotrode could introduce small changes in the bond strength and the required power from the ultrasonic generator. Variations in these aspects should be clear prior to starting the analysis of implementing a different booster in the Ultrasonic Tacking (UST) stack. After implementation of the high gain booster the percentage of vibrational amplitude is increased with steps of 10% starting from the amplitude level equal to an amplitude of 100% with the low gain booster. Similar to all other experiments performed in this research project, three samples are prepared to increase the reliability of the experiment. The bond strength of the samples is tested using the Mandrel Peel (MP) setup. The generated power required to obtain the defined vibrational amplitude is logged by the Falko Automated Tape Laying (ATL), this data is eventually analysed using a Python script. Power graphs, and especially the average power consumption during continuous tacking provides understanding of the relation between an amplitude increase and the efficiency of the process.

6.1.2. Modification of Ultrasonic Tacking Stack

The sonotrode used for analysing the effect of an increased vibrational amplitude, referred to as sonotrode B, does have a different gain factor compared to the current production sonotrode (sonotrode A).The

¹Please note the qualitative description because of confidentiality reasons

gain of the high gain booster (Booster H) is twice the gain from the current production booster (Booster L). Furthermore, Sonotrode B does have fewer points of contact with the Unidirectional (UD) tape compared to Sonotrode A. The configurations of UST stack are schematically depicted in figure 6.1. Three samples were prepared using identical settings with each ultrasonic stack, the gain difference in booster and sonotrode were considered in the selected amplitude percentage. The bond strengths and the power generated are presented in figure 6.2 and figure 6.3 respectively. Besides a slightly higher amount of variation, the required power to achieve the vibrational amplitude is similar. This agrees with what was expected since the amplitude in microns for both UST stack configurations is identical. A decrease in bond strength was observed using Sonotrode B compared to Sonotrode A. This can be explained by a decrease in contact area while utilising sonotrode B. Concluded from the graphs is that the change of sonotrode does not affect the required power consumption whereas the bond strength is decreased, due to the reduced points of contact.

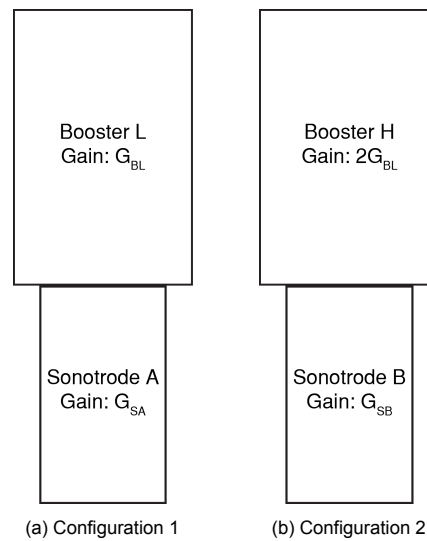


Figure 6.1: Ultrasonic stack configurations used for booster implementation

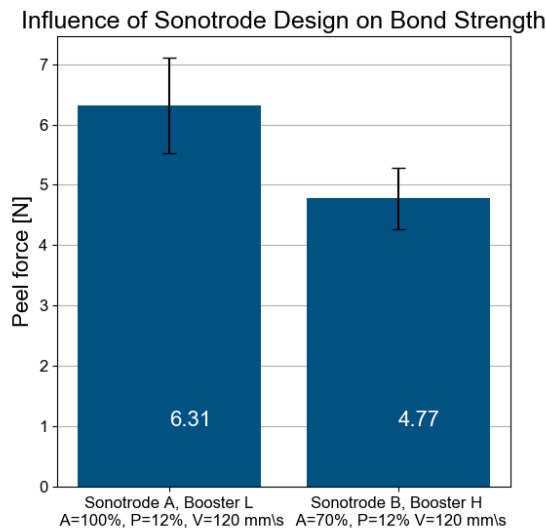


Figure 6.2: Bond strength differences of samples from different ultrasonic stack configurations

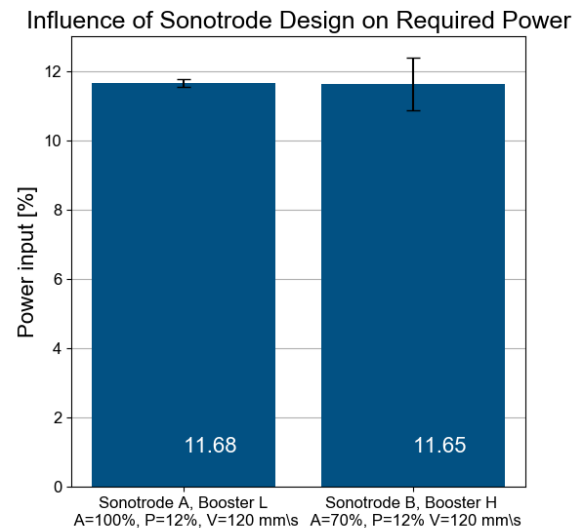


Figure 6.3: Required power differences of samples from different ultrasonic stack configurations

6.1.3. Results and Discussion

To determine the influence of an increased vibrational amplitude on the bond strength samples are prepared with configuration 2 at amplitudes of 70% (100% of configuration 1), 80%, 90% and 100%. The measured peel forces using the MP setup represented using bar plots are presented in appendix E, figure E.1 - figure E.3. The last bar of each figure should be ignored, this bar corresponds to the results of the experiment described in section 6.2.

A clear trend is visible in the graphs presented showing an increase of bond strength upon an increase of vibrational amplitude, what is in agreement with findings from literature [7, 72]. An increase of amplitude results in the generation of more heat, originated from larger strain oscillations (explained in section 2.2.2). This increase of generated heat results in a larger locally heated zone during tacking, resulting in more fusion of polymer chains across the interface. Consequently, resulting in a stronger bond.

Three fitted line plots are presented in figure 6.4a - figure 6.4c, based on the Design of Experiment(s) (DOE) data of chapter 5. For each of the three datasets a quadratic regression fit (with very little curvature) most accurately represents the data presented using the three predictor levels, this was determined based on the R -squared value of the proposed model. A second order fit was also applied to the results obtained from the samples created with an increased vibrational amplitude, this trend is presented as the dashed line in figure E.1 - figure E.3. The peel forces extracted from the fitted trend lines for both, the DOE and the booster implementation experiment are summarized in table 6.1. Note that for the DOE 'Sonotrode A' and 'Booster L' are used whereas 'Sonotrode B' with 'Booster H' is the configuration used for the booster implementation results. The percentage difference of the vibrational amplitude (A) and peel force (F) is used to calculate the 'Ratio'. This ratio characterizes the increase of peel strength in relation to the increase of amplitude. Based on the ratio calculated for the Solvay DOE it can be stated that the bond strength increases the fastest with an amplitude increase, compared to the other two tapes. For the booster implementation part of table 6.1, where 70% corresponds to 100% in the DOE part the same behaviour is observed when looking at the ascending/descending order of calculated ratios. However, the increasing peel strength becomes less sensitive with an increase of amplitude, since the ratios are lower.

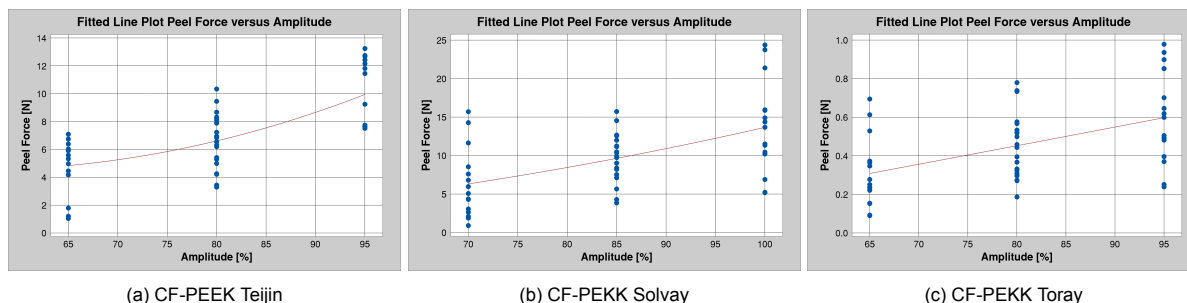


Figure 6.4: Fitted line plots of vibrational amplitude versus bond strength for each UD tape analysed

		Design of experiments				Booster implementation			
		Initial	Final	Δ	Ratio	Initial	Final	Δ	Ratio
CF-PEEK - Teijin	A [%]	65	95	46.2%	2.28	70	100	42.9%	0.97
	F [N]	4.85	9.95	105.4%		3.14	4.44	41.4%	
CF-PEKK - Solvay	A [%]	70	100	42.7%	2.71	70	100	42.9%	1.74
	F [N]	6.32	13.66	116.2%		4.70	8.21	74.6%	
CF-PEKK - Toray	A [%]	65	95	46.2%	2.03	70	100	42.9%	0.78
	F [N]	0.31	0.60	93.7%		1.87	2.50	33.2%	

Table 6.1: Peel strength increase with increase of amplitude: DOE vs booster implementation

The corresponding power required for the prepared samples are visualized in figure E.4 - figure E.6. Again, only the first four bars should be considered. From the graphs it is clear that the required power

increases as the vibrational amplitude increases, which fully agrees with other experiments presented in literature [9]. The mean values vary between the different UD tapes, considering the same amplitude level with roughly similar pressure and velocity. It is observed that the mean values of the Teijin tape are higher compared to the Toray tape, and especially with respect to the Solvay tape. It is interesting to note that the ease of achieving the defined amplitude agrees with the difference in fibre and resin rich outer surfaces of the UD tape. For example, the fibre rich regions at the surface of the Teijin tape act as rather stiff blocks meaning that the sonotrode in contact with this surface requires more effort to achieve the defined vibrational amplitude.

6.1.4. Concluding Remarks

Based on the ratios presented, expressing the bond strength increase over the increase of amplitude, it is high likely to assume that an optimum is present for the relation peel force versus amplitude, which is in agreement with literature [18]. An optimum is expected because the defined ratio decreased when comparing the DOE results (up to original 100%) with the booster implementation results (above original 100%). By critically reviewing the calculated ratios, it was not expected that the calculated ratios of the Solvay tape for both experiments would be the highest. It was expected that the peel strength of tacked CF-PEEK samples would be most sensitive to an amplitude increase. This because the amplitude for this tape contributes 47% to the peel strength, which is much more than the 29% and 25% for the Solvay and Toray tape respectively. However, this can be explained by considering the decrease in contact points for Sonotrode B and the sensitive nature of the Teijin tape to bond locations, emphasized by the R_{BLL} ratios presented in table 5.7.

6.2. Validation of Booster Implementation

The methodology of the validation experiment is presented in section 6.2.1, followed by the results in section 6.2.2. Section 6.2.3 motivates why the implementation of the booster is validated.

6.2.1. Methodology of Experiment

Based on the experiment presented in the previous section it is concluded that an increase in vibrational amplitude shows a positive effect on the bond strength of the tacked UD tapes. For process optimization it is interesting to see the effect of the bond strength when the velocity of the Falko ATL is increased, while utilising the high gain booster. Samples are prepared using the high gain booster with 100% amplitude with an increased velocity. The bond strength of the corresponding samples are determined using the MP setup, and are compared with the earlier presented peel force results of the samples prepared using an amplitude of 70%. This because 70% corresponds to the maximum vibrational amplitude in the current production setup (Sonotrode A with Booster L). Because the influence of the tape laying velocity at high amplitudes is not completely clear, the increase in velocity is according to

$$V_{high} = \frac{A_{final}}{A_{initial}} \cdot V_{low} = \frac{100\%}{70\%} \cdot V_{low} = 1.43 \cdot V_{low} \quad (6.1)$$

meaning that the velocity is increased with 43%. To purely see the effect of an increased velocity on the bond strength, it is decided to keep the continuous tacking pressure constant. Three identical tacked samples are realized for each UD tape material for increased accuracy.

6.2.2. Results and Discussion

The last (fifth) bar in the graphs of appendix E represents the measured peel forces and required power of the samples prepared with V_{high} . The measured peel forces of the high velocity samples show a clear decrease compared to results obtained at lower velocities with a similar amplitude. This can easily be substantiated by the fact that less energy is dissipated at a specific location, meaning that less fusion of polymer chains can take place. Consequently resulting in a weaker bond between both UD tapes. The peel force results are summarized in table 6.2. The bond strengths in combination with visual observations of the tapes realized with a velocity increase of 43% show promising results. At maximum a reduction of the original bond strength of 18.46% was observed for the Teijin tape samples. This is in agreement with the results presented in table 5.3 - table 5.5, showing that the Teijin tape is most sensitive to velocity changes. The minor influence of velocity to the bond strength of the Solvay tape is also evident from the lowest drop in the observed bond strength.

The required power to achieve the predefined vibrational amplitude corresponding to the tacked V_{high} samples show inconsistent behaviour, visualized in appendix E. The required power for the Teijin and Toray tape are roughly identical to the the power required to realize the samples at V_{low} with an amplitude of 100%. However, the required power for the Solvay tape increased tremendously increased. In other words, it becomes more difficult to realize the amplitude of 100% at high velocities. Although a straightforward explanation cannot be given, it could be due to the fact that the surface of the Solvay tape shows major surface waviness.

	V_{low}	V_{high}	Δ
CF-PEEK Teijin	3.14	2.56	-18.46 %
CF-PEKK Solvay	4.70	4.30	-8.55 %
CF-PEKK Toray	1.87	1.66	-11.34 %

Table 6.2: Differences in measured peel force with 43% velocity increase

6.2.3. Concluding Remarks

The bond strengths of the samples realized with an increased velocity are promising. Based on experience, an increase of tape laying velocity is generally accompanied with an increase of continuous tacking pressure. However, the pressure was kept constant during throughout this experiment. Meaning that high likely higher bond strengths than those presented in table 6.2 can be realized. Nevertheless, the implementation of a high gain booster did show its potential for process optimization in terms of tape laying velocity.

Conclusions and Recommendations

Variations in the ability to tack Unidirectional (UD) tapes, consisting of Carbon Fibre (CF) with Polyetheretherketone (PEEK) and Polyetherketoneketone (PEKK) Thermoplastic (TP) resins were observed at Boikon utilising their Ultrasonic Tacking (UST) technology. A thorough understanding of the origin of the challenges encountered contribute to the possibilities of process optimization. The following main research question is formulated:

'Which UST parameters should be altered, and in which manner to increase the tape laying speed, while preserving the tacking quality of carbon fibre unidirectional tapes containing PEKK and PEEK polymers?'

which is answered in section 7.1. Recommendations for further research are proposed in section 7.2.

7.1. Conclusions

The microstructure of the three relevant UD tapes are dissimilar, and each tape can be characterized by distinct features. Apparently identical tapes are utterly different on microscopic level. The analytical model developed to quantitatively characterize UD tapes utilises the Voronoi Tessellation algorithm. The area of a Voronoi cell, in combination with the fibre cross-sectional area effectively describes the local Fibre-Resin Ratio (FRR). Characterizing straight tapes is most accurate using the developed through thickness FRR distribution, whereas the localized boundary analysis is preferred for quantifying and comparing tapes with surface waviness. The CF-PEEK Teijin tape is characterized by a fibre rich upper surface with much fibre clustering and variation in the distribution of fibres present at the total cross-section. The Solvay CF-PEKK tape has irregular shaped resin rich outer surfaces, especially the top surface, with respect to the tape mid-section. Large variations in FRR are observed for this tape. The CF-PEKK tape manufactured by Toray has the most constant FRR distribution, and shows little variation in FRR.

Differences in the ability to tack the tapes from Teijin, Solvay and Toray are experienced by Boikon. Considering that the relevant material properties for UST of PEEK and PEKK are roughly identical (refer to table 2.1), it is concluded that the microstructure has a major influence on the ability to ultrasonically tack a tape. The Teijin tape is most challenging to tack, due to the fibre rich outer surfaces. Meaning that little resin is present at the surface. The large amount of variation in the FRR distribution of this tape is also visible in the inconsistency in the measured Bond Line Length (BLL). Viscoelastic heating at the interface is limited due to the relatively difficult accessible TP resin. Furthermore, little frictional heating is expected because of the straight tape surface. The tape of Solvay is relatively easy to tack as a result of much matrix accumulation at the interface. The large variations in FRR for this tape are also present in the inconsistencies of BLL. Viscoelastic heating at the interface is more likely for the Solvay tape because of the resin rich outer surface. Frictional heating is considered an important heating mechanism because of the surface waviness, what acts as surface asperities. This combination of heating mechanisms enhances the heating of TP polymer and eventually the fusion of polymer chains across the interface. The CF-PEKK Toray tape is more challenging to tack compared to the Solvay

PEKK tape, this because of the rather fibre rich interface. Although the slight challenging tacking ability, very little variation is observed in BLL, which is in agreement with the consistent microstructure of the Toray tape. It is concluded that for a consistent BLL, a tape showing little variation in FRR at the surface is preferred compared to a tape with much variation in FRR, even if this tape is slightly fibre rich at the interface.

The sensitivity to a change of the tacking parameters amplitude, pressure and velocity to the bond strength depends on the tape microstructure, and is therefore different for each type of tape. The Response Surface Methodology (RSM) type of Design of Experiment(s) (DOE) statistically derived the contributions to the bond strength, for each of the three aforementioned tacking parameters. Bond strengths of the tacked samples are quantified based on the peel curves, obtained utilising the developed Mandrel Peel (MP) test setup. The degree of variation observed in peel force of the tacked samples is in agreement with the variations in FRR of the three UD tapes. Meaning that the variation in microstructure can qualitatively be described by the amount of peel force variation present in the peel curves. The selected face-centred Central Composite Design (CCD) type of RSM contains three predictors at three levels and involves one response. The tacking parameter settings used to span the three level parameter space are inherently linked to the tape characteristics. For example, the parameter space of the Solvay tape contains relatively low pressure levels. This because the TP resin is easily accessible, and little pressure is required for polymer-polymer contact at the interface. The opposite holds for the Teijin parameter space, high pressure levels are necessary due to the fibre rich outer surfaces.

The response surfaces derived from the RSM, utilising a CCD model, are used to indicate that the tacking pressure has the highest potential for process optimization of tacking CF-PEKK tapes. An increased tacking pressure results in significant higher bond strengths for each of the three UD tapes. However, a relatively high continuous tacking pressure can damage the tape which is undesirable. An increase of vibrational amplitude significantly contributes to a stronger bond, with varying contribution for the three relevant tapes. Even further increasing the vibrational amplitude, by implementing a high gain booster, resulted in stronger bonds. This validates the significant contribution of amplitude to the bond strength, predicted using RSM. Process optimization of UST in terms of a 43% increased tape laying velocity is possible by increasing the amplitude, considering that a similar bond strength is sufficient.

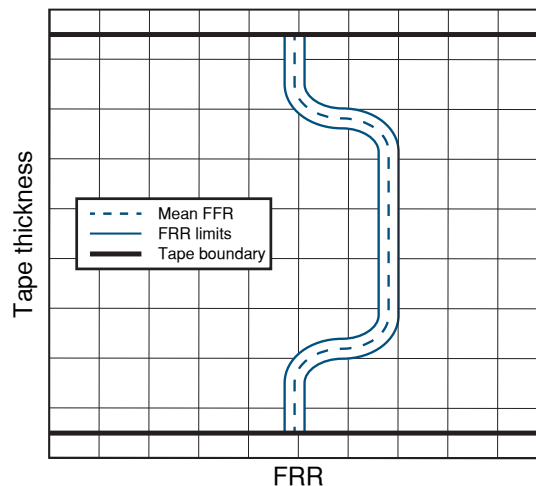


Figure 7.1: Schematic ideal UD tape FRR distribution for UST

Besides an increased vibrational amplitude, the tape laying process can be optimized by changing the microstructure of the UD tapes to the most ideal UD tape for UST, refer to figure 7.1. This tape is characterized by resin rich outer surfaces, whereas the mid-section of the tape is rather fibre rich. This to compensate for the resin rich regions at the outer surfaces. A resin rich interface is favourable for UST as this increases the length over which a bond is established, concluded based on the flipped Solvay tape experiment. The advantage of having a resin rich interface is in agreement with literature related to conventional Ultrasonic Welding (USW), where regularly an Energy Director (ED) is included

at the interface to enhance the welding abilities. A resin rich interface is also efficient in terms of the power required to achieve the pre-defined vibrational amplitude. This is concluded based on the analysed required power graphs corresponding to the tacked Solvay samples. Low variations in FRR are included in figure 7.1 because little to no variation in FRR is favourable for the consistency in BLL, resulting in small variations in peel force.

7.2. Recommendations

For further research related to the microstructural analysis of UD tapes the following is proposed. First of all, implementation of automated tape boundary detection is desired. The current method of detecting the boundary shape is a laborious and time consuming task. With the use of automated detection, more micrographs can be analysed in the same time span what increases the accuracy of the analysis. Initial attempts to detect the boundary of the tape using photo editing software showed promising results. Nevertheless, the automated boundary detection must ensure that the boundary is not defined such that a fibre is located outside the defined boundary. This results in invalid use of the Python script.

According to the micrographs obtained it is clear that fibres do not have a constant circular cross-section. Using a method to individually determine the shape and size of the cross-section would improve the analytical model. A different method to express the data obtained is based on the area disorder property, a number quantifying the dispersion of fibres in composite parts [115, 116, 129]. Adding this property to the analysis is considered effective as in some unique cases the Voronoi tessellation diagram misguidedly describes a perfect dispersed system.

Voids present in the TP resin are not recognized by the analysis, meaning that a void is currently considered as TP resin. This inaccuracy results in a lower FRR due to the additional resin considered in the calculation as part of the Voronoi cell, which actually is entrapped air. The current boundary detection method can also be applied to detect voids, and subtract these from the original image to increase the precision of the FRR distribution.

In case more accurate relations between the predictors and response is desired, it is recommended to use the Box-Behnken type of RSM instead of the CCD. This model is configured such that extreme parameter combinations are not included [105]. This partially removes the challenges encountered while defining the parameter spaces of each predictor. Furthermore, removing the extreme combinations also reduce the possibility of obtaining slightly damaged tapes. This increases the certainty that purely the peel strength of the bond is assessed with the MP setup and that no other fibre-resin interactions influence the peel force measurements. Additionally, a change of sonotrode design is recommended such that a more gradual contact between the sonotrode and the UD tape is realized. This to possibly reduce damaging of the tapes.

The inexplicable required power results obtained after implementation of the high gain booster should be studied in more detail to understand the consequence of an increased vibrational amplitude on the power required. It is also recommended to optimize the continuous tacking pressure in combination with the increased amplitude such that the most optimal configuration is obtained. Additionally, further increasing the vibrational amplitude is recommended to find the optimum amplitude at which the bond strengths stops increasing. This can be realized by implementing an even higher gain booster.

Bibliography

- [1] M. Roux, C. Dransfeld, N. Eguémann, and L. Giger. Processing and recycling of thermoplastic composite fibre/peek aerospace part. In *16th European Conference on Composite Materials*, pages 1–8, Seville, Spain, 2014. URL: https://www.researchgate.net/publication/273575078_Processing_and_recycling_of_thermoplastic_composite_fibrePEEK_aerospace_part.
- [2] M. Kropka, M. Muehlbacher, T. Neumeyer, and V. Altstaedt. From ud-tape to final part – a comprehensive approach towards thermoplastic composites. *Procedia CIRP*, 66(1):96–100, 2017. DOI: 10.1016/j.procir.2017.03.371.
- [3] V. Dhinakaran, K. V. Surendar, M. S. Hasunfur Riyaz, and M. Ravichandran. Review on study of thermosetting and thermoplastic materials in the automated fiber placement process. *Materials Today: Proceedings*, 27(1):812–815, 2020. DOI: 10.1016/j.matpr.2019.12.355.
- [4] H. Li and K. Englund. Recycling of carbon fiber-reinforced thermoplastic composite wastes from the aerospace industry. *Journal of Composite Materials*, 51(1):1265–1273, 2017. DOI: 10.1177/0021998316671796.
- [5] A. Yousefpour, M. Hojjati, and J. Immarigeon. Fusion bonding/welding of thermoplastic composites. *Journal of Thermoplastic Composite Materials*, 17(1):303–341, 2004. DOI: 10.1177/0892705704045187.
- [6] BOIKON B.V. "Thermoplastic Composites Machinery" unpublished.
- [7] A. Benatar and T. G. Gutowski. Ultrasonic welding of peek graphite apc-2 composites. *Polymer Engineering & Science*, 29(23):1705–1721, 1989. DOI: 10.1002/pen.760292313.
- [8] D. A. Grewell and A. Benatar. Welding of plastics: Fundamentals and new developments. *International Polymer Processing*, 22(1):43–60, 2007. DOI: 10.3139/217.0051.
- [9] I. Fernandez-Villegas. In situ monitoring of ultrasonic welding of thermoplastic composites through power and displacement data. *Journal of Thermoplastic Composite Materials*, 28(1):66–85, 2015. DOI: 10.1177/0892705712475015.
- [10] H. Kim, S. Yarlagadda, J. Gillespie Jr, N. Shevchenko, and B. Fink. A study on the induction heating of carbon fiber reinforced thermoplastic composites. *Advanced Composite Materials - ADV COMPOS MATER*, 11(1):71–80, 2002. DOI: 10.1163/156855102753613309.
- [11] Vijay K. Stokes. Joining methods for plastics and plastic composites: An overview. *Polymer Engineering & Science*, 29(19):1310–1324, 1989. DOI: 10.1002/pen.760291903.
- [12] H. J. Yeh. Chapter 11 - ultrasonic welding of medical plastics. In *Joining and Assembly of Medical Materials and Devices*, Y. Zhou and M. D. Breyen (editors), pages 296–323. Woodhead Publishing, Cambridge, UK, 1st edition, 2013. ISBN: 978-1-84569-577-4. DOI: 10.1016/B978-0-8155-1581-4.50004-4.
- [13] J. D. N. Cheeke. *Fundamentals and applications of ultrasonic waves*. CRC Press - Taylor & Francis Group, LLC, Boca Raton, Florida, USA, 2nd edition, 2017. ISBN: 978-1-43-985494-5. DOI: 10.1201/b12260.
- [14] M. Hongoh, M. Yoshikuni, H. Hashii, T. Ueoka, and J. Tsujino. Welding characteristics of 67 khz ultrasonic plastic welding system using fundamental and higher-resonance-frequency vibrations. *Japanese Journal of Applied Physics*, 42(5B):2981–2985, 2003. DOI: 10.1143/JJAP.42.2981.

- [15] J. Tsujino, M. Hongoh, M. Yoshikuni, H. Hashii, and T. Ueoka. Welding characteristics of 27, 40 and 67 khz ultrasonic plastic welding systems using fundamental- and higher-resonance frequencies. *Ultrasonics*, 42(1):131–137, 2004. DOI: 10.1016/j.ultras.2004.02.009.
- [16] J. Tsujino, T. Tamura, T. Uchida, and T. Ueoka. Characteristics of two-vibration-system ultrasonic plastic welding with 90 khz and 20 khz vibration systems at right angles. *Japanese Journal of Applied Physics*, 35(1):5884–5889, 1996. DOI: 10.1143/jjap.35.5884.
- [17] A. Benatar. Chapter 12 - ultrasonic welding of plastics and polymeric composites. In *Power Ultrasonics*, J. A. Gallego-Juárez and K. F. Graff (editors), pages 295–312. Woodhead Publishing, Oxford, UK, 1st edition, 2015. ISBN: 978-1-78242-028-6. DOI: 10.1016/B978-1-78242-028-6.00012-0.
- [18] A. Levy, S. Le Corre, and A. Poitou. Ultrasonic welding of thermoplastic composites: A numerical analysis at the mesoscopic scale relating processing parameters, flow of polymer and quality of adhesion. *International Journal of Material Forming*, 7(1):39–51, 2011. DOI: 10.1007/s12289-012-1107-6.
- [19] H. Potente. Ultrasonic welding — principles & theory. *Materials & Design*, 5(5):228–234, 1984. DOI: 10.1016/0261-3069(84)90032-3.
- [20] S. F. Raza, S. A. Khan, and M. P. Mughal. Optimizing the weld factors affecting ultrasonic welding of thermoplastics. *International Journal of Advanced Manufacturing Technology*, 103(8):2053–2067, 2019. DOI: 10.1007/s00170-019-03681-7.
- [21] I. Fernandez Villegas and H. E. N. Bersee. Ultrasonic welding of advanced thermoplastic composites: An investigation on energy-directing surfaces. *Advances in Polymer Technology*, 29(2): 112–121, 2010. DOI: 10.1002/adv.20178.
- [22] B. C. P. Jongbloed, J. J. E. Teuwen, G. Palardy, and I. Fernandez Villegas. Improving weld uniformity in continuous ultrasonic welding of thermoplastic composites. In *ECCM18: 18th European Conference on Composite Materials*, pages 1–8, Athens, Greece, 2018. DOI: 10.1177/0021998319890405.
- [23] M. J. Troughton. Chapter 2 - ultrasonic welding. In *Handbook of Plastics Joining - A practical guide*, M. J. Troughton (editor), pages 15–35. William Andrew Publishing, Norwich, New York, USA, 2nd edition, 2009. ISBN: 978-0-81-551581-4. DOI: 10.1016/B978-0-8155-1581-4.50004-4.
- [24] S. A. Vendan, M. Natesh, A. Garg, and L. Gao. *Confluence of Multidisciplinary Sciences for Polymer Joining*. Springer Nature Singapore Pte Ltd., Singapore, Singapore, 1st edition, 2019. ISBN: 978-981-13-0625-9. DOI: 10.1007/978-981-13-0626-6.
- [25] V. N. Khmelev, A. N. Slivin, and A. D. Abramov. Research of parameter influence of ultrasonic welding process on conjuncture of polymeric thermoplastic materials. In *9th International Workshop and Tutorials on Electron Devices and Materials*, pages 272–278, Novosibirsk, Russia, 2008. DOI: 10.1109/SIBEDM.2008.4585905.
- [26] W. Kim, E. Kang, and D. Park. Evaluation of welding performance of 20 khz and 40 khz ultrasonic metal welding. In *IOP Conference Series: Materials Science and Engineering*, pages 1–6, Seoul, South Korea, 2017. DOI: 10.1088/1757-899X/248/1/012013.
- [27] M. Tadvi, A. Pandey, J. Prajapati, and J. Shah. Design and development of sonotrode for ultrasonic drilling. In *International Mechanical Engineering Congress and Exposition - Advanced Manufacturing*, pages 1–5, Houston, Texas, USA, 2015. DOI: 10.1115/IMECE2015-53023.
- [28] A. Arnau. *Piezoelectric Transducers and Applications*. Springer-Verlag, Heidelberg, Germany, 2nd edition, 2008. ISBN: 978-3-540-77508-9. DOI: 10.1007/978-3-540-77508-9.
- [29] W. D. Callister and W. D. C. William. *Materials Science and Engineering: An Introduction*. John Wiley & Sons, Limited, New York City, New York, USA, 5th edition, 2007. ISBN: 978-1-11-831922-2. DOI: 10.1108/acmm.2000.12847aae.001.

- [30] H. Wijshoff. The dynamics of the piezo inkjet printhead operation. *Physics Reports*, 491(4): 77–177, 2010. DOI: 10.1016/j.physrep.2010.03.003.
- [31] D. A. Grewell, A. Benatar, and J. B. Park. *Plastics and Composites Welding Handbook*. Hanser Gardener, Munich, Germany, 1st edition, 2003. ISBN: 978-1-56-990313-1.
- [32] A. Benatar, R. V. Eswaran, and S. K. Nayar. Ultrasonic welding of thermoplastics in the near-field. *Polymer Engineering & Science*, 29(23):1689–1698, 1989. DOI: 10.1002/pen.760292311.
- [33] M. Tolunay, P. Dawson, and K. Wang. Heating and bonding mechanisms in ultrasonic welding of thermoplastics. *Polymer Engineering & Science*, 23(1):726–733, 1983. DOI: 10.1002/pen.760231307.
- [34] K. Shu, W. Hsieh, and C. Chi. On the design and analysis of acoustic horns for ultrasonic welding. *Advanced Materials Research*, 475(1):1555–1558, 2012. DOI: 10.4028/www.scientific.net/AMR.472-475.1555.
- [35] K. H. W. Seah, Y. S. Wong, and L. C. Lee. Design of tool holders for ultrasonic machining using fem. *Journal of Materials Processing Technology*, 37(1):801–816, 1993. DOI: 10.1016/0924-0136(93)90138-V.
- [36] B. Behera, S. K. Sahoo, L. Patra, M. Rout, and K. Kanaujia. Finite element analysis of ultrasonic stepped horn. In *International Conference on Advances in Mechanical Engineering (ICAME)*, pages 60–64, Gujarat, India, 2011. DOI: 10.13140/RG.2.1.2065.3209.
- [37] P. K. Rai, V. Yadavak, and R. K. Patel. Modal analysis of horns used in ultrasonic machine. In *ARIMPIE - 2017*, pages 1–5, Himachal Pradesh, India, 2017. URL: https://www.researchgate.net/publication/330162147_Modal_Analysis_of_Horns_used_in_Ultrasonic_Machine.
- [38] M. Roopa Rani and R. Rudramoorthy. Computational modeling and experimental studies of the dynamic performance of ultrasonic horn profiles used in plastic welding. *Ultrasonics*, 53(3): 763–772, 2013. DOI: 10.1016/j.ultras.2012.11.003.
- [39] H. H. Hansen. Optimal design of an ultrasonic transducer. *Structural Optimization*, 14(3):150–157, 1997. DOI: 10.1007/BF01812517.
- [40] C. B. Bucknall, I. C. Drinkwater, and G. R. Smith. Hot plate welding of plastics: Factors affecting weld strength. *Polymer Engineering & Science*, 20(6):432–440, 1980. DOI: 10.1002/pen.760200609.
- [41] R. J. Young and P. A. Lovell. *Introduction to Polymers*. CRC Press - Taylor & Francis Group, LLC, Boca Raton, Florida, USA, 3rd edition, 2011. ISBN: 978-0-84-933929-5.
- [42] K. Balani, V. Verma, A. Arvind, and R. Narayan. Physical, thermal, and mechanical properties of polymers. In *Biosurfaces: A Materials Science and Engineering Perspective*, K. Balani, V. Verma, A. Arvind, and R. Narayan (editors), pages 329–344. John Wiley & Sons, Limited, Hoboken, New Jersey, USA, 1st edition, 2014. ISBN: 978-1-118-29997-5. DOI: 10.1002/9781118950623.app1.
- [43] N. Saba, M. Jawaid, O. Y. Alothman, and M. T. Paridah. A review on dynamic mechanical properties of natural fibre reinforced polymer composites. *Construction and Building Materials*, 106(1):149–159, 2016. DOI: 10.1016/j.conbuildmat.2015.12.075.
- [44] L. Ahmed, B. Zhang, S. Hawkins, M. S. Mannan, and Z. Cheng. Study of thermal and mechanical behaviors of flame retardant polystyrene-based nanocomposites prepared via in-situ polymerization method. *Journal of Loss Prevention in the Process Industries*, 49(1):229–240, 2017. DOI: 10.1016/j.jlp.2017.07.003.
- [45] J. Bergström. Chapter 2 - experimental characterization techniques. In *Mechanics of Solid Polymers*, J. Bergström (editor), pages 19–114. William Andrew Publishing, San Diego, California, USA, 1st edition, 2015. ISBN: 978-0-323-31150-2. DOI: 10.1016/B978-0-323-31150-2.00002-9.

- [46] V. G. Geethamma, R. Asaletha, N. Kalarikkal, and S. Thomas. Vibration and sound damping in polymers. *Resonance*, 19(9):821–833, 2014. DOI: 10.1007/s12045-014-0091-1.
- [47] B. Jiang, H. Peng, W. Wu, Y. Jia, and Y. Zhang. Numerical simulation and experimental investigation of the viscoelastic heating mechanism in ultrasonic plasticizing of amorphous polymers for micro injection molding. *Polymers*, 8(5):1–12, 2016. DOI: 10.3390/polym8050199.
- [48] A. Levy, S. Le Corre, and I. Fernandez Villegas. Modeling of the heating phenomena in ultrasonic welding of thermoplastic composites with flat energy directors. *Journal of Materials Processing Technology*, 214(7):1361–1371, 2014. DOI: 10.1016/j.jmatprotec.2014.02.009.
- [49] F. Awaja. Autohesion of polymers. *Polymer*, 97(1):388–408, 2016. DOI: 10.1016/j.polymer.2016.05.043.
- [50] G. Vasconcelos, R. Mazur, E. Botelho, M. C. Rezende, and M. Costa. Evaluation of crystallization kinetics of poly (ether-ketone-ketone) and poly (ether-ether-ketone) by dsc. *Journal of Aerospace Technology and Management*, 2(1):155–162, 2010. DOI: 10.5028/jatm.2010.02026310.
- [51] M. H. E. Van der Beek, G. W. M. Peters, and H. E. H. Meijer. The influence of cooling rate on the specific volume of isotactic poly(propylene) at elevated pressures. *Macromolecular Materials and Engineering*, 290(5):443–455, 2005. DOI: 10.1002/mame.200500027.
- [52] B. R. Cho and J. L. Kardos. Consolidation and self-bonding in poly(ether ether ketone) (peek). *Journal of Applied Polymer Science*, 56(11):1435–1454, 1995. DOI: 10.1002/app.1995.070561106.
- [53] G. Wypych. Pekk polyetherketoneketone. In *Handbook of Polymers*, G. Wypych (editor), pages 380–382. ChemTec Publishing, Toronto, Canada, 2nd edition, 2016. ISBN: 978-1-895198-92-8. DOI: 10.1016/B978-1-895198-92-8.50117-8.
- [54] G. Wypych. Peek polyetheretherketone. In *Handbook of Polymers*, G. Wypych (editor), pages 366–370. ChemTec Publishing, Toronto, Canada, 2nd edition, 2016. ISBN: 978-1-895198-92-8. DOI: 10.1016/B978-1-895198-92-8.50113-0.
- [55] G. Wypych. Pp polypropylene. In *Handbook of Polymers*, G. Wypych (editor), pages 497–504. ChemTec Publishing, Toronto, Canada, 2nd edition, 2016. ISBN: 978-1-895198-92-8. DOI: 10.1016/B978-1-895198-92-8.50156-7.
- [56] J. Davidson. *Multiscale modeling and simulation of crosslinked polymers*. Ph.d thesis, University of Michigan, 2014. URL: https://www.researchgate.net/publication/295404630_Multiscale_modeling_and_simulation_of_crosslinked_polymers.
- [57] A. Diez-Pascual, M. Naffakh, M. Gómez, C. Marco, Gary Ellis, J. González-Domínguez, A. An-són, M. Martínez, Y. Martinez Rubi, B. Simard, and B. Ashrafi. The influence of a compatibilizer on the thermal and dynamic mechanical properties of peek/carbon nanotube composites. *Nanotechnology*, 20(1):315707, 2009. DOI: 10.1088/0957-4484/20/31/315707.
- [58] M. Yahiaoui, F. Chabert, J. Y. Paris, V. Nassiet, and J. Denape. Friction, acoustic emission, and wear mechanisms of a pekk polymer. *Tribology International*, 132(1):154–164, 2019. DOI: 10.1016/j.triboint.2018.12.020.
- [59] S. Farzaneh and A. Tcharkhtchi. Viscoelastic properties of polypropylene reinforced with mica in α and α_c transition zones. *International Journal of Polymer Science*, 2011(1):1–5, 2011. DOI: 10.1155/2011/427095.
- [60] T. Choupin. *Mechanical performances of PEKK thermoplastic composites linked to their processing parameters*. Ph.d thesis, Ecole nationale supérieure d'arts et métiers - ENSAM, 2017. URL: https://www.researchgate.net/publication/327952758_Mechanical_performances_of_PEKK_thermoplastic_composites_linked_to_their_processing_parameters.

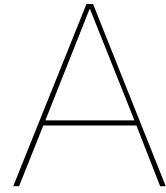
- [61] J. Mofokeng, A. Luyt, T. Tábi, and J. Kovacs. Comparison of injection moulded, natural fibre reinforced composites with pp and pla as matrices. *Journal of Thermoplastic Composite Materials*, 25(1):927–948, 2012. DOI: 10.1177/0892705711423291.
- [62] A. Gopanna, S. P. Thomas, K. P. Rajan, R. Rajan, E. Rainosalo, J. Zavašnik, and M. Chavali. Investigation of mechanical, dynamic mechanical, rheological and morphological properties of blends based on polypropylene (pp) and cyclic olefin copolymer (coc). *European Polymer Journal*, 108(1):439–451, 2018. DOI: 10.1016/j.eurpolymj.2018.09.030.
- [63] M. Coulson, Q. Cortes, L. Enrique, E. Dantras, A. Lonjon, and C. Lacabanne. Dynamic rheological behavior of poly(ether ketone ketone) from solid state to melt state. *Journal of Applied Polymer Science*, 135(27):1–7, 2018. DOI: 10.1002/app.46456.
- [64] S. R. Kim, D. H. Kim, D. J. Kim, M. H. Kim, and J. M. Park. Study on thermal conductivity of polyetheretherketone/thermally conductive filler composites. *Solid State Phenomena*, 126(1):1079–1082, 2007. DOI: 10.4028/www.scientific.net/SSP.124-126.1079.
- [65] Toray. Product data sheet toray cetex tc1320 pekk. 2019. URL: <https://www.toraytac.com/>.
- [66] Solvay. Technical data sheet solvay apc (pekk-fc). 2017. URL: <https://www.solvay.com/>.
- [67] Sabic. Product data sheet udmx gpp45-70 tape. 2018. URL: <https://www.sabic.com>.
- [68] A. Benatar and Z. Cheng. Ultrasonic welding of thermoplastics in the far-field. *Polymer Engineering & Science*, 29(23):1699–1704, 1989. DOI: 10.1002/pen.760292312.
- [69] A. Benatar. Chapter 10 - sound in enclosures. In *Acoustics: Sound Fields, Transducers and Vibration*, L. Beranek and T. Mellow (editors), pages 511–545. Academic Press, Oxford, UK, 2nd edition, 2019. ISBN: 978-0-12-815227-0. DOI: 10.1016/B978-0-12-815227-0.00010-8.
- [70] K. S. Suresh, M. R. Rani, K. Prakasan, and R. Rudramoorthy. Modeling of temperature distribution in ultrasonic welding of thermoplastics for various joint designs. *Journal of Materials Processing Technology*, 186(1):138–146, 2007. DOI: 10.1016/j.jmatprotec.2006.12.028.
- [71] M. Rani, K. Prakasan, and R. Rudramoorthy. Study of different joints for ultrasonic welding of semicrystalline polymers. *Experimental Techniques - EXP TECH*, 33(1):1–7, 2008. DOI: 10.1111/j.1747-1567.2008.00399.x.
- [72] A. Al-Obaidi. *Ultrasonic Joining of Metal-Polymer Surfaces*. Ph.d thesis, The University of Sheffield, 2017. URL: https://www.researchgate.net/publication/330452244_Ultrasonic_Joining_of_Metal-Polymer_Surfaces.
- [73] D. G. Papageorgiou, D. N. Bikiaris, and K. Chrissafis. Effect of crystalline structure of polypropylene random copolymers on mechanical properties and thermal degradation kinetics. *Thermochimica Acta*, 543(1):288–294, 2012. DOI: 10.1016/j.tca.2012.06.007.
- [74] C. J. Nonhof and G. A. Luiten. Estimates for process conditions during the ultrasonic welding of thermoplastics. *Polymer Engineering & Science*, 36(9):1177–1183, 1996. DOI: 10.1002/pen.10511.
- [75] Z. Zhang, X. Wang, L. Yi, Z. Zhang, and L. Wang. Study on heating process of ultrasonic welding for thermoplastics. *Journal of Thermoplastic Composite Materials*, 23(5):647–664, 2010. DOI: 10.1177/0892705709356493.
- [76] SciPy Community. Scipy reference guide. 2013. URL: <https://docs.scipy.org>.
- [77] G. Wypych. Ps polystyrene. In *Handbook of Polymers*, G. Wypych (editor), pages 560–566. ChemTec Publishing, Toronto, Canada, 2nd edition, 2016. ISBN: 978-1-895198-92-8. DOI: 10.1016/B978-1-895198-92-8.50175-0.
- [78] D. D. L. Chung. Materials for thermal conduction. *Applied Thermal Engineering*, 21(16):1593–1605, 2001. DOI: 10.1016/S1359-4311(01)00042-4.

- [79] M. Schäkel, S. M. A. Hosseini, H. Janssen, I. Baran, and C. Brecher. Temperature analysis for the laser-assisted tape winding process of multi-layered composite pipes. *Procedia CIRP*, 85(1): 171–176, 2019. DOI: 10.1016/j.procir.2019.09.003.
- [80] D. Y. Wu, S. Meure, and D. Solomon. Self-healing polymeric materials: A review of recent developments. *Progress in Polymer Science*, 33(5):479–522, 2008. DOI: 10.1016/j.progpolymsci.2008.02.001.
- [81] F. Yang and R. Pitchumani. Healing of thermoplastic polymers at an interface under nonisothermal conditions. *Macromolecules*, 35(8):3213–3224, 2002. DOI: 10.1021/ma010858o.
- [82] R. P. Wool and K. M. O'Connor. A theory crack healing in polymers. *Journal of Applied Physics*, 52(10):5953–5963, 1981. DOI: 10.1063/1.328526.
- [83] G. Wypych. Abs poly(acrylonitrile-co-butadiene-co-styrene). In *Handbook of Polymers*, G. Wypych (editor), pages 5–11. ChemTec Publishing, Toronto, Canada, 2nd edition, 2016. ISBN: 978-1-895198-92-8. DOI: 10.1016/B978-1-895198-92-8.50005-7.
- [84] G. Wypych. Pe polyethylene. In *Handbook of Polymers*, G. Wypych (editor), pages 349–354. ChemTec Publishing, Toronto, Canada, 2nd edition, 2016. ISBN: 978-1-895198-92-8. DOI: 10.1016/B978-1-895198-92-8.50109-9.
- [85] Y. K. Chuah, L. Chien, B. C. Chang, and S. Liu. Effects of the shape of the energy director on far-field ultrasonic welding of thermoplastics. *Polymer Engineering & Science*, 40(1):157–167, 2000. DOI: 10.1002/pen.11149.
- [86] K. Goto, K. Imai, M. Arai, and T. Ishikawa. Shear and tensile joint strengths of carbon fiber-reinforced thermoplastics using ultrasonic welding. *Composites Part A: Applied Science and Manufacturing*, 116(1):126–137, 2019. DOI: 10.1016/j.compositesa.2018.10.032.
- [87] F. R. Sacchetti. *Interlaminar toughness of fusion bonded thermoplastic composites*. Ph.d thesis, University of Twente, 2017. DOI: 10.3990/1.9789036543781.
- [88] Y. Su, M. de Rooij, W. J. B. Grouve, and L. Warnet. Characterisation of metal–thermoplastic composite hybrid joints by means of a mandrel peel test. *Composites Part B: Engineering*, 95(1):293–300, 2016. DOI: 10.1016/j.compositesb.2016.03.055.
- [89] T. Kok, W. J. B. Grouve, L. L. Warnet, and R. Akkerman. Effect of ply orientation on bond strength in fiber-placed composites. In *ICCM International Conferences on Composite Materials*, pages 1–12, Copenhagen, Denmark, 2015. URL: <https://research.utwente.nl/en/publications/effect-of-ply-orientation-on-bond-strength-in-fiber-placed-compos>.
- [90] W. J. B. Grouve, L. L. Warnet, and R. Akkerman. Critical assessment of the mandrel peel test for fiber reinforced thermoplastic laminates. *Engineering Fracture Mechanics*, 101(1):96–108, 2013. DOI: 10.1016/j.engfracmech.2012.07.005.
- [91] L. F. Kawashita, A. J. Kinloch, D. R. Moore, and J. G. Williams. A critical investigation of the use of a mandrel peel method for the determination of adhesive fracture toughness of metal-polymer laminates. *Engineering Fracture Mechanics*, 73(16):2304–2323, 2006. DOI: 10.1016/j.engfracmech.2006.04.025.
- [92] K. Reincke and W. Grellmann. Chapter 18 - approaches to characterise the mechanical properties of films and elastomers. In *Deformation and Fracture Behaviour of Polymer Materials*, W. Grellmann and B. Langer (editors), pages 257–270. Springer-Verlag, Heidelberg, Germany, 1st edition, 2017. ISBN: 978-3-319-41877-3. DOI: 10.1007/978-3-319-41879-7_18.
- [93] L. F. Kawashita, D. R. Moore, and J. G. Williams. Protocols for the measurement of adhesive fracture toughness by peel tests. *The Journal of Adhesion*, 82(10):973–995, 2006. DOI: 10.1080/00218460600876142.

- [94] L. F. Kawashita, D. R. Moore, and J. G. Williams. Comparison of peel tests for metal–polymer laminates for aerospace applications. *The Journal of Adhesion*, 81(6):561–586, 2005. DOI: 10.1080/00218460590954557.
- [95] S. Teixeira de Freitas and J. Sinke. Adhesion properties of bonded composite-to-aluminium joints using peel tests. *The Journal of Adhesion*, 90(6):511–525, 2014. DOI: 10.1080/00218464.2013.850424.
- [96] G. Wagner, F. Balle, and D. Eifler. Ultrasonic welding of aluminum alloys to fiber reinforced polymers. *Advanced Engineering Materials*, 15(9):792–803, 2013. DOI: 10.1002/adem.201300043.
- [97] M. L. Herring, J. I. Mardel, and B. L. Fox. The effect of material selection and manufacturing process on the surface finish of carbon fibre composites. *Journal of Materials Processing Technology*, 210(7):926–940, 2010. DOI: 10.1016/j.jmatprotec.2010.02.005.
- [98] A. Jiju. *Design of Experiments for Engineers and Scientists*. Elsevier Ltd., London, UK, 2nd edition, 2003. ISBN: 978-0-08-099417-8. DOI: 10.1016/C2012-0-03558-2.
- [99] R.H. Myers, D.C. Montgomery, and C.M. Anderson-Cook. *Response Surface Methodology: Process and Product Optimization Using Designed Experiments*. John Wiley & Sons, Limited, Hoboken, New Jersey, USA, 4th edition, 2016. ISBN: 978-1-118-91601-8.
- [100] A. Field. *Discovering statistics using SPSS*. Sage Publications Ltd., London, UK, 3rd edition, 2005. ISBN: 978-1-84787-906-6.
- [101] D. C. Montgomery. *Design and Analysis of Experiments*. John Wiley & Sons, Limited, Westford, Massachusetts, USA, 8th edition, 2013. ISBN: 978-1118-14692-7. DOI: doi.org/10.1002/ep.11743.
- [102] S. Liu, I. T. Chang, and S. Hung. Factors affecting the joint strength of ultrasonically welded polypropylene composites. *Polymer Composites*, 22(1):132–141, 2001. DOI: 10.1002/pc.10525.
- [103] S. Liu and I. T. Chang. Optimizing the weld strength of ultrasonically welded nylon composites. *Journal of Composite Materials*, 36(5):611–624, 2002. DOI: 10.1177/0021998302036005476.
- [104] R. M. Rani, K. S. Suresh, K. Prakasan, and R. Rudramoorthy. A statistical study of paramaters in ultrasonic welding of plastics. *Experimental Techniques*, 31(5):53–58, 2007. DOI: 10.1111/j.1747-1567.2007.00182.x.
- [105] P.G. Mathews. *Design of Experiments with MINITAB*. ASQ Quality Press, Milwaukee, Wisconsin, USA, 1st edition, 2005. ISBN: 978-0-87389-637-5.
- [106] M. A. Bezerra, R. E. Santelli, E. P. Oliveira, L. S. Villar, and L. A. Escaleira. Response surface methodology (rsm) as a tool for optimization in analytical chemistry. *Talanta*, 76(5):965–977, 2008. DOI: 10.1016/j.talanta.2008.05.019.
- [107] P. Saha and D. Waghmare. Parametric optimization for autogenous butt laser welding of sub-millimeter thick ss 316 sheets using central composite design. *Optics & Laser Technology*, 122(1):105833, 2020. DOI: 10.1016/j.optlastec.2019.105833.
- [108] S. Huang, R. Chen, H. Zhang, J. Ye, X. Yang, and J. Sheng. A study of welding process in connecting borosilicate glass by picosecond laser pulses based on response surface methodology. *Optics & Laser Technology*, 131(1):1–11, 2020. DOI: 10.1016/j.optlastec.2020.106427.
- [109] M. W. Hattab. On the use of data transformation in response surface methodology. *Quality and Reliability Engineering International*, 34(6):1185–1194, 2018. DOI: 10.1002/qre.2317.
- [110] Minitab, LLC. "Minitab Support". Methods and formulas for the analysis of variance in Analyze Response Surface Design. www.minitab.com. (Accessed 09-07-2020).

- [111] H. R. F. Masoumi, M. Basri, A. Kassim, D. K. Abdullah, Y. Abdollahi, S. S. Abd Gani, and M. Rezaee. Statistical optimization of process parameters for lipase-catalyzed synthesis of triethanolamine-based esterquats using response surface methodology in 2-liter bioreactor. *The Scientific World Journal*, 4(1):1–9, 2013. DOI: 10.1155/2013/962083.
- [112] D. J. Hosken, D. L. Buss, and D. J. Hodgson. Beware the f test (or, how to compare variances). *Animal Behaviour*, 136(1):119–126, 2018. DOI: 10.1016/j.anbehav.2017.12.014.
- [113] J. Xu. Randomized blocks designs and two-way anova. 2014. URL: <http://www.bbk.ac.uk/ems/faculty/xu>.
- [114] M. H. Kutner, C. J. Nachtsheim, J. Neter, and W. Lia. *Applied Linear Statistical Models*. McGraw-Hill/Irwin, New York City, New York, USA, 5th edition, 2014. ISBN: 978-1-118-91601-8.
- [115] D. J. Bray, S. G. Gilmour, F. J. Guild, and A. C. Taylor. The effects of particle morphology on the analysis of discrete particle dispersion using delaunay tessellation. *Composites Part A: Applied Science and Manufacturing*, 54(1):37–45, 2013. DOI: 10.1016/j.compositesa.2013.07.003.
- [116] D. J. Bray, S. G. Gilmour, F. J. Guild, T. H. Hsieh, K. Masania, and A. C. Taylor. Quantifying nanoparticle dispersion: application of the delaunay network for objective analysis of sample micrographs. *Journal of Materials Science*, 46(19):6437–6452, 2011. DOI: 10.1007/s10853-011-5615-4.
- [117] A. Makwana and V. R. Patel. An experimental investigation of ultrasonic welding on thermoplastic material. *International Journal for Scientific Research & Development*, 2(5):838–841, 2017. DOI: 10.1016/j.protcy.2016.03.062.
- [118] R. Schledjewski and A. Schlarb. In-situ consolidation of thermoplastic tape material effects of tape quality on resulting part properties. In *International SAMPE Symposium and Exhibition*, pages 1–12, Baltimore, Maryland, USA, 2007. URL: https://www.researchgate.net/publication/289787615_In-situ_consolidation_of_thermoplastic_tape_material_effects_of_tape_quality_on_resulting_part_properties.
- [119] B. Bertonecelj. A voronoi-diagram analysis of the microstructures in bulk-molding compounds and its correlation with the mechanical properties. *Express Polymer Letters*, 10(6):493–505, 2016. DOI: 10.3144/expresspolymlett.2016.47.
- [120] J. Zangenberg, J. B. Larsen, R. C. Østergaard, and P. Brøndsted. Methodology for characterisation of glass fibre composite architecture. *Plastics, Rubber and Composites*, 41(5):187–193, 2012. DOI: 10.1179/1743289811Y.0000000067.
- [121] G. Jeong, J. Lim, C. Choi, and S. Kim. A virtual experimental approach to evaluate transverse damage behavior of a unidirectional composite considering noncircular fiber cross-sections. *Composite Structures*, 228(1):1–11, 2019. DOI: 10.1016/j.compstruct.2019.111369.
- [122] T. Fereirra and W. Rasband. Imagej user guide. 2012. URL: <https://imagej.nih.gov/>.
- [123] I. V. Grishagin. Automatic cell counting with imagej. *Analytical Biochemistry*, 473(1):63–65, 2015. DOI: 10.1016/j.ab.2014.12.007.
- [124] Boikon. Tenax e tpud peek-2-34-ims65 properties (internal company data). 2020.
- [125] Hexcel. Product data sheet hextow as4d carbon fiber. 2016. URL: <https://www.hexcel.com/>.
- [126] Teijin Carbon. Product data sheet teijin tenax filament yarn. 2020. URL: <https://www.tejincarbon.com>.
- [127] F. Sacchetti, W. J. B. Grouve, L. L. Warnet, and I. Fernandez Villegas. Woven fabric composites: Can we peel it? *Procedia Structural Integrity*, 2(1):245–252, 2016. DOI: 10.1016/j.prostr.2016.06.032.

- [128] F. Sacchetti, W. J. B. Grouve, Laurent L. Warnet, and I. Fernandez-Villegas. Interlaminar fracture toughness of 5hs carbon/peek laminates. a comparison between dcb, els and mandrel peel tests. *Polymer Testing*, 66(1):13–23, 2018. DOI: 10.1016/j.polymertesting.2017.12.005.
- [129] D. J. Bray, S. G. Gilmour, F. J. Guild, and A. C. Taylor. Quantifying nanoparticle dispersion by using the area disorder of delaunay triangulation. *Journal of the Royal Statistical Society: Series C (Applied Statistics)*, 61(2):253–275, 2012. DOI: 10.1111/j.1467-9876.2011.01009.x.



Microstructure Characterization Python Script

```
1  """
2  Created on Mon Feb  3 14:50:42 2020
3
4  @author: Nico-Katuin - 4738373 - Msc thesis TU Delft/ Boikon B.V.
5  """
6  # coding=utf-8
7  # =====
8  # Input packages
9  # =====
10 import numpy as np
11 import matplotlib.pyplot as plt
12 from scipy.spatial import Voronoi, ConvexHull
13 from shapely.geometry import Polygon
14 import openpyxl
15 import matplotlib as mpl
16 import matplotlib.cm as cm
17 from matplotlib.axes._axes import _log as matplotlib_axes_logger
18 matplotlib_axes_logger.setLevel('ERROR')
19 from matplotlib import rcParams
20 #Default TU Delft font for Latex
21 rcParams['font.family'] = 'sans-serif'
22 rcParams['font.sans-serif'] = ['Arial']
23
24 # =====
25 # Input Variables
26 # =====
27
28 #Color definition
29 Blue      = np.array([0.007, 0.317, 0.513])
30 LightBlue = np.array([0, 0.588, 0.862])
31 Cyan      = np.array([0, 0.882, 0.882])
32
33 #File location definition
34 # #0 = CF-PEEK (Teijin), #1 = CF-PEKK (Solvay), #2 = CF-PEKK (Toray)
35 fileloc = 0
36
37
38 HorPixel = [856,867,880]           # width of micrograph sections in pixels
39 VerPixel = [734,679,738]         # height of micrograph sections in pixels
40 segments = [18,24,27]            # Amount of segments in fib/res distribution
```

```

41 segments=segments[ fileloc ]
42 D_fib    = [9.06,11.465,11.475]    # Averaged fibre diameters , measured with ImageJ
43 t_tape   = [0.225,0.197,0.150]    # Measured actual tape thickness
44 t_tape   = t_tape[ fileloc ]
45
46 #Transformation between pixels and micrometers
47 T_ratio  = 0.00055                  # Equivalent for all three tapes
48
49 #File locations:
50 directory = ['01-PEEK_Teijin', '02-PEKK_Solvay', '03-PEKK_Toray']
51 plotnames = ['CF-PEEK - Teijin', 'CF-PEKK - Solvay', 'CF-PEKK - Toray']
52 ## Automated list generation
53 if fileloc ==0:
54     first_img = 8                    # First image number of sequence of images analysed
55     last_img  = 13                   # Last image number of sequence of images analysed
56
57 if fileloc ==1:
58     first_img = 2
59     last_img  = 7
60
61 if fileloc ==2:
62     first_img = 2
63     last_img  = 7
64
65
66 number = []                          # List of image numbers for plotting purpose etc.
67 for i in np.arange(first_img ,last_img+1,1):
68     number.append(f'{i}')
69
70 FibCorFile = []                      # List of Excel file names for fibre coordinate extraction
71 for i in np.arange(first_img ,last_img+1,1):
72     FibCorFile.append(f'FibCor_{i}')
73
74 BoundCorFile = []                   # List of Excel file names for boundary coordinate extraction
75 for i in np.arange(first_img ,last_img+1,1):
76     BoundCorFile.append(f'BoundCor_{i}_int')
77
78 HorPixel = HorPixel[ fileloc ]
79 VerPixel  = VerPixel[ fileloc ]
80 D_fib     = D_fib[ fileloc ]
81
82 #Midline coordinates definition to determine the skewed lines , are different per
    UD tape because each micrographs is positioned differently
83 #Image coordinates for determining inclination of segments - CF-PEEK Teijin
84 if fileloc == 0:
85     Y8_L = VerPixel - 224
86     Y8_R = VerPixel - 228
87     Y9_L = Y8_R
88     Y9_R = VerPixel - 220
89     Y10_L = Y9_R
90     Y10_R = VerPixel - 240
91     Y11_L = Y10_R
92     Y11_R = VerPixel - 225
93     Y12_L = Y11_R
94     Y12_R = VerPixel - 233
95     Y15_L = VerPixel - 322
96     Y15_R = VerPixel - 322
97
98     Y_midline = [[Y8_L-5,Y8_R-5],[Y9_L,Y9_R],[Y10_L,Y10_R],[Y11_L,Y11_R],[Y12_L,
    Y12_R],[Y15_L,Y15_R]]
99

```

```

100 if fileloc == 1:
101 #Image coordinates for determining inclination of segments - CF-PEKK Solvay
102     Y2_L = VerPixel - 203
103     Y2_R = VerPixel - 269
104     Y3_L = Y2_R
105     Y3_R = VerPixel - 265
106     Y4_L = Y3_R
107     Y4_R = VerPixel - 316
108     Y5_L = Y4_R
109     Y5_R = VerPixel - 372
110     Y6_L = Y5_R
111     Y6_R = VerPixel - 381
112     Y7_L = Y6_R
113     Y7_R = VerPixel - 425
114
115     Y_midline = [[Y2_L+8,Y2_R+8],[Y3_L+5,Y3_R+5],[Y4_L,Y4_R],[Y5_L,Y5_R],[Y6_L,
Y6_R],[Y7_L,Y7_R]]
116
117 if fileloc ==2:
118 #Image coordinates for determining inclination of segments - CF-PEKK Toray
119     Y2_L = VerPixel - 246
120     Y2_R = VerPixel - 231
121     Y3_L = Y2_R
122     Y3_R = VerPixel - 213
123     Y4_L = Y3_R
124     Y4_R = VerPixel - 192
125     Y5_L = Y4_R
126     Y5_R = VerPixel - 175
127     Y6_L = Y5_R
128     Y6_R = VerPixel - 156
129     Y7_L = Y6_R
130     Y7_R = VerPixel - 148
131
132     Y_midline = [[Y2_L,Y2_R],[Y3_L,Y3_R],[Y4_L,Y4_R],[Y5_L,Y5_R],[Y6_L+5,Y6_R+5],[
Y7_L,Y7_R]]
133
134 #Horizontal coordinates for defining skewed lines
135 X_midline = [0,HorPixel]
136
137 # =====
138 # =====
139 # # Python functions
140 # =====
141 # =====
142
143 # =====
144 # FUNCTION BLOCK 1 & 4:
145 # Function to extract fibre and boundary locations from excel file
146 # =====
147 def CoordinateExtraction(FibCorFile, BoundCorFile):
148     """
149     Input:  FibCorFile;  Excel sheet with fibre location coordinates
150           BoundCorFile; Excel sheet with boundary location coordinates
151     Output: coordinates; List of fibre location coordinates from Excel
152           boundary;     List of boundary location coordinates from Excel
153     """
154
155     # Opening Excel file with active sheet of fibre x-, y-coordinates
156     book = openpyxl.load_workbook(directory[fileloc]+' /01-CoordinatesFiles/' +
FibCorFile[q]+' .xlsx')
157     sheet1 = book.active

```

```

158
159
160
161 #Extract fibre coordinates (x,y data) from FibCor Excel sheet, ignore first
row because of ImageJ output
162 coordinates = []
163 for row_i in range(2, sheet1.max_row + 1):
164     x = float(sheet1.cell(row=row_i, column=1).value)
165     y = float(sheet1.cell(row=row_i, column=2).value)
166     coordinates.append([x,(VerPixel-y)])
167 coordinates = np.asarray(coordinates)
168
169 # Opening Excel file with active sheet of boundary x-, y-coordinates
170 book = openpyxl.load_workbook(directory[fileloc]+'/'+'01-CoordinatesFiles/'+'
BoundCorFile[q]+''.xlsx')
171 sheet2 = book.active
172
173 # Extract boundary coordinates (x,y data) from BoundCor Excel sheet, ignore
first row because of ImageJ output
174 BoundaryCoordinates = []
175 for row_j in range(2, sheet2.max_row+1):
176     x = float(sheet2.cell(row=row_j, column=1).value)
177     y = float(sheet2.cell(row=row_j, column=2).value)
178     BoundaryCoordinates.append([x,(VerPixel-y)])
179 BoundaryCoordinates = np.asarray(BoundaryCoordinates)
180
181 #Create polygon from all imported boundary coordinates
182 boundary = Polygon(BoundaryCoordinates)
183
184 return coordinates, boundary
185
186 # =====
187 # FUNCTION BLOCK 2 & 3:
188 # Function to finitize the voronoi vertices which are at infinity
189 # =====
190 # =====
191 # Code to finitize inifite Voronoi cells, obtained and modified from:
192 # https://stackoverflow.com/questions/20515554/colorize-voronoi-diagram?lq=1
193 # =====
194 def voronoi_finite_polygons_2d(vor):
195     """
196     Input: vor;          Voronoi Diagram of coordinates
197     Output: new_regions; List of inidices of (new) Voronoi vertices
198             new_vertices; List of initial Voronoi vertex coordinates (x,y)
199                    with new vertices added at a finite distance added
200                    to the end of the list.
201     """
202     #Empty list for the new regions and copy array of 'old' vertices to a new list
203     new_regions = []
204     new_vertices = vor.vertices.tolist()
205
206     #Center vector, mean of x- and y-coordinate of input coordinates
207     center = vor.points.mean(axis=0)
208     #Radius distance of 2x (amx fibre x-,y-coordinate) for calculation to make
inifite Voronoi vertices finite
209     dist = 2*vor.points.ptp().max()
210
211     """
212
213     vor.ridge_points => array ([N*[]]) where N = number of Voronoi ridges (lines),
Voronoi ridge is always perpendicular to a line drawn between two input points

```

```

. [Ppoint1,Ppoint2] Defines between which input points the Voronoi ridge is 90
deg.
214
215 vor.ridge_vertices => list of tuples [N*[]] where N = number of Voronoi
vertices. [Vpoint1,Vpoint2] defines indices of Voronoi vertices defining each
Voronoi ridge, -1 index defines point at infinity.
216
217 The for loop below defines N*[p1,p2,v1,v2] where N = number of input points
and creates dictionary item for each input point, p1 (and second input point,
p2) where v1 and v2 represent the Voronoi vertex indices of the Voronoi ridge (
perpendicular to line drawn between p1 and p2 input points) vertices
"""
218
219 #Empty dictionary for Voronoi ridges
220 all_ridges = {}
221 #Append point1 and corresponding p2 with v1 and v2, also append p2 and
corresponding p1 with v1 and 2
222 for (p1, p2), (v1, v2) in zip(vor.ridge_points, vor.ridge_vertices):
223     all_ridges.setdefault(p1, []).append((p2, v1, v2))
224     all_ridges.setdefault(p2, []).append((p1, v1, v2))
225
226 #Reconstruct infinite regions, point_region: python list with cell indices
227 for p1, region in enumerate(vor.point_region):
228     vertices = vor.regions[region] #list with indices corresponding to cell
229
230     #When all indices >=0 -> no infinite points -> finite area, append
Voronoi vertices to the list of 'new' regions
231     if all(Vor_index >= 0 for Vor_index in vertices):
232         new_regions.append(vertices)
233         continue
234
235     #Indices not all >0 -> make Voronoi vertices finite
236     ridges = all_ridges[p1] # Extract p1 related data from dictionary
237
238     #ridges does contain multiple p1,p2,v1,v2 combinations, filters out the
finite regions with same p1 where v1 and v2 >0
239     new_region = [v for v in vertices if v >= 0]
240
241     #When v2 is the -1 Voronoi vertex, swap with v1 to make v1 leading
variable for Vertex at infinity. If v2 >= 0 and v1 >=1, this ridge is already
in the new_region list
242     for p2, v1, v2 in ridges:
243         if v2 < 0:
244             v1, v2 = v2, v1
245         if v1 >= 0:
246             continue
247
248
249     #v1 is the point at infinity and must become finite. Define tangent
vector between p1 and p2 with ((Xp2 - Xp1), (Yp2-Yp1) = (Xt,Yt))
250     t = vor.points[p2] - vor.points[p1]
251
252     #Normalize tangent vector by means of t / sqrt(Xt^2+Yt^2)
253     t = t / np.linalg.norm(t)
254     #Define normal vector of t
255     n = np.array([-t[1], t[0]])
256
257     #Define midpoint between p1 and p2 input coordinates
258     midpoint = vor.points[[p1, p2]].mean(axis=0)
259
260     #Vector of normal vector times sign dot product between midpoint and
centre vector

```

```

261         direction = np.sign(np.dot(midpoint - center, n)) * n
262
263         #Finite point is defined based on coordinates of Voronoi vertex (v2)
and direction vector * radius distance
264         fin_point = vor.vertices[v2] + (direction * dist)
265
266         #The length of new_vertices list determines the new Voronoi vertex
index
267         new_region.append(len(new_vertices))
268
269         #Appends new finite Voronoi vertex coordinates to list of original
Voronoi vertex coordinates (extends the original list)
270         new_vertices.append(fin_point.tolist())
271
272         #New Voronoi vertex coordinates (x,y) array (with original finite Voronoi
indices plus the corresponding 'new' fin_point coordinates ([N*[x,y]]) where N
= number of Voronoi vertices of specific cell)
273         vs = np.asarray([new_vertices[v] for v in new_region])
274
275
276         #Average vector of all Voronoi vertex coordinates
277         c = vs.mean(axis=0)
278         #Subtract mean from vectors from vs array and define angle between
horizontal axis and calculated mean vector
279         angles = np.arctan2(vs[:,1] - c[1], vs[:,0] - c[0])
280
281         #Sort angles counter clock-wise
282         new_region = np.array(new_region)[np.argsort(angles)]
283
284         #Append new region to array of all regions ('new_regions')
285         new_regions.append(new_region.tolist())
286
287         return new_regions, np.asarray(new_vertices)
288
289 # =====
290 # FUNCTION BLOCK 5:
291 # Function for polygon modification according to specified boundary and polygon
292 # plots with color plot specified according to local FRR
293 # =====
294 def PolygonModification(regions, vor, vertices, D_fib):
295     """
296     Input: vor;          Voronoi pattern applied to the input coordinates
297           regions;      Finitized voronoi regions
298           vertices;     Array of all Voronoi vertices (incl modified)
299           D_fib;        Measured fibre diameter
300     Output: norm;       Normalized color map between 0 and 1
301           Area;         List with areas of all polygono shapes
302     """
303     Elst          = [ ]
304     Area          = [ ]                #List for area values (unsorted areas)
305     Area_ordered2 = [0]*len(regions)   #list of areas orderd by CN number
306     Area_net2     = [0]*len(regions)   #List for nett areas (Acell-Afib)
307     Local_FibVol2 = [0]*len(regions)   #FRR ratio of Voronoi cell
308     n= 0          #Counter definition
309     A_fib = np.pi*(D_fib/2)**2        #Average area of fibre in pixels^2
310
311     #Normalize data from 0 to 1 without clipping (for cells with FRR out-of-range)
312     norm = mpl.colors.Normalize(vmin=0, vmax=1.0, clip=False)
313
314     #Map color scale based on norm and color scheme
315     mapper = cm.ScalarMappable(norm=norm, cmap=cm.YlGnBu)

```

```

316 # Define figure and size based on pixel ratio (+title of window)
317 plt.figure('Voronoi Diagram section '+number[q], figsize=(20,(VerPixel/HorPixel
318 *20)))
319 #Boundary intersection check:
320 BoundCell =[]; BoundPoly=[]
321
322 #Region are the Voronoi indices of a specific cell, CN is the cell number
323 for i, (region, CN) in enumerate(zip(regions, vor.point_region)):
324
325     #Vertices[region] gives the x,y-coordinates of voronoi vertices
326     polygon = vertices[region]
327
328     #Poly is a polygon constructed from the coordinates specified by polygon
329     poly = Polygon(polygon)
330
331     #Transform polygon 'old' coordinates from x y, x y .. to (x,y),(x,y)..etc.
332     poly_old = [p for p in poly.exterior.coords]
333
334     #If poly intersects with boundary, polygon vertex coordinates are changed
335     poly = poly.intersection(boundary)
336
337     #Transform polygon 'new' coordinates from x y, x y .. to (x,y),(x,y)..etc.
338     poly_new = [p for p in poly.exterior.coords]
339
340     #Calculate area of poly_new (modified polygon or not)
341     Area.append(ConvexHull(poly_new).volume)
342     #Area list ordered with CN as leading variable
343     Area_ordered2[CN] = Area[i]
344     Area_net2[CN] = Area_ordered2[CN] - A_fib
345
346
347     #Colorize polygon based on the FRR and the color scale mapper, if
statement is used to correct cells with 1 < FRR < 0
348     if Area_net2[CN] < 0:
349         plt.fill(*zip(*poly_new), color='r', alpha=1, linewidth=1.0, linestyle='-'
', closed=False)
350         Elst.append(Area_net2[CN])
351         #Set local FRR to 1 to neglect incorrect data values
352         Local_FibVol2[CN] = 1
353     else:
354         Local_FibVol2[CN] = A_fib / Area_ordered2[CN]
355         plt.fill(*zip(*poly_new), color=mapper.to_rgba(Local_FibVol2[CN]),
alpha=0.8, linewidth = 1.0, linestyle = '-', closed = False)
356         n = n+1
357
358     #Statement to check whether or not the polygon is modified due to boundary
intersections
359     if np.round(ConvexHull(poly_old).volume,4) != np.round(ConvexHull(poly_new
).volume,4):
360         BoundCell.append(CN)
361         BoundPoly.append(poly_new)
362
363     return norm, Area, A_fib, Local_FibVol2, Area_net2, Elst, BoundCell, BoundPoly
364
365 # =====
366 # FUNCTION BLOCK 6:
367 # Additional plot function to add elements to Voronoi diagram
368 # =====
369 def VoronoiPlot(coordinates, vor, Area, norm, HorPixel, VerPixel):
370     """

```

```

371     Input:  coordinates; Input fibre location coordinates
372           vor;      Voronoi pattern applied to the input coordinates
373           Area;     List with areas of all polygon shapes
374           norm;     Normalized color map between 0 and 1
375           HorPixel; Image size width in pixels
376           VerPixel; Image size height in pixels
377     Output: DisList; List with CN, Vor. cell number, y-coordinate, cell area
378           ""
379     # Plot original fibre locations as dots in same figure
380     plt.plot(coordinates[:, 0], coordinates[:, 1], 'ko', markersize = 2)
381
382     #DisList is a matrix with: [Input coordinate number, CN, input y-coordinate,
383     area Vor. cell, input x-coordinate]
384     DisList = np.zeros((len(coordinates),5))
385     m = 0
386     for i in (vor.point_region):
387         # plt.text(coordinates[m][0], coordinates[m][1], f'CN{i}', fontsize = 10)
388         DisList[m,0] = m # Number of input coordinate
389         DisList[m,1] = i # Number of corresponding Voronoi
390         Cell
391         DisList[m,2] = coordinates[m][1] # Y-coordinate of input coordinate
392         DisList[m,3] = Area[m] # Area of Voronoi cell
393         DisList[m,4] = coordinates[m][0] # X-coordinate of input coordinate
394         m = m+1
395
396     #Load and display actual image behind Voronoi diagram
397     plt.xlim(0, HorPixel) #Set limits of x- and y-axis
398     plt.ylim(0, VerPixel)
399     img_file = directory[ fileloc]+ '/02-Images/' +number[q]+ '.png'
400     img = plt.imread(img_file)
401     plt.imshow(img[:, :-1], origin = 'lower', cmap = plt.cm.gray)
402     #Plot preparation
403     plt.title('Fibre Location Voronoi Diagram and FRR Colorplot\n'+plotnames[
404     fileloc], fontsize=45)
405     plt.xlabel('Pixels', fontsize=30); plt.ylabel('Pixels', fontsize=30)
406     plt.xticks(fontsize=28), plt.yticks(fontsize=28)
407     cb = plt.colorbar(cm.ScalarMappable(norm=norm, cmap=cm.YlGnBu), ax=None, shrink
408     =0.75)
409     cb.ax.tick_params(labelsize=25)
410     cb.ax.get_yaxis().labelpad = 0
411     cb.ax.get_xaxis().labelpad = 20
412     cb.ax.set_title('FRR', fontsize=25)
413
414     #Segmental distribution of micrographs
415     t = VerPixel #Total height of micrograph
416     dt = t/segments #Thickness of one segment
417     midpoint = int(segments/2)
418     plt.tight_layout()
419     plt.show()
420     plt.savefig(directory[ fileloc]+ '/03-plots/VoronoiDiagram_' +plotnames[ fileloc]+
421     '_' +number[q]+ '.png', format='png', dpi=200)
422     #From midpoint on, for each iteration there will be a paralel line drawn at
423     distance -k*dt and +k*dt from the mid-line
424     for k in range(midpoint+1):
425         Yleft_bot = Acoff * 0 + Bcoff - k * dt
426         Yleft_top = Acoff * 0 + Bcoff + k * dt
427         Yright_bot = Acoff * HorPixel + Bcoff - k * dt
428         Yright_top = Acoff * HorPixel + Bcoff + k * dt
429
430         if k == 0: # Creates the dashed mid-section line

```

```

425     plt.plot(X_midline ,( Yleft_bot , Yright_bot ), linestyle='--', color = '
black')
426     else:
427         plt.plot(X_midline ,( Yleft_bot , Yright_bot ), color = 'black')
428         plt.plot(X_midline ,( Yleft_top , Yright_top ), color = 'black')
429     plt.tight_layout()
430     plt.show()
431     plt.savefig(directory[ fileloc]+ '/03-plots/VoronoiDiagram_' + plotnames[ fileloc]+
'_' + number[q]+ '_skewlines.png', format='png', dpi=200)
432
433     return DisList
434
435 # =====
436 # FUNCTION BLOCK 7:
437 # Function to plot the Voronoi pattern over actual image, including fib/res
438 # distribution expressed as color map
439 # =====
440 def VorDistributionPlot(VerPixel , segments , DisList , A_fib ):
441     """
442     Input:  coordinates; Input fibre location coordinates
443            vor;       Voronoi pattern applied to the input coordinates
444            Area;     List with areas of all polygon shapes
445            norm;     Normalized color map between 0 and 1
446            VerPixel; Image size height in pixels
447            segments; Amount of segments sections through thickness
448            DisList;  List with CN, Vor. cell number, y-coordinate, cell area
449            D_fib;    Measured fibre diameter
450     Output: FibVol_dbl; List with fib/res distribution through thickness
451     """
452     t = VerPixel
453     dt = t/segments
454     #Thickness distribution points, n segment means n+1 edge points
455     Td = np.zeros((1, segments+1))
456
457     #List (one for each segment) with local FRRs, and list for avg segment value
458     Loc_FibVol_lst = [[] for _ in range(segments)]
459     Loc_FibVol_lst_avg = [[] for _ in range(segments)]
460
461     # count loops from 0 to len(DisList[:,2]), Y is each input y-coordinate
462     for count , Y in enumerate(DisList[:,2]):
463         X = DisList[count,4]
464
465         midpoint = int(segments/2)
466         #Define segment distribution coordinates, the top and bottom y-coordinate
of a section are x-coordinate dependent due to the skewness of the lines
467         for i in range(midpoint+1):
468             Td[0, midpoint-i] = Acoff*X+Bcoff - i * dt
469             Td[0, midpoint+i] = Acoff*X+Bcoff + i * dt
470         #Define left and boundary of specific thickness segment
471         for n in range(segments):
472             left = Td[0, n]
473             right = Td[0, n+1]
474             #Check in which segment the y-coordinate falls
475             if Y >= left and Y < right:
476                 Loc_FibVol_lst[n].append(DisList[count,3])
477                 break #if segment found, break for loop to speed up calculation
478     #For segmental plot, twice each value needed (except edge values)
479     Td_dbl = []; FibVol_dbl = []
480     for i in range(segments):
481         Loc_FibVol_lst_avg[i] = A_fib/ np.mean(Loc_FibVol_lst[i])
482         FibVol_dbl.append(Loc_FibVol_lst_avg[i])

```

```

483     FibVol_dbl.append(Loc_FibVol_lst_avg[i])
484     Td_dbl.append(Td[0][i])
485     Td_dbl.append(Td[0][i])
486     Td_dbl.append(Td[0][i+1]); Td_dbl.append(Td[0][i+1])
487     Td_dbl = Td_dbl[1:-1]
488
489     #Plotting commands
490     fig = plt.figure(number[q], figsize=(20*0.5,(VerPixel/HorPixel*20)))
491     ax = fig.add_subplot(111)
492     plt.title('FRR Through Tape Thickness \n'+plotnames[fileloc]+' section: '+
number[q], fontsize=45)
493     plt.plot(FibVol_dbl, Td_dbl, label = 'Fiber-Resin Ratio', linewidth=5); plt.grid
(True)
494     plt.xlabel('FRR', fontsize=30)
495     plt.ylabel('Tape Thickness Direction in Pixels', fontsize=30)
496     plt.yticks(np.arange(0, VerPixel, 100))
497     plt.xticks(np.arange(0, 1, 0.1))
498     plt.ylim(0, VerPixel)
499     ax.tick_params(axis='x', which='major', labelsize=20)
500     ax.tick_params(axis='y', which='major', labelsize=20)
501     plt.savefig(directory[fileloc]+' /03-plots/FibResDistribution'+number[q]+'_skew
.png', format='png', dpi=200)
502
503     return FibVol_dbl, Loc_FibVol_lst_avg, Td
504
505     # =====
506     # FUNCTION BLOCK 8 (first part):
507     # Function to combine the individual FR ratios through thickness for each of
508     # the micrographs, to one single list
509     # =====
510     def VorDistributionPlot_Combined_data(FibRes):
511         """
512         Input: FibRes; Input list with the local FRR through thickness for each
513         single microscopic sample
514
515         Output: Mean_fr_ratio_NOnan; List with average FRR through thickness, nan
516         's filtered out
517         Mean_fr_ratio_NOnan_dbl; Same list with all but first and last items
518         twice for plotting purpose
519         Std_fr_ratio_NOnan; List with error values for FRR calculation
520         Ylst1; List with vertical position of thickness
521         segments (not modified yet)
522         Ylst2; List with vertical position for error bars (
523         not modified yet)
524         """
525         #Provide average of FRR in each segment of all micrographs
526         Mean_fr_ratio = [np.nanmean(k) for k in zip(*FibRes)]
527         #Not A Number (NAN) due to segments without fibres, each nan removed properly
528         Mean_fr_ratio_NOnan = [x for x in Mean_fr_ratio if str(x) != 'nan']
529
530         FR_segments = len(Mean_fr_ratio_NOnan)
531
532         #For plotting purposes, append value twice
533         Mean_fr_ratio_NOnan_dbl = np.repeat(Mean_fr_ratio_NOnan, 2)
534
535         #Error of FRR of each individual thickness segment
536         Std_fr_ratio = [np.nanstd(k) for k in zip(*FibRes)]
537         Std_fr_ratio_NOnan = [x for x in Std_fr_ratio if str(x) != 'nan']
538
539         #Ylst1 and Ylst2 used for plotting mean FRR and std FRR, respectively
540         dt = VerPixel/segments

```

```

536 Ylst = np.zeros(FR_segments+1)
537 for i in range(FR_segments+1):
538     Ylst[i] = dt*i*T_ratio
539 Ylst1 = np.repeat(Ylst,2)
540 Ylst1 = Ylst1[1:-1]
541
542 Ylst2 = [x+((dt/2)*T_ratio) for x in Ylst]
543 Ylst2 = Ylst2[: -1]
544
545 return Mean_fr_ratio_NOnan, Mean_fr_ratio_NOnan_dbl, Std_fr_ratio_NOnan, Ylst1,
Ylst2
546
547 # =====
548 # FUNCTION BLOCK 9:
549 # Function which filters the polygons which intersect with the defined boundary
550 # =====
551 def Polygon_edge_detection(BoundCell, DisList, HorPixel, VerPixel):
552     #List FRR values of Voronoi cells at top and bottom boundary
553     Boundpoly_sel_top=[]; Boundpoly_sel_bot=[]
554     BoundcellFR_top =[]; BoundcellFR_bot =[]
555     """
556     Input: BoundCell; Input list with the Voronoi CN which intersects with the
pre-defined boundary
557           DisList; Matrix with x-,y-coordinates, CN's, Cell areas
558           HorPixel; Width of input image in pixels
559           VerPixel; Height of input image in pixels
560     Output: avgFR_bound_top; list with averaged FR ratio of top edge Voronoi cells
561           avgFR_bound_bot; list with averaged FR ratio of bot edge Voronoi cells
562     """
563     for count, i in enumerate(BoundCell): #Counter and i = Voronoi Cell number (CN)
564         # Find location of index of the CN in the DisList matrix
565         loc = np.where(DisList[:,1] ==i)
566         xpos = np.asscalar(DisList[loc,4]) # Corresponding x-coordinate of CN
567         #Neglect left and right boundary FRR
568         if 25 < xpos < HorPixel-25:
569             ypos = np.asscalar(DisList[loc,2]) # Corresponding y-coordinate of CN
570
571             #Top boundary Vor. cells, based on y-coordinate and midline midpoint
572             if ypos > np.mean(Y_midline[q]):
573                 Boundpoly_sel_top.append(BoundPoly[count])
574                 #Corresponding FR ratio of Voronoi cell appended to a list
575                 BoundcellFR_top.append(FR_lst[i])
576             elif ypos < np.mean(Y_midline[q]): #Bottom equivalent
577                 Boundpoly_sel_bot.append(BoundPoly[count])
578                 BoundcellFR_bot.append(FR_lst[i])
579
580             avgFR_bound_top.append(np.mean(BoundcellFR_top))
581             avgFR_bound_bot.append(np.mean(BoundcellFR_bot))
582
583             #Plotting commands
584             plt.figure('Voronoi Diagram section '+number[q], figsize=(20,(VerPixel/HorPixel
*20)))
585             for i in range(len(Boundpoly_sel_top)):
586                 plt.fill(*zip(*Boundpoly_sel_top[i]), color='y')
587                 if i == len(Boundpoly_sel_top)-1:
588                     plt.fill(*zip(*Boundpoly_sel_top[i]), color='y', label='Top surface
Voronoi cells')
589
590             plt.figure('Voronoi Diagram section '+number[q], figsize=(20,(VerPixel/HorPixel
*20)))
591             for i in range(len(Boundpoly_sel_bot)):

```

```

592     plt.fill(*zip(*Boundpoly_sel_bot[i]), color='g')
593     #To comply with desired legend
594     if i == len(Boundpoly_sel_bot)-1:
595         plt.fill(*zip(*Boundpoly_sel_bot[i]), color='g', label = 'Bottom
surface Voronoi cells')
596     plt.legend(loc='lower center', bbox_to_anchor=(0.5,0.2), prop={'size':25})
597     plt.savefig(directory[fileloc]+' /03-plots/VoronoiDiagram_EdgeDetection_' +
number[q]+' _skew.png', format='png', dpi=200)
598
599     return avgFR_bound_top, avgFR_bound_bot
600
601 # =====
602 # FUNCTION BLOCK 10:
603 # Function to present top and bottom boundary FRR of tape. #
604 # =====
605 def EdgeFRR_BarPlot(avgFR_bound_top_l, avgFR_bound_bot_l):
606     """
607     Input:  avgFR_bound_top_l; list with averaged FR ratio of top edge Voronoi
cells
608            avgFR_bound_bot_l; list with averaged FR ratio of bottom edge Voronoi
cells
609
610     Output: avgFR_bound_top_s; Single scalar value for average FRR of top boundary
611            avgFR_bound_bot_s; Single scalar value for average FRR of bottom
boundary
612     """
613     #Calculate avg and std of top and bottom lists
614     avgFR_bound_top_s = np.mean(avgFR_bound_top_l)
615     avgFR_bound_bot_s = np.mean(avgFR_bound_bot_l)
616     stdFR_bound_top = np.std(avgFR_bound_top_l)
617     stdFR_bound_bot = np.std(avgFR_bound_bot_l)
618
619     #Plotting commands
620     fig = plt.figure('Barplot Edge Voronoi Cells Intersecting With Boundary
Polygon')
621     ax = fig.add_subplot(111)
622     plt.grid(axis='y', zorder=0)
623     plt.bar(('Top boundary', 'Bottom boundary'), (avgFR_bound_top_s,
avgFR_bound_bot_s), color=Blue, yerr=(stdFR_bound_top, stdFR_bound_bot), capsize=5)
624     plt.ylabel('$FRR$', fontsize=20)
625     plt.yticks(np.arange(0,0.7+0.1,0.1))
626     plt.title(plotnames[fileloc], fontsize=25)
627     ax.set_axisbelow(True)
628     ax.tick_params(axis='both', which='major', labelsize=15)
629     plt.savefig(directory[fileloc]+' /03-plots/Edge_FR_Ratio_' + plotnames[fileloc] +
'.png', format='png', dpi=200)
630
631     return avgFR_bound_top_s, avgFR_bound_bot_s
632
633 # =====
634 # FUNCTION BLOCK 8 (second part):
635 # Function to plot the combined individual FRR through thickness
636 # =====
637 def VorDistributionPlot_Combined_plot(avgFR_bound_top_s, avgFR_bound_bot_s, Ylst1,
Ylst2, Mean_fr_ratio_NOnan_dbl):
638     """
639     Input:  avgFR_bound_top_s; Single scalar value for average FRR of top boundary
640            avgFR_bound_bot_s; Single scalar value for average FRR of bottom
boundary
641
642     Output: Combined FRR plot through thicknes, scaled to FRR bot,top ratio

```

```

643     """
644     #Define ratio between FRR top and FRR bottom edge
645     ratio_total = avgFR_bound_top_s + avgFR_bound_bot_s
646     ratio_bot   = avgFR_bound_top_s / ratio_total
647
648     # Modified Ylst1 and Ylst2 for vertical shift according to tape thickness
649     Ylst1_mod = [x + (t_tape-np.max(Ylst1))/2*ratio_bot*2 for x in Ylst1]
650     Ylst2_mod = [x + (t_tape-np.max(Ylst1))/2*ratio_bot*2 for x in Ylst2]
651
652     #Plotting commands
653     plt.figure('Combined Tape Sections')
654     plt.plot((0,HorPixel),(t_tape,t_tape),linewidth=2,linestyle='--',color=Blue,
655             label='Tape Boundary')
656     plt.plot(Mean_fr_ratio_NOnan_dbl,(Ylst1_mod),label='Mean FRR')
657     plt.plot((0,HorPixel),(0,0),linewidth=2,linestyle='--',color=Blue)
658     plt.xlim(0.0,1.0)
659     plt.xticks(np.arange(0.0, 1.1,0.1))
660     plt.errorbar(Mean_fr_ratio_NOnan,(Ylst2_mod), xerr=Std_fr_ratio_NOnan,ls=
661                 'none',c='black',capsize=1, elinewidth=1, markeredgewidth=2,label='Error')
662
663     plt.title('Average FRR Distribution \n'+plotnames[fileloc])
664     plt.xlabel('FRR')
665     plt.ylabel('Tape Thickness [mm]')
666     plt.grid()
667     plt.legend()
668     plt.savefig(directory[fileloc]+' /03-plots /
669                 FiberResinDistribution_Combinedsections'+plotnames[fileloc]+' .png', format='png',
670                 ,dpi=200)
671
672     return
673
674     # =====
675     # Python code
676     # =====
677     FibRes=[]; Error_lst = []; avgFR_bound_top=[]; avgFR_bound_bot=[]
678     for q in range(len(number)):
679
680         #Calculate A and B coefficient of segmental distribution lines
681         Acoeff = np.polyfit(X_midline ,Y_midline[q],1)[0]
682         Bcoeff = np.polyfit(X_midline ,Y_midline[q],1)[1]
683         #Define fibre coordinates and boundary coordinates
684         coordinates ,boundary = CoordinateExtraction(FibCorFile ,BoundCorFile)
685         #Calculate Voronoi pattern of input points
686         vor = Voronoi(coordinates ,qhull_options= '')
687         #Calculate finite regions and Voronoi vertices
688         regions , vertices = voronoi_finite_polygons_2d(vor)
689         #Calculate polygon modification related parameters
690         norm,Area,A_fib,FR_lst,Anett, Error_list ,BoundCell ,BoundPoly =
691         PolygonModification(regions ,vor ,vertices ,D_fib)
692         #Calculate DisList matrix
693         DisList = VoronoiPlot(coordinates ,vor ,Area ,norm ,HorPixel ,VerPixel)
694         #Calculate Local FRR per segment
695         FibVol_dbl ,FibVol_single ,Td = VorDistributionPlot(VerPixel ,segments ,DisList ,
696                 A_fib)
697         FibRes.append(FibVol_single)
698         #Check to ensure that amount of segments with fibres are equal for each
699         micrograph
700         print('\n')
701         print('Thickness segments with fibres located in it: ',len([x for x in
702                 FibVol_single if str(x) != 'nan']))
703         print('\n')

```


B

BLL Comparison Micrographs

Tacked CF-PEEK Teijin Samples

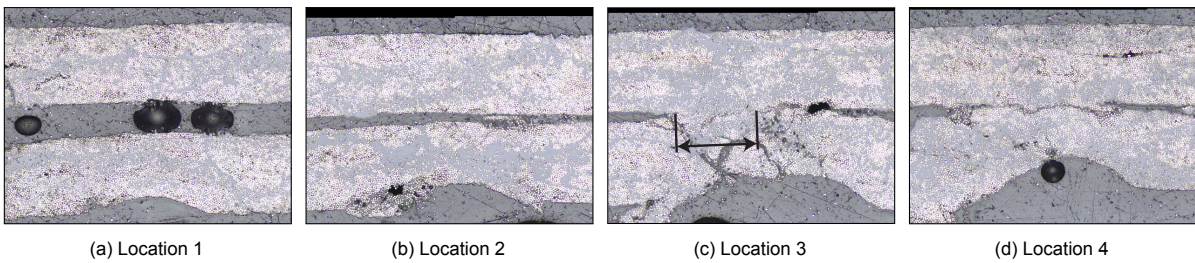


Figure B.1: Bond line comparison micrographs of tacked CF-PEEK Teijin sample 1

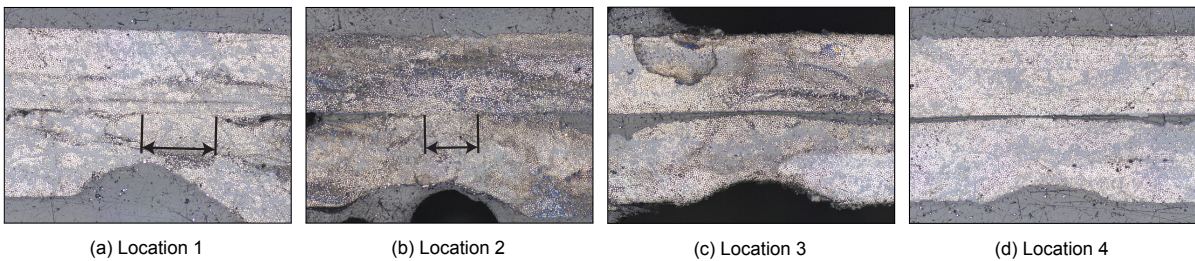


Figure B.2: Bond line comparison micrographs of tacked CF-PEEK Teijin sample 2

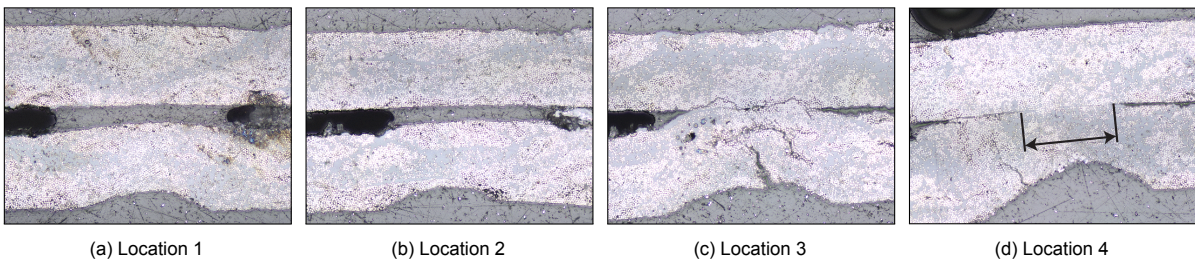


Figure B.3: Bond line comparison micrographs of tacked CF-PEEK Teijin sample 3

Tacked CF-PEKK Solvay Samples

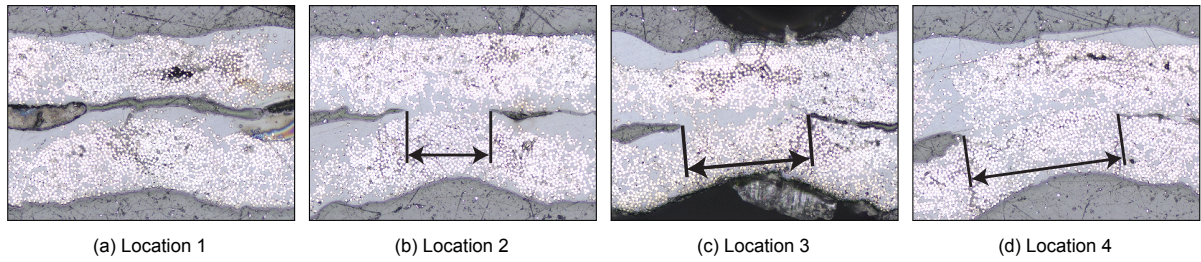


Figure B.4: Bond line comparison micrographs of tacked CF-PEKK Solvay tape 1

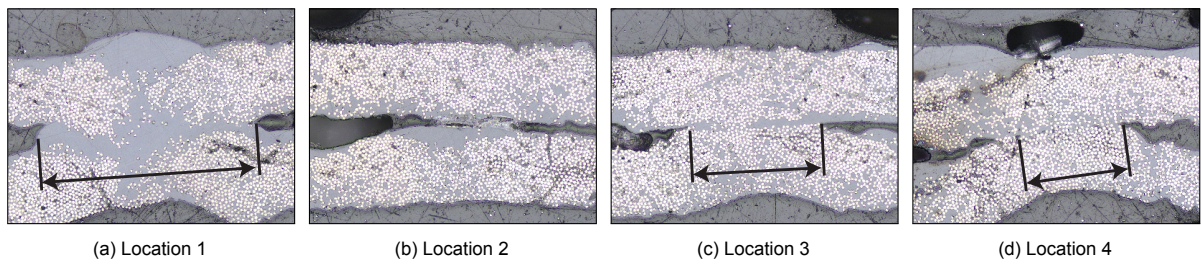


Figure B.5: Bond line comparison micrographs of tacked CF-PEKK Solvay sample 2

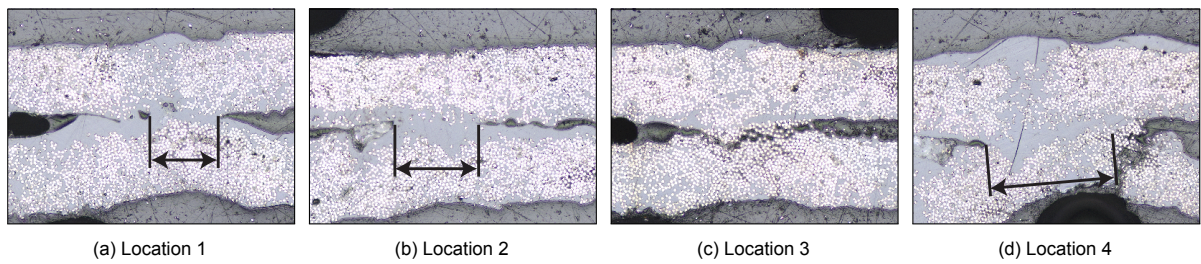


Figure B.6: Bond line comparison micrographs of tacked CF-PEKK Solvay sample 3

Tacked CF-PEKK Toray Samples

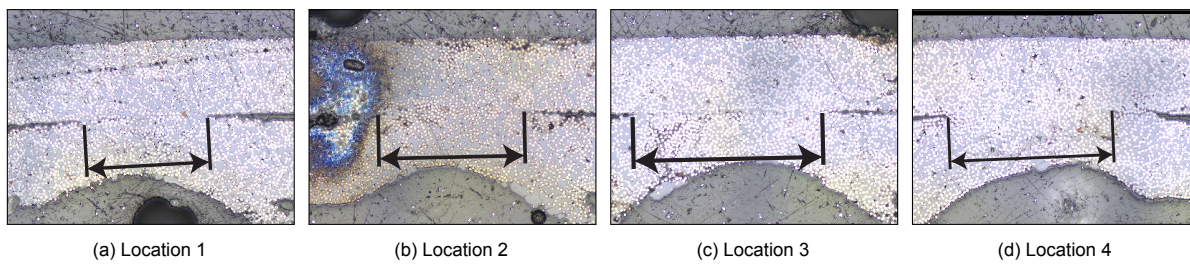


Figure B.7: Bond line comparison micrographs of tacked CF-PEKK Toray sample 1

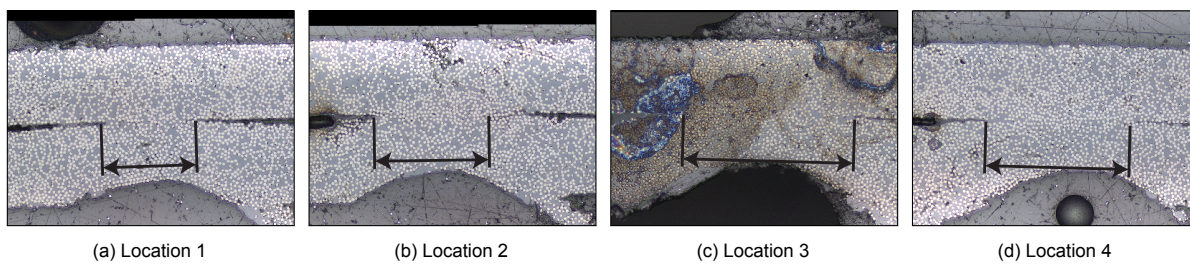


Figure B.8: Bond line comparison micrographs of tacked CF-PEKK Toray sample 2

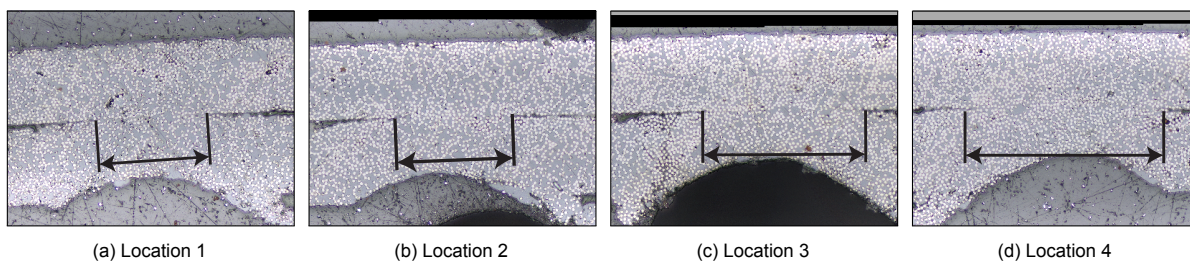


Figure B.9: Bond line comparison micrographs of tacked CF-PEKK Toray sample 3

Tacked CF-PEKK Solvay Samples - Fibre Rich Interface

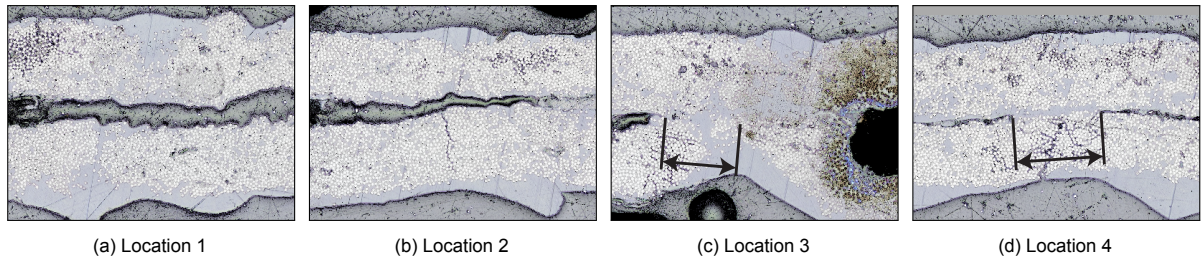


Figure B.10: Bond line comparison micrographs of tacked CF-PEKK Solvay fibre rich interface sample 1

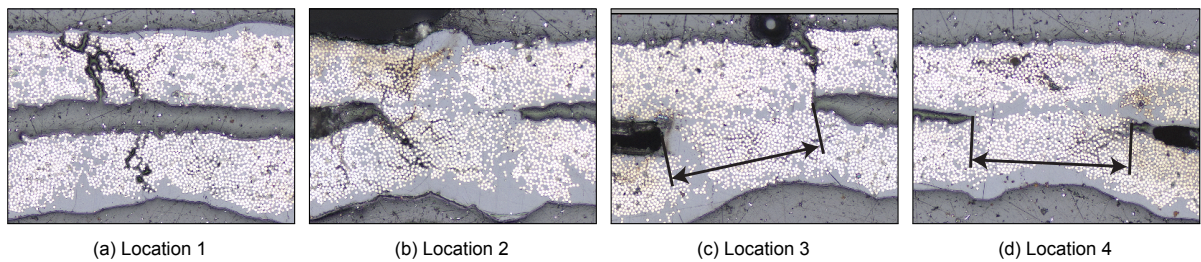


Figure B.11: Bond line comparison micrographs of tacked CF-PEKK Solvay fibre rich interface sample 2

Tacked CF-PEKK Solvay Samples - Resin Rich Interface

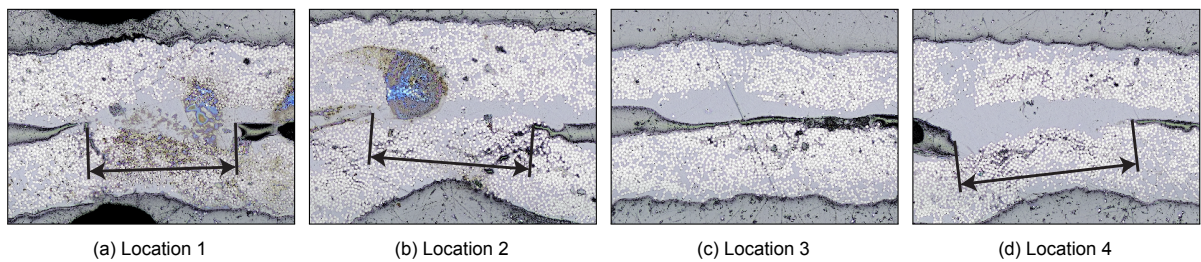


Figure B.12: Bond line comparison micrographs of tacked CF-PEKK Solvay resin rich interface sample 1

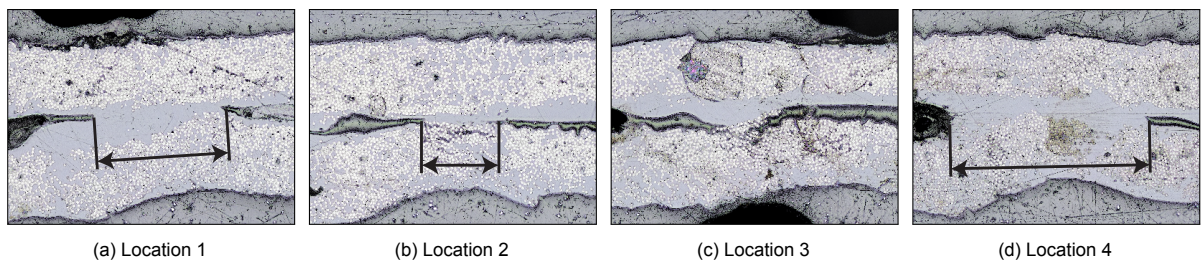
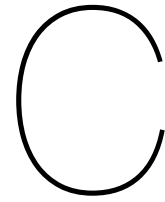


Figure B.13: Bond line comparison micrographs of tacked CF-PEKK Solvay resin rich interface sample 2



DOE Peel Force Results

CF-PEEK Teijin

Test	A [%]	P [%]	V [mm/s]	Peel Force [N]		
				Run 1	Run 2	Run 3
1	65	40	90	5.91	6.40	5.33
2	95	40	90	12.68	12.16	12.43
3	65	46	90	5.58	7.09	6.75
4	95	46	90	11.24	11.81	11.74
5	65	40	120	1.05	1.21	1.80
6	95	40	120	7.55	7.55	7.74
7	65	46	120	4.17	6.03	5.98
8	95	46	120	7.51	9.25	7.64
9	65	43	105	4.97	5.96	4.46
10	95	43	105	7.72	8.45	7.75
11	80	40	105	4.75	5.41	5.21
12	80	46	105	4.99	8.14	8.32
13	80	43	90	9.45	8.11	7.88
14	80	43	120	5.30	8.44	3.30
15	80	43	105	8.20	8.67	10.34
16	80	43	105	7.24	6.93	6.84
17	80	43	105	6.34	6.94	6.57

Table C.1: DOE peel force results CF-PEEK Teijin

CF-PEKK Solvay

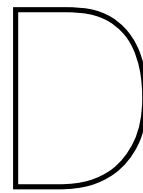
Test	A [%]	P [%]	V [mm/s]	Peel Force [N]		
				Run 1	Run 2	Run 3
1	70	12	80	4.36	3.06	2.64
2	100	12	80	11.32	10.19	13.66
3	70	18	80	11.63	15.70	14.27
4	100	18	80	21.37	24.36	23.74
5	70	12	120	0.90	2.10	1.87
6	100	12	120	6.89	5.16	5.22
7	70	18	120	7.60	6.80	8.54
8	100	18	120	14.89	14.36	15.86
9	70	15	100	4.31	5.96	5.07
10	100	15	100	10.45	11.50	15.93
11	85	12	100	3.86	5.65	4.29
12	85	18	100	14.54	15.72	12.55
13	85	15	80	11.99	11.15	12.66
14	85	15	120	7.10	8.23	8.21
15	85	15	100	8.38	7.54	9.72
16	85	15	100	9.02	9.89	11.24
17	85	15	100	10.47	9.74	10.36

Table C.2: DOE peel force results CF-PEKK Solvay

CF-PEKK Toray

Test	A [%]	P [%]	V [mm/s]	Peel Force [N]		
				Run 1	Run 2	Run 3
1	65	19	90	0.73	0.42	1.36
2	95	19	90	1.49	2.03	3.16
3	65	25	90	3.10	3.94	2.38
4	95	25	90	6.91	7.61	8.49
5	65	19	120	0.42	0.24	0.23
6	95	19	120	0.73	0.78	1.34
7	65	25	120	1.32	1.22	0.78
8	95	25	120	4.02	2.20	6.11
9	65	22	105	0.66	0.71	0.89
10	95	22	105	3.42	2.11	2.97
11	80	19	105	1.11	0.54	0.88
12	80	25	105	4.41	2.30	5.01
13	80	22	90	2.41	4.46	1.87
14	80	22	120	0.87	1.78	1.33
15	80	22	105	1.15	1.48	2.16
16	80	22	105	2.40	1.33	1.04
17	80	22	105	2.69	0.98	2.77

Table C.3: DOE peel force results CF-PEKK Toray



Analysis of Variance DOE Results

CF-PEEK Teijin ANOVA

Source	DF	Contribution	Adj SS	Adj MS	F-Value	P-Value
Model	11	86.10%	355.201	32.291	21.96	0.000
Blocks	2	1.10%	4.524	2.262	1.54	0.227
Linear	3	79.07%	326.206	108.735	73.95	0.000
Amplitude	1	47.35%	195.328	195.328	132.84	0.000
Pressure	1	4.49%	18.541	18.541	12.61	0.001
Velocity	1	27.23%	112.337	112.337	76.40	0.000
Square	3	1.99%	8.208	2.736	1.86	0.152
Amplitude*Amplitude	1	1.84%	6.294	6.294	4.28	0.045
Pressure*Pressure	1	0.14%	0.630	0.630	0.43	0.517
Velocity*Velocity	1	0.01%	0.054	0.054	0.04	0.849
2-Way Interaction	3	3.94%	16.263	5.421	3.69	0.020
Amplitude*Pressure	1	1.41%	5.834	5.834	3.97	0.053
Amplitude*Velocity	1	1.22%	5.046	5.046	3.43	0.072
Pressure*Velocity	1	1.31%	5.384	5.384	3.66	0.063
Error	39	13.90%	57.347	1.470		
Lack-of-Fit	33	11.12%	45.871	1.390	0.73	0.747
Pure Error	6	2.78%	11.476	1.913		
Total	50	100.00%	412.548			

Table D.1: ANOVA results of CF-PEEK Teijin DOE

CF-PEKK Solvay ANOVA

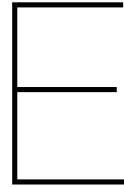
Source	DF	Contribution	Adj SS	Adj MS	F-Value	P-Value
Model	11	95.52%	1324.41	120.401	75.51	0.000
Blocks	2	0.60%	8.26	4.131	2.59	0.088
Linear	3	91.51%	1268.93	422.976	265.26	0.000
Amplitude	1	29.13%	403.9	403.895	253.29	0.000
Pressure	1	47.62%	660.24	660.243	414.06	0.000
Velocity	1	14.77%	204.79	204.79	128.43	0.000
Square	3	0.72%	10.01	3.336	2.09	0.117
Amplitude*Amplitude	1	0.11%	0.41	0.412	0.26	0.614
Pressure*Pressure	1	0.24%	0.92	0.92	0.58	0.452
Velocity*Velocity	1	0.37%	5.08	5.077	3.18	0.082
2-Way Interaction	3	2.68%	37.21	12.405	7.78	0.000
Amplitude*Pressure	1	0.47%	6.55	6.548	4.11	0.050
Amplitude*Velocity	1	1.02%	14.12	14.115	8.85	0.005
Pressure*Velocity	1	1.19%	16.55	16.551	10.38	0.003
Error	39	4.48%	62.19	1.595		
Lack-of-Fit	33	3.99%	55.26	1.675	1.45	0.341
Pure Error	6	0.50%	6.93	1.155		
Total	50	100.00%	1386.60			

Table D.2: ANOVA results of CF-PEKK Solvay DOE

CF-PEKK Toray ANOVA

Source	DF	Contribution	Adj SS	Adj MS	F-Value	P-Value
Model	11	85.65%	2.08448	0.189498	21.16	0.000
Blocks	2	1.40%	0.03405	0.017027	1.9	0.163
Linear	3	81.74%	1.98923	0.663076	74.05	0.000
Amplitude	1	25.73%	0.62628	0.626277	69.94	0.000
Pressure	1	40.77%	0.99211	0.992109	110.79	0.000
Velocity	1	15.24%	0.37084	0.370842	41.41	0.000
Square	3	0.83%	0.02013	0.00671	0.75	0.529
Amplitude*Amplitude	1	0.00%	0.00675	0.006751	0.75	0.391
Pressure*Pressure	1	0.56%	0.00685	0.006847	0.76	0.387
Velocity*Velocity	1	0.26%	0.00645	0.006445	0.72	0.401
2-Way Interaction	3	1.69%	0.04107	0.013689	1.53	0.222
Amplitude*Pressure	1	1.13%	0.02749	0.027492	3.07	0.088
Amplitude*Velocity	1	0.01%	0.00033	0.000333	0.04	0.848
Pressure*Velocity	1	0.54%	0.01324	0.013242	1.48	0.231
Error	39	14.35%	0.34923	0.008955		
Lack-of-Fit	33	11.27%	0.27438	0.008314	0.67	0.791
Pure Error	6	3.08%	0.07485	0.012475		
Total	50	100.00%	2.43371			

Table D.3: ANOVA results of CF-PEKK Toray DOE



Optimization of Ultrasonic Technology Experiment: Results

Peel Force Results

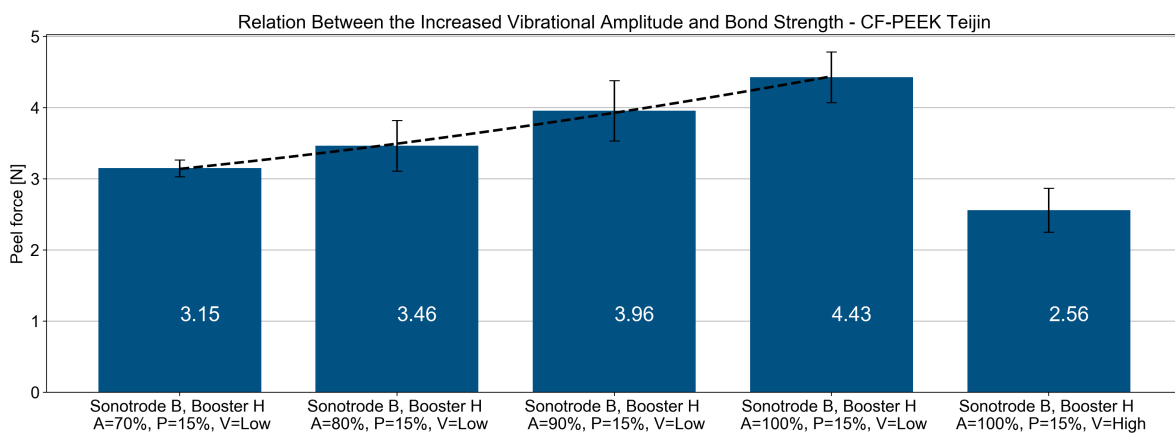


Figure E.1: CF-PEEK Teijin: influence of vibrational amplitude on the bond strength

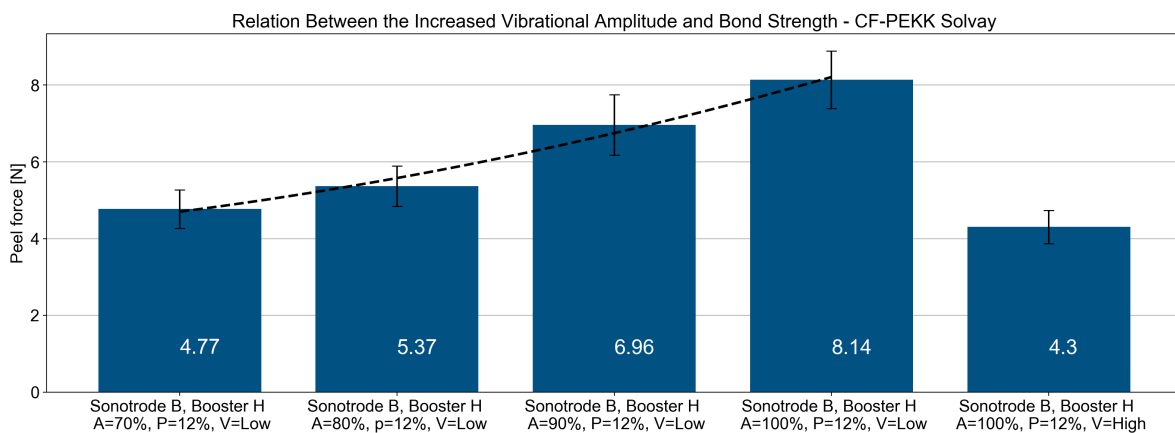


Figure E.2: CF-PEKK Solvay: influence of vibrational amplitude on the bond strength

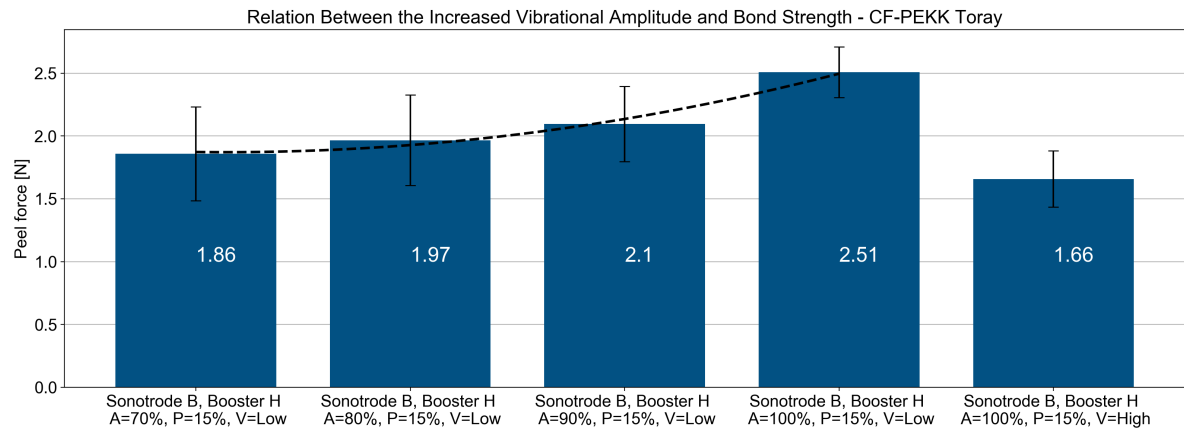


Figure E.3: CF-PEKK Toray: influence of vibrational amplitude on the bond strength

Required Power Results

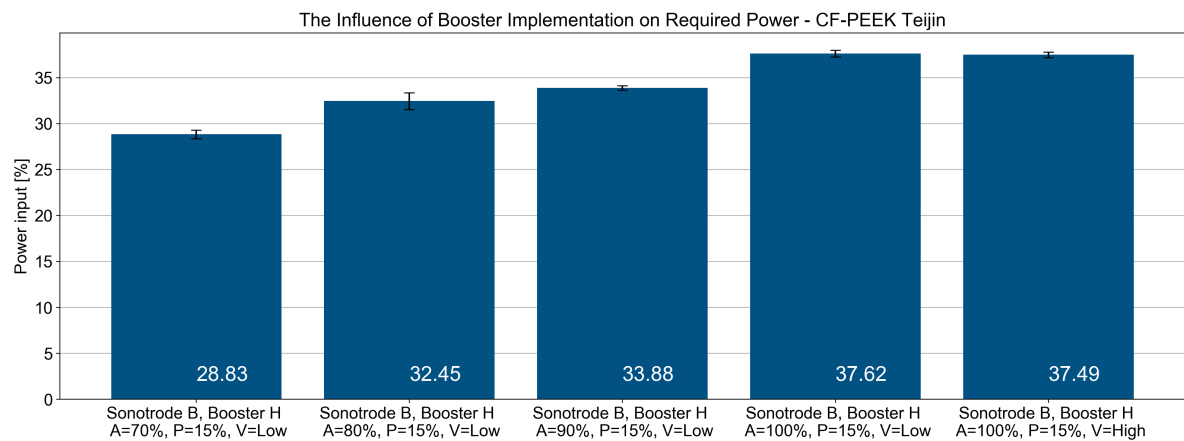


Figure E.4: CF-PEEK Teijin: influence of vibrational amplitude on the required power

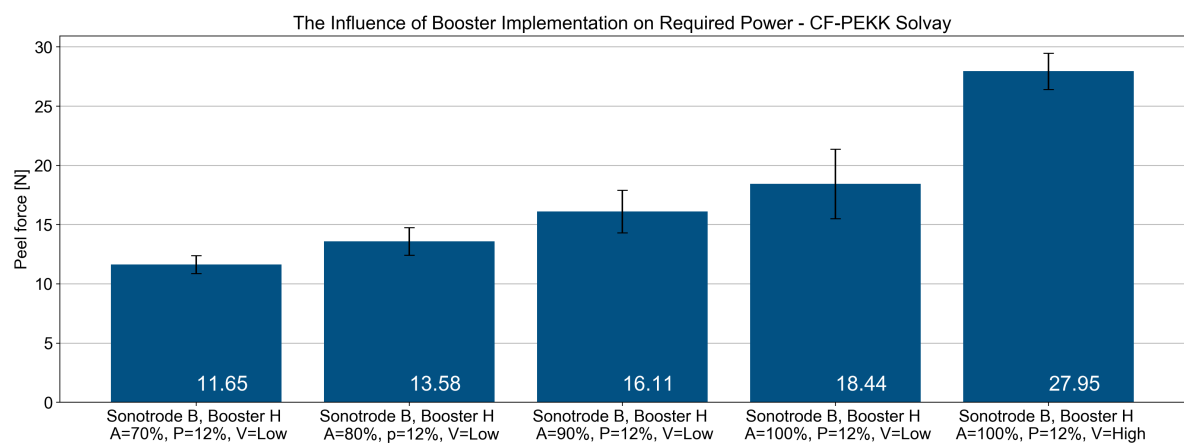


Figure E.5: CF-PEKK Solvay: influence of vibrational amplitude on the required power

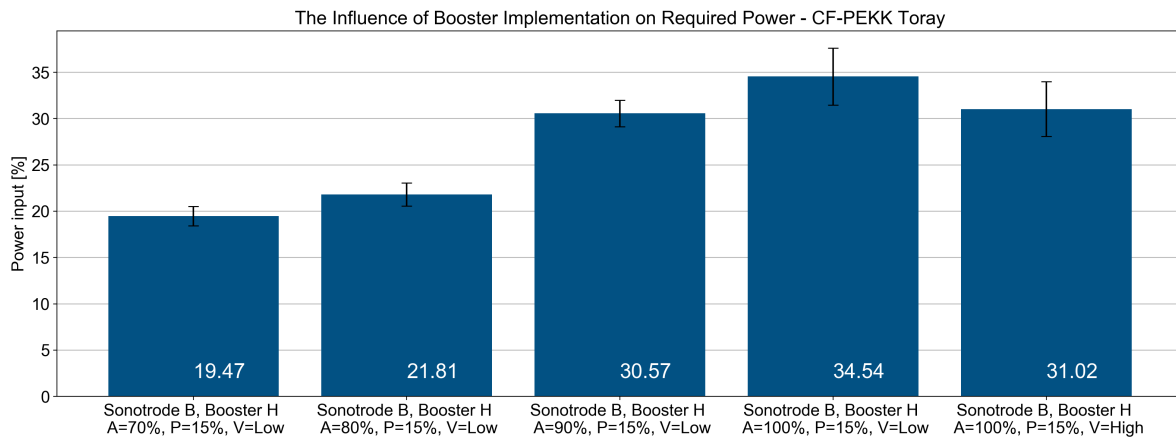


Figure E.6: CF-PEKK Toray: influence of vibrational amplitude on the required power